Brillouin dynamic gratings in optical fibres for distributed sensing and advanced optical signal processing

THÈSE Nᴼ 6768 (2015)

PRÉSENTÉE LE 16 OCTOBRE 2015
À LA FACULTÉ DES SCIENCES ET TECHNIQUES DE L'INGÉNIEUR
GROUPE SCI STI LT
PROGRAMME DOCTORAL EN PHOTONIQUE

ÉCOLE POLYTECHNIQUE FÉDÉRALE DE LAUSANNE

POUR L'OBTENTION DU GRADE DE DOCTEUR ÈS SCIENCES

PAR

Andrey DENISOV

acceptée sur proposition du jury:

Prof. J.-E. Moser, président du jury
Prof. L. Thévenaz, directeur de thèse
Prof. A. Zadok, rapporteur
Prof. M. González Herráez, rapporteur
Prof. C.-S. Brès, rapporteuse

EPFL

ÉCOLE POLYTECHNIQUE
FÉDÉRALE DE LAUSANNE

Suisse
2015

Acknowledgements

The four years I spent working on my thesis were the best time of my life so far, both inside the lab and outside of it. It would be surely impossible without the people who surrounded and supported me.

I will start with my supervisor, Prof. Luc Thévenaz, for without him this thesis would not exist. I would like to thank him warmly for accepting me as his student, thus, allowing me to do exactly the type of a PhD I was dreaming of. He shared my enthusiasm about new techniques and helped me to fill the gaps in my knowledge so I could implement the ideas I had. I would also like mention the warm, family-like atmosphere Luc cultivates in the lab, which made these years especially memorable.

My thanks go to SangHoon Chin, who took me under his wing when I have just arrived; he helped me to quickly learn the essential things about the work in our lab. After leaving the lab he remained a frequent guest, which lead to interesting discussions for which I am grateful as well. After SangHoon left the lab, Marcelo Soto took his place as my mentor. I would like to thank him for all the times he helped me find the answers to questions "Why doesn't it work?" and "How do I make it work?"

I would like to thank my thesis jury members: Prof. Avinoam Zadok from Bar-Ilan University, Prof. Miguel González Herráez from University of Alcalá, and Prof. Camille-Sophie Brès from EPFL. Prof. Zadok gets additional thanks for the friendly competition between our groups which stimulated me to achieve the best possible results. I would also like to thank Prof. Miguel González Herráez for the knowledge he shared during his stays in our lab and the research done in the collaboration between our groups.

A significant part of the research I carried out during these years has roots in the work done by a fellow PhD student Nikolay Primerov. Not only he was a great teacher while transferring me his know-how in Brillouin dynamic gratings, he also helped me out several times with my problems outside of the lab. I would like to thank my other colleagues: Isabelle Dicaire, Mehdi Alem, Xin Lu, Kenny Hey Tow, and Desmond Chow, for all the friendly discussions we had about science and life in general. Kenny also gets special thanks for our talks about British comedy and for all the times he helped me out with his knowledge of French.

My deep gratitude goes to our lab secretary Alexandra Morrison for preventing me

Abstract

This thesis presents results of a research on applications of Brillouin dynamic gratings – distributed reflectors that can be dynamically created in an optical fibre by two optical waves. A basic theory of stimulated Brillouin scattering (SBS) is introduced, on a level enough for understanding the processes that govern SBS.

A major part of this thesis is dedicated to studies of distributed Brillouin sensors based on phase correlation. First, the concept of correlation-based sensors is introduced; it is described how the Brillouin interaction between two waves can be localised, creating a permanent reflector confined to a millimetre-scale section of the fibre. This allows creating a distributed sensing system with very a high spatial resolution.

A detailed theoretical model for the phase-correlation technique is presented, showing how the gain response of a system can be calculated and how the system's resolution can be determined. For an ideal case an analytical solution is derived, while for real experimental conditions the expected behaviour is found via numerical simulation. Results of numerical modelling are compared with experimentally obtained data, showing a good agreement. A spatial resolution of 1 cm is demonstrated over a 200 m distance, representing 20 000 separate points.

The concept of time gating is introduced, extending the measurement distance from 200 m to 17.5 km while retaining a sub-centimetre spatial resolution. This technique allows for a two order of magnitude increase in the number of points that a system is capable to resolve. An absolute record for distributed fibre sensors is achieved, demonstrating a system capable to resolve 2 100 000 separate points.

Limitations for a further increase in number of points are discussed as well as possible ways to overcome them. An issue related to the temperature dependency of the refractive index is discussed in details, since it can lead to significant errors in spatial accuracy. An algorithm is presented, capable of using the measured temperature to account for the change in the refractive index and correctly determine the positioning of measured data.

In the last chapter potential applications of Bragg dynamic gratings in signal processing are investigated. A theoretical model of BDG's in polarisation-maintaining fibres is presented capable of calculating reflection of a probe wave – continuous or pulsed. The model includes the case of non-uniform birefringence along the fibre.

Dynamic gratings are applied to create a flip-flop – an all-optical memory, turned on and off by a light pulse. A working system is demonstrated in a 1 m long fibre, corresponding to a 10 ns storage time. Using the theoretical model the birefringence variation is measured along the fibre. A preliminary study of spectral properties of dynamic gratings is presented, along with a model predicting the spectrum of a uniform BDG. It is demonstrated that the spectral properties of a BDG can be manipulated by changing the spectra of optical waves used in the generation process.

This work is concluded by a discussion, summing up the above-mentioned theoretical the experimental work. Potential applications of the presented research are proposed along with the most promising direction of further research activities.

iv

Version abrégée

Ces travaux de thèse présentent les résultats obtenus sur l'utilisation des réseaux Brillouin dynamiques, des réflecteurs qui peuvent être créés de façon distribuée sur toute la longueur d'une fibre optique. La théorie de base sur la diffusion Brillouin stimulée (SBS) est présentée pour une bonne compréhension des processus régissant ce phénomène.

Une partie majeure de ces travaux de recherches est dédiée à l'étude des capteurs répartis utilisant la diffusion Brillouin basés sur la corrélation de phase. En premier lieu, nous présentons le concept des capteurs avec des systèmes d'interrogation dans le domaine de corrélation – la technique de corrélation de phase.

Un modèle théorique détaillé pour la technique de corrélation de phase est présentée et nous montrons comment la réponse en gain et la résolution du système peuvent être déterminées. Pour le cas idéal, une solution analytique est déduite alors que pour les cas expérimentaux nous utilisons une simulation numérique pour prédire fidèlement le comportement du système: des valeurs mesurées expérimentalement sont en parfait accord avec celles déduites en partant du modèle numérique. De plus, une résolution spatiale de 1 cm sur une distance plus de 200 m – représentant ainsi 20 000 points différents – est démontrée.

Le concept de mesure à déclenchement périodique est présenté, étendant la mesure de 200 m à 17,5 km tout en gardant une résolution spatiale inférieure au centimètre. Cette technique permet d'augmenter de deux ordres de grandeurs le nombre de points que le système peut résoudre. Un système résolvant 2 100 000 différent points a ainsi été démontré; un record absolu dans le domaine des capteurs à fibre répartis.

Dans un chapitre séparé, nous discutons des limitations pour augmenter le nombre de points ainsi que des solutions possibles pour les contourner. Nous voyons aussi comment mitiger la dépendance de l'indice de réfraction de la fibre à la température via un algorithme capable de compenser cet effet.

Dans le dernier chapitre, les applications possibles du réseau Brillouin dynamique sont étudiées. Un modèle théorique du BDG dans des fibres à maintien de polarisation, capable de calculer la réflexion de l'impulsion sonde, est présenté Le modèle prend aussi en compte le cas d'une biréfringence non-uniforme le long de la fibre.

Les réseaux dynamiques sont utilisés pour crée un flip-flop –- une mémoire tout-

optique commutable avec une impulsion lumineuse. L'effet est démontré sur une fibre de 1 mètre de long, correspondant à un temps de stockage de 10 ns. Le modèle théorique permet la mesure de la variation de la biréfringence le long d'une fibre optique. Une étude préliminaire des propriétés spectrales des réseaux dynamiques est effectuée, ainsi qu'un modèle permettant de prédire la réponse spectrale d'un BDG uniforme. Nous montrons que nous pouvons modifier les propriétés spectrales d'un BDG en changeant les spectres des ondes optiques utilisées pour sa génération.

Nous allons conclure par une discussion, résumant tout le travail théorique et expérimental effectué durant cette thèse. Des applications possibles des travaux de résultats présentés sont proposées ainsi que les perspectives pour des activités de recherches futures.

Mots-clés: fibre optique, effets non linéaires dans les fibres optiques, diffusion Brillouin, réseau Brillouin dynamique, capteurs à fibre optiques, traitement du signal optique

Contents

List of Figures

Introduction

Fibre Bragg gratings have a very broad range of applications, including spectral filtering, dispersion compensation, reflectors for fibre lasers, optical sensing. While there is some potential of tuning properties of an FBG after it has been manufactured (via strain [1, 2] or temperature [3]), the capability of all the methods is quite limited. Brillouin dynamic gratings (BDG's) offer a much broader versatility; being generated by two optical waves, they can be created and destroyed within some tens of nanoseconds. Their length can vary from several millimetres up to tens or even hundreds of metres – while the length of traditional FBG's is so far limited to about ten centimetres. Both short and long BDG's can be used for distributed sensing [4, 5] and signal processing [6–8]; multiple gratings can be generated within a single fibre for more complex applications [6, 9].

Exploiting the same process, Brillouin fibre sensing became a mature technology – the result of more than two decades of intense research and development. One of the techniques that offers the highest performance, and thus provides the largest number of resolved points, is called Brillouin optical time-domain analysis (BOTDA) [10]. It has shown clear advantages with respect to systems based on discrete sensing elements, e.g. fibre Bragg gratings – a single distributed system is able to interrogate a large number of independent points (given by the quotient between the sensing range and the spatial resolution) along an optical fibre. This feature gives unique opportunities to monitor, for instance, large civil structures or very long pipelines in the oil & gas industry, where a large number of resolved points is typically required.

Using an optimised conventional BOTDA scheme the sensing range can reach 50 km with the limitation given by fibre losses of $0.2\,\mathrm{dB\,km^{-1}}$. Several techniques are used to extend the measurement distance. Raman amplification can be used to compensate for fibre losses by introducing distributed amplification along the sensing fibre [11–14]. Optical pulse coding techniques use multiple pump pulses to bypass power limitations given by nonlinear effects [15–20]. Mathematical algorithms are further used to process multiple measurements, combining them into a single one with an improved signal-to-noise ratio (SNR). Using either of these techniques or a combination of them [15, 21, 22] the measurement range was expended beyond 100 km. However, since optical losses scale exponentially with fibre length it is not the best way to significantly improve the number

of measured points. For example an increase in measurement distance from 100 km to 125 km introduces the same decrease in SNR as a change from 25 km to 50 km. Yet, the relative change in the number of measured points is four times less (25 % against 100 %).

As for the spatial resolution, for a BOTDA system is ultimately limited down to 1 m by the acoustic-wave response time [23]. Such methods as correlation-domain [4, 24, 25], acoustic pre-activation [26, 27], or differential pulses [28, 29], have allowed the spatial resolution to be improved down to the order of centimetres or millimetres, but only along restricted fibre lengths (less than 5 km-long). Brillouin optical correlation-domain analysis (BOCDA) so far has shown the best spatial resolution of 1.6 mm [30]. Yet, this technique has an intrinsic correlation between the spatial resolution and the sensing distance. Attempts have been made to overcome this limitation, but so far the number of resolved points in these sensors has not exceeded 24 000 [31].

In general, until recently the number of points achievable by distributed Brillouin sensors was limited to about 100 000 [32], e.g. sensing with 1 m spatial resolution over a 120 km distance [15], or 5 cm resolution over 5 km [29].

A new approach is required to increase the number of points by either expanding the sensing distance or improving the spatial resolution. Both directions have their own difficulties and limitations that have to be addressed separately, especially when one tries to combine high spatial resolution with long sensing distance. A technique based on phase correlation was introduced for sensing with high spatial resolution over short distances and immediately showed 20 000 measured points [4], a more than three times improvement over BOCDA. A further development, though, was impeded by a linear relation between the noise and the measurement distance.

This work shows how introduction of time-gating [33] and time-domain measurement [34] allowed for a two order of magnitude improvement in the number of measured points, leading to a sensor capable of resolving more than 2 000 000 separate points – exceeding a symbolic milestone of 1 000 000 points and outperforming any existing system in number of resolved points.

As it was said before, application of Brillouin dynamic gratings is by no means limited to distributed sensing. Brillouin dynamic gratings can be generated in polarisation-maintaining (PM) fibres, showing multiple application in optical and microwave signal processing. Optical signal integration and differentiation [7, 35] has been demonstrated along with the true time-reversal of an optical signal [8]. Delay lines for optical signals were shown [36, 37] and true time delay of microwave signals has been demonstrated [36].

For a long time research activities have been carried out to create all-optical logic circuits and other components which will potentially enable creation of an all-optical computer. One of the required elements is a flip-flop – a memory switch, that can be turned on and off by optical means. Solutions were proposed based, for example, on microdisk lasers [38] and ring lasers [39]. We propose a method based on Brillouin dynamic gratings to create an all-optical flip-flop which is potentially scalable for storage times of

hundreds of nanoseconds.

As it was said before, classic fibre Bragg gratings have a limited tunability; the peak wavelength can be tuned by a mechanical strain or a temperature change but neither of the two methods offers the possibility to manipulate the spectral properties of the grating. The spectral characteristics of Brillouin dynamic gratings directly depend on the spectra of optical waves that generate them. Not only it allows for a fast tuning of the grating's frequency, but it can also be used to create gratings with complex spectra. This work shows the generation of Brillouin dynamic gratings with multiple spectra lines and combining closely positioned lines to create an optical band-pass filter. These results are preliminary but they already show what can be done easily and which problems arise for other, not so easily implemented applications.

It is important to have a mathematical model to support research activities. They allow careful planning of experimental work and predicting the problems that may arise. In this work for every experiment there will be a sufficient theoretical model designed for a specific application of BDG's. The ambition of this work is to be helpful for researchers who prepare to carry out research on Brillouin dynamic gratings to plan their work.

Chapter 1

Brillouin scattering

The origin of any scattering process is the inhomogeneity of the medium, i.e. fluctuations of some of its characteristics. For Rayleigh scattering, for example, these are the stationary fluctuations of the refractive index which scatter the light without changing its spectrum. Léon Brillouin considered the scattering of an optical wave on an acoustic wave – a moving oscillation of medium density. Results of his calculations became a part of a paper he published in 1922 [40]. Brillouin showed how reflection angle will depend on the acoustic wave frequency; he also demonstrated that the reflected light will be shifted spectrally due to the Doppler effect[1]:

$$(27) \quad \begin{cases} \dot{e}_y = -\, \mathrm{A}_y \dfrac{\partial k}{\partial \rho} \, \Delta_0 \Phi \, \dfrac{(2\pi n)^2}{8\pi \mathrm{D}c^2} \cos 2\pi \left((n + \mathrm{N})t_1 + \mathrm{N}\theta \right) \\[2ex] e_z = -\, \mathrm{A}_z \dfrac{\partial k}{\partial \rho} \, \Delta_0 \Phi \, \dfrac{(2\pi n)^2}{8\pi \mathrm{D}c^2} \cos 2\pi \left((n + \mathrm{N})t_1 + \mathrm{N}\theta \right) \end{cases}$$

"La formule (27) nous montre d'ailleurs que l'onde lumineuse réfléchie a une fréquence $(n + N)$ différente de la fréquence n de l'onde incidente; ceci s'explique, et provient de l'effet Döppler pendant la réflexion sur des miroirs MM (fig. 1) en mouvement avec une vitesse V_l."

Observation of Brillouin scattering in the stimulated regime requires a high-intensity coherent source of light, unavailable before the invention of lasers in 1960's. Thus, it was only in 1964 when Chiao *et al.* [42] were able to observe SBS in quartz and sapphire crystals. With development of fibre optics it was recognised to be a major factor, limiting the power that can be successfully used to send data. Yet, as it will be shown later, it has multiple useful applications.

---

[1]While there are reasons to believe that Soviet physicist Leonid Mandelstam has predicted the same effect in 1918, he has not published his results until 1926 [41].

While nonlinear optics covers multiple effects such as modulation instability, four-wave mixing, higher harmonic generation, etc., they are outside of the scope of this work and will only be mentioned briefly. All the theoretical models derived throughout this work consider only stimulated Brillouin scattering; if needed, a detailed information on nonlinear effects can be found in literature [43, 44].

1.1   Spontaneous Brillouin scattering

Spontaneous Brillouin scattering occurs on thermally activated acoustic waves inside the material. On the quantum level it is an interaction between a photon and an acoustic phonon. Let's consider a photon with frequency ν, energy $E_{\mathrm{phot}} = h\nu$, and wave vector $k = hn\nu/c$, where h is the Planck's constant, n is the refractive index and c is the light velocity. The phonon has frequency f, energy $E_{\mathrm{phon}} = hf$, and wave vector $q = hf/V_{\mathrm{a}}$, where V_{a} is the acoustic velocity in the material. Since the frequency of the phonon is negligible in comparison with the frequency of the phonon (10 GHz versus 200 THz), the energy of the phonon is also negligible in comparison to the one of the photon. Thus, during the interaction between the photon and the phonon one can consider the photon's energy and frequency to remain constant ($\Delta E_{\mathrm{phot}} \ll E_{\mathrm{phot}}$, $\Delta\nu \ll \nu$). From this also follows that the absolute value of the photon's wave vector doesn't change either; its direction, though, may change significantly.

Figure 1.1 depicts the scattering of a photon with the initial wave vector $\mathbf{k}_{\mathrm{i}}$ and the wave vector after the scattering $\mathbf{k}_{\mathrm{s}}$, with θ being the angle between those two wave vectors. The absolute value of the difference between the two wave vectors $|\Delta\mathbf{k}| = |\mathbf{k}_{\mathrm{s}} - \mathbf{k}_{\mathrm{i}}|$ increases with the scattering angle. The value of this wave vector change can be calculated easily:

$$\Delta k = 2k\sin(\theta/2)\,, \tag{1.1}$$

ranging from 0 to $2k$ for the scattering angle varying from 0 to π.

The change in the wave vector during the scattering process can be caused by two configurations in which the photon is interacting with a phonon having the wave vector equal to Δk given by equation (1.1):

$$q = 2k\sin(\theta/2)\,. \tag{1.2}$$

The first configuration is the interaction with a phonon propagating towards the photon ($\mathbf{k}_{\mathrm{i}}\mathbf{q} < 0$), as depicted on figure 1.2a. During this process the phonon is annihilated transferring its energy and momentum to the photon. In the second configuration the photon interacts with a phonon moving away from the photon ($\mathbf{k}_{\mathrm{i}}\mathbf{q} > 0$) as depicted on figure 1.2b. In this process a copy of the initial phonon is created, thus, the photon loses a part of its energy. These two processes are called anti-Stokes and Stokes scattering.
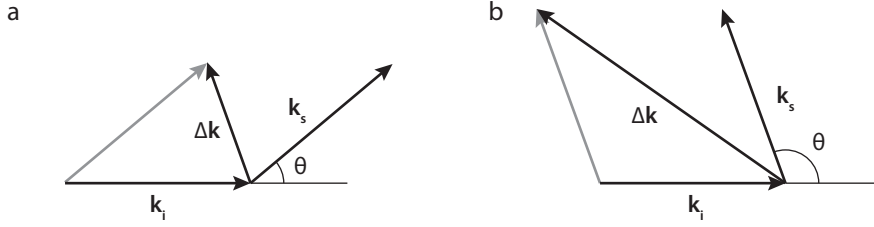
Figure 1.1: Change of photon's momentum in a scattering process for two scattering angles
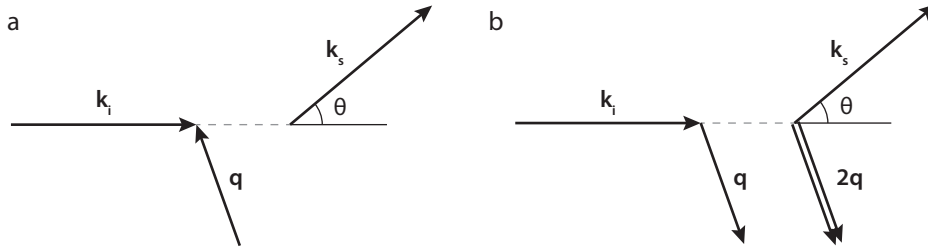
Figure 1.2: Spontaneous Brillouin scattering: a) anti-Stokes and b) Stokes processes

As a result of the scattering process the energy of the photon is changed by a value equal to the phonon's energy $\Delta E = qV_a = 2k\sin(\theta/2)V_a$ which leads to a change in the frequency:

$$\Delta\nu = 2\nu n V_a \sin(\theta/2)/c. \tag{1.3}$$

In the Stokes process a phonon is created, thus the photon's energy is decreased, while during the anti-Stokes scattering the energy transfer goes the opposite direction. Since in an optical fibre the light can propagate just in two directions, only the light scattered at angles 0 and π gets captured. From equation (1.3) follows that the light scattered forward ($\theta = 0$) experiences no frequency shift. In fact in can be seen from equation (1.2) that for $\theta = 0$ the phonon's wave vector and, therefore, frequency are equal to zero. This corresponds to the whole medium moving as a whole, creating no inhomogeneities. For the backscattered light the phonon's wave vector can be easily found to be equal to $2k$; giving the following change in photon's frequency

$$\Delta\nu = 2\nu n V_a/c, \tag{1.4}$$

which can be rewritten in terms of the wavelength to obtain the classic formula for the so-called Brillouin frequency shift:

$$\nu_B = 2n V_a/\lambda. \tag{1.5}$$

7

Rayleigh

Brillouin
stokes

Brillouin
anti-stokes

$v_0 - v_B$ v_0 $v_0 + v_B$
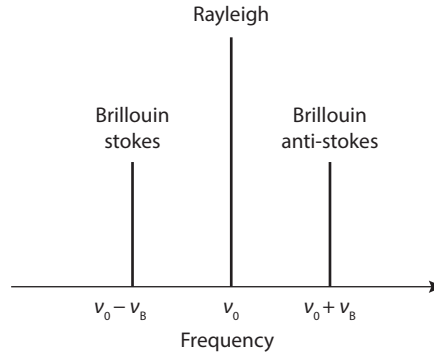
Frequency

Figure 1.3: Spectrum of the back-scattered light.

It can also be rewritten in a commonly used form for the angular frequency:

$$\Omega_B = 2nV_a\omega/c. \tag{1.6}$$

In a standard single-mode optical fibre (SMF) with refractive index $n = 1.44$ and acoustic velocity $V_a = 5.9\,\mathrm{km\,s^{-1}}$ the typical value of the Brillouin frequency shift is about $10.8\,\mathrm{GHz}$ at a wavelength of $1.5\,\mathrm{\mu m}$. The typical spectrum of the backscattered light can be seen on figure 1.3 showing the light scattered via Rayleigh (without a change in the frequency) and the Brillouin Stokes and anti-Stokes waves positioned at either side of it.

1.2 Stimulated Brillouin scattering

For small incident powers the intensity of the backscattered light is the same for Stokes and anti-Stokes waves. However, as the incident power grows, the Stokes wave becomes strong enough to affect the scattering process – the scattering changes from the spontaneous to the stimulated regime.

Stimulated Brillouin scattering (SBS) involves two counterpropagating optical waves with a small frequency shift. These waves are called throughout the text *the pump* and *the signal*; their respective angular frequencies are ω_p and ω_s; and the frequency difference between them is $\Omega = \omega_p - \omega_s$. Figure 1.4 shows how two waves interact with each other and the medium they propagate in. The pump and the probe interfere creating an optical intensity wave, which, due to a frequency difference between the pump and the signal, moves along the fibre. Electrostriction – material compression in the presence of the electric field – copies the optical intensity wave as a wave of compression, that leads to a change in the material density – an acoustic wave. A change in the material's density naturally leads to a change in the refractive index, and this periodic modulation of the refractive index works as a moving fibre Bragg grating resonant at the frequency of
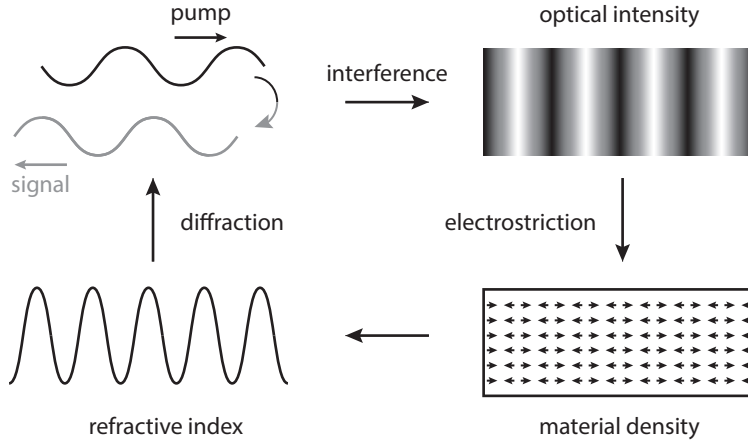
Figure 1.4: Self-sustained loop of the stimulated Brillouin scattering

the pump wave. Due to the Doppler effect the reflected light has a lower frequency that matches the one of the signal wave. Thus, the signal wave gets amplified enhancing the intensity wave and therefore the whole SBS process.

Let's derive equations that govern SBS. For simplicity we will neglect the transversal distribution of all the waves since normally it is of a small importance. The electrical field inside the fibre is given by the sum of the fields of the pump and the signal waves:

$$E(z, t) = E_{\mathrm{p}}(z, t) + E_{\mathrm{s}}(z, t)\,. \tag{1.7}$$

Electrical fields of the optical waves $E_{\mathrm{p}}(z, t)$ and $E_{\mathrm{s}}(z, t)$ can be written in the traditional form for electromagnetic waves, separating the oscillations at the optical frequency from the slowly varying complex amplitude:

$$E_{\mathrm{p}}(z, t) = A_{\mathrm{p}}(z, t)e^{j(k_{\mathrm{p}}z - \omega_{\mathrm{p}}t)} + \mathrm{c.c.}\,, \tag{1.8}$$

$$E_{\mathrm{s}}(z, t) = A_{\mathrm{s}}(z, t)e^{j(-k_{\mathrm{s}}z - \omega_{\mathrm{s}}t)} + \mathrm{c.c.}\,, \tag{1.9}$$

where A_{p} and A_{s} are the complex amplitudes of the two waves and $k_{\mathrm{p,s}}$ are the wave vectors of the pump and the signal. A similar equation can be written for the material density:

$$\rho_{\mathrm{tot}}(z, t) = \rho_0 + \Delta\rho(z, t) = \rho_0 + \left[Q(z, t)e^{j(qz - \Omega t)} + \mathrm{c.c.} \right]\,, \tag{1.10}$$

where Ω is the above-mentioned frequency difference between the pump and the signal, ρ_0 is the mean density of the medium, and Q is the complex amplitude of the acoustic wave.

9

1.2.1 Acoustic wave

In order to derive equations that govern the evolution of the acoustic wave during the SBS process, we start with the wave equation (see, for example, Section 9.3 of Boyd's Nonlinear Optics [43]):

$$\frac{\partial^2 \rho_{\text{tot}}(z,t)}{\partial t^2} - \Gamma' \nabla^2 \frac{\partial \rho_{\text{tot}}(z,t)}{\partial t} - V_{\text{a}}^2 \nabla^2 \rho_{\text{tot}}(z,t) = \nabla \cdot \mathbf{f}(z,t) \,, \qquad (1.11)$$

where Γ' is the damping parameter, responsible for the decay of the acoustic wave, and $\mathbf{f}$ is the force per unit volume, which in this case comes from the electrostriction. Note that in this equation we do not consider Langevin's terms which give the thermal excitation of phonons [45], assuming them to be much smaller than $\nabla \cdot \mathbf{f}$. Let's rewrite the three terms on the left side using equation (1.10) and remembering that we consider only longitudinal changes, thus $\nabla Q = \partial Q / \partial z$ (here and further, arguments z and t are omitted for a better readability):

$$\frac{\partial^2 \rho_{\text{tot}}}{\partial t^2} = \left(\frac{\partial^2 Q}{\partial t^2} - 2j\Omega \frac{\partial Q}{\partial t} - \Omega^2 Q \right) e^{j(qz-\Omega t)} + \text{c.c.} \,, \qquad (1.12)$$

$$\Gamma' \nabla^2 \frac{\partial \rho_{\text{tot}}}{\partial t} = \Gamma' \nabla^2 \left(\frac{\partial Q}{\partial t} - j\Omega Q \right) e^{j(qz-\Omega t)} + \text{c.c.} =$$
$$\Gamma' \left(\frac{\partial^2}{\partial z^2} \frac{\partial Q}{\partial t} + 2jq \frac{\partial}{\partial z} \frac{\partial Q}{\partial t} - q^2 \frac{\partial Q}{\partial t} - j\Omega \frac{\partial^2 Q}{\partial z^2} + 2\Omega q \frac{\partial Q}{\partial z} + j\Omega q^2 Q \right) e^{j(qz-\Omega t)} + \text{c.c.} \,,$$
$$(1.13)$$

$$V_{\text{a}}^2 \nabla^2 \rho_{\text{tot}} = V_{\text{a}}^2 \left(\frac{\partial^2 Q}{\partial z^2} + 2jq \frac{\partial Q}{\partial z} - q^2 Q \right) e^{j(qz-\Omega t)} + \text{c.c.} \qquad (1.14)$$

Assuming that the acoustic wave amplitude varies slowly in space and time, we can omit higher order derivatives, significantly simplifying equations (1.12)–(1.14):

$$\frac{\partial^2 \rho_{\text{tot}}}{\partial t^2} \approx \left(-2j\Omega \frac{\partial Q}{\partial t} - \Omega^2 Q \right) e^{j(qz-\Omega t)} + \text{c.c.} \,, \qquad (1.15)$$

$$\Gamma' \nabla^2 \frac{\partial \rho_{\text{tot}}}{\partial t} \approx \Gamma' \left(-q^2 \frac{\partial Q}{\partial t} + 2\Omega q \frac{\partial Q}{\partial z} + j\Omega q^2 Q \right) e^{j(qz-\Omega t)} + \text{c.c.} \,, \qquad (1.16)$$

$$V_{\text{a}}^2 \nabla^2 \rho_{\text{tot}} \approx V_{\text{a}}^2 \left(2jq \frac{\partial Q}{\partial z} - q^2 Q \right) e^{j(qz-\Omega t)} + \text{c.c.} \qquad (1.17)$$

The right term of equation (1.11) – the divergence of the force per unit volume – can be calculated knowing that the force per unit volume is given by the gradient of the strictive pressure p_{st}:

$$\mathbf{f} = \nabla p_{\text{st}} = \frac{\partial p_{\text{st}}}{\partial z} \,. \qquad (1.18)$$

The strictive pressure comes from the electrostrictive effect due to the presence of two optical waves:

$$p_{st} = -\frac{1}{2}\epsilon_0\gamma_e \left\langle E^2 \right\rangle . \tag{1.19}$$

Using equations (1.8) and (1.9) and considering the amplitudes of the pump and the signal waves to be constant the force per unit volume can be derived

$$\begin{aligned}
\mathbf{f} &= -\frac{1}{2}\epsilon_0\gamma_e\frac{\partial}{\partial z}\left(2A_pA_s^*e^{j(qz-\Omega t)} + \text{c.c.}\right)\mathbf{z} \\
&= -jq\epsilon_0\gamma_e\left(A_pA_s^*e^{j(qz-\Omega t)} + \text{c.c.}\right)\mathbf{z},
\end{aligned} \tag{1.20}$$

where $\mathbf{z}$ is the unit vector along z axis. Calculating the divergence of this term is straightforward:

$$\nabla\mathbf{f} = q^2\epsilon_0\gamma_e A_pA_s^*e^{j(qz-\Omega t)} + \text{c.c.} . \tag{1.21}$$

Now we can insert the results of equations (1.15)–(1.17) and (1.21) into equation (1.11). Since the multiplier $e^{j(qz-\Omega t)}$ and the complex conjugate are present in each term, both can be omitted in calculations:

$$\begin{aligned}
\frac{\partial Q}{\partial t}(-2j\Omega + \Gamma'q^2) - \frac{\partial Q}{\partial z}(2\Omega\Gamma'q + 2jV_a^2q) \\
+ Q(-\Omega^2 - j\Omega\Gamma'q^2 + V_a^2q^2) = q^2\epsilon_0\gamma_e A_pA_s^* .
\end{aligned} \tag{1.22}$$

This equation can be simplified even further. First, we introduce $\Gamma_B = \Gamma'q^2$ – the damping coefficient of the acoustic wave ($\Gamma_B \ll \Omega_B, \Omega$). Next, we remember that $q = 2k$ and therefore V_aq is equal to the angular Brillouin frequency given by equation (1.6)

$$V_aq = 2V_ak = \frac{2nV_a\omega}{c} = \Omega_B . \tag{1.23}$$

Keeping this in mind the left part of equation (1.22) can be rewritten

$$\begin{aligned}
\frac{\partial Q}{\partial t}(-2j\Omega + \Gamma'q^2) - \frac{\partial Q}{\partial z}(2\Omega\Gamma'q + 2jV_a^2q) + Q(-\Omega^2 - j\Omega\Gamma'q^2 + V_a^2q^2) \\
= -2j\Omega\frac{\partial Q}{\partial t} - 2jV_a^2q\frac{\partial Q}{\partial z} + (\Omega_B^2 - \Omega^2 - j\Omega\Gamma_B)Q .
\end{aligned} \tag{1.24}$$

In the first term $\Gamma'q^2 = \Gamma_B \ll 2\Omega$. The second term can be fully ignored as the acoustic wave propagates only several micrometres before fully decaying:

$$-2j\Omega\frac{\partial Q}{\partial t} + \left(\Omega_B^2 - \Omega^2 - j\Omega\Gamma_B\right)Q = \epsilon_0\gamma_e q^2 A_pA_s^* . \tag{1.25}$$

Let's introduce frequency detuning parameter

$$\Gamma_A = j\frac{\Omega_B^2 - \Omega^2 - j\Omega\Gamma_B}{2\Omega}\,, \tag{1.26}$$

and electrostrictive coupling coefficient

$$g_1 = \frac{\epsilon_0 \gamma_e q^2}{2\Omega}\,. \tag{1.27}$$

Using these two and reintroducing arguments z and t we obtain the final equation for the acoustic wave amplitude:

$$\frac{\partial Q(z,t)}{\partial t} + \Gamma_A Q(z,t) = jg_1 A_p(z,t)A_s^*(z,t)\,. \tag{1.28}$$

The term $A_p(z,t)A_s^*(z,t)$ can be rewritten:

$$A_p(z,t)A_s^*(z,t) = |A_p(z,t)||A_s(z,t)|e^{j\Delta\phi}\,, \tag{1.29}$$

where $\Delta\phi$ is the phase difference between the pump and the signal waves.

1.2.2 Optical waves

The optical waves have to fulfil the wave equation as well:

$$\frac{\partial^2 E(z,t)}{\partial z^2} - \frac{1}{v_g^2}\frac{\partial^2 E(z,t)}{\partial t^2} = \frac{1}{\epsilon_0 c^2}\frac{\partial^2 P(z,t)}{\partial t^2}\,, \tag{1.30}$$

where v_g is the optical group velocity and P is the total nonlinear polarization:

$$P = \epsilon_0 \Delta\chi E(z,t) = \epsilon_0 \Delta\epsilon E(z,t) = \epsilon_0 \rho_0^{-1}\gamma_e \Delta\rho E(z,t)\,, \tag{1.31}$$

where ϵ_0 is the dielectric permittivity of free space and γ_e is the electrostrictive coefficient of the material. The two terms of P that are phase-matched with the pump and the signal waves are[2]:

$$P_p = \epsilon_0 \gamma_e \rho_0^{-1} Q A_s e^{j(k_p z - \omega_p t)} + \text{c.c.}, \tag{1.32}$$

$$P_s = \epsilon_0 \gamma_e \rho_0^{-1} Q^* A_p e^{j(-k_s z - \omega_s t)} + \text{c.c.} \tag{1.33}$$

---

[2] As before, arguments z and t are left out until the final equations are obtained

Inserting these into equation (1.30) and assuming slowly varying amplitudes, equations can be written for amplitudes of the pump and the signal:

$$\frac{\partial A_{\mathrm{p}}}{\partial z} + \frac{1}{v_{\mathrm{g}}}\frac{\partial A_{\mathrm{p}}}{\partial t} = \frac{j\omega\gamma_e}{4nc\rho_0}A_{\mathrm{s}}Q\,, \tag{1.34}$$

$$-\frac{\partial A_{\mathrm{s}}}{\partial z} + \frac{1}{v_{\mathrm{g}}}\frac{\partial A_{\mathrm{s}}}{\partial t} = \frac{j\omega\gamma_e}{4nc\rho_0}A_{\mathrm{p}}Q^*\,. \tag{1.35}$$

Let's introduce the elasto-optic coefficient

$$g_2 = \frac{\omega\gamma_e}{2nc\rho_0}\,, \tag{1.36}$$

and write the equations in the final form:

$$\frac{\partial A_{\mathrm{p}}(z,t)}{\partial z} + \frac{1}{v_{\mathrm{g}}}\frac{\partial A_{\mathrm{p}}(z,t)}{\partial t} = j\frac{g_2}{2}A_{\mathrm{s}}(z,t)Q(z,t)\,, \tag{1.37}$$

$$\frac{\partial A_{\mathrm{s}}(z,t)}{\partial z} - \frac{1}{v_{\mathrm{g}}}\frac{\partial A_{\mathrm{s}}(z,t)}{\partial t} = -j\frac{g_2}{2}A_{\mathrm{p}}(z,t)Q^*(z,t)\,. \tag{1.38}$$

1.2.3 Small gain approximation

In the general case equations (1.28), (1.37) and (1.38) describing the evolution of the acoustic and optical waves cannot be solved analytically. However, when several reasonable approximations are made a solution can be found. This subsection will consider the simple case of small gain. First, let's consider the system to be in a steady state, meaning that the amplitudes of the optical and the acoustic waves do not change in time. Second, let's assume that the interaction between pump and signal is negligible, meaning that *i)* the pump amplitude remains constant and *ii)* the change in signal amplitude is very small $\Delta A_{\mathrm{s}} \ll A_{\mathrm{s},0}$ (where $A_{\mathrm{s},0}$ is signal wave's amplitude on the input of the fibre). Under these conditions equations (1.28) and (1.38) can be rewritten:

$$\Gamma_{\mathrm{A}}Q(z) = jg_1 A_{\mathrm{p}}A_{\mathrm{s}}^*(z)\,, \tag{1.39}$$

$$\frac{\partial A_{\mathrm{s}}(z)}{\partial z} = -j\frac{g_2}{2}A_{\mathrm{p}}Q^*(z)\,. \tag{1.40}$$

Equation (1.39) can be easily solved in the constant signal approximation, obtaining the asymptotic acoustic wave amplitude:

$$Q_{\mathrm{as}} = \frac{jg_1 A_{\mathrm{p}}A_{\mathrm{s},0}^*}{\Gamma_{\mathrm{A}}}\,. \tag{1.41}$$

Inserting this result into equation (1.40):

$$\frac{\partial A_s(z)}{\partial z} = -j\frac{g_2}{2}A_p Q_{as}^*,\tag{1.42}$$

which can be immediately solved to find the (small) change in the signal amplitude along a fibre with length d:

$$\Delta A_s = \frac{g_1 g_2 A_{s,0}|A_p|^2 d}{2\Gamma_A}.\tag{1.43}$$

Normally the intensity of the signal is detected:

$$\begin{aligned}I_s &= A_s A_s^* = (A_{s,0}+\Delta A_s)(A_{s,0}+\Delta A_s)^*\\ &\approx I_{s,0} + 2\operatorname{Re}(A_{s,0}\Delta A_s^*),\end{aligned}\tag{1.44}$$

where $I_{s,0} = |A_{s,0}|^2$ is the initial signal intensity. The change in signal's intensity can be calculated using equation (1.43) and remembering equation (1.26) for Γ_A:

$$\Delta I_s = g_1 g_2 I_p I_{s,0} d \operatorname{Re}\left(\frac{2j\Omega}{\Omega_B^2 - \Omega^2 - j\Omega\Gamma_B}\right).\tag{1.45}$$

Let's calculate the last multiplier of this equation:

$$\operatorname{Re}\left(\frac{2j\Omega}{\Omega_B^2 - \Omega^2 - j\Omega\Gamma_B}\right) = \operatorname{Re}\left(\frac{2j\Omega(\Omega_B^2 - \Omega^2 - j\Omega\Gamma_B)}{(\Omega_B^2 - \Omega^2)^2 + \Omega^2\Gamma_B^2}\right) = \frac{2\Omega^2\Gamma_B}{(\Omega_B^2 - \Omega^2)^2 + \Omega^2\Gamma_B^2}.\tag{1.46}$$

The frequency difference Ω between the pump and the probe is normally close to the Brillouin frequency shift, therefore we can consider $\Omega \approx \Omega_B$ and $\Omega + \Omega_B \approx 2\Omega$. Using $\Omega_B^2 - \Omega^2 = (\Omega_B + \Omega)(\Omega_B - \Omega)$ equation (1.46) can be rewritten and simplified:

$$\frac{2\Omega^2\Gamma_B}{(\Omega_B^2 - \Omega^2)^2 + \Omega^2\Gamma_B^2} = \frac{2\Omega^2\Gamma_B}{4\Omega^2(\Omega_B - \Omega)^2 + \Omega^2\Gamma_B^2} = \frac{\Gamma_B/2}{(\Omega_B - \Omega)^2 + (\Gamma_B/2)^2}.\tag{1.47}$$

Inserting this result in equation (1.45) it's possible to obtain the final equation for the detected change in the signal for the small gain approximation:

$$\Delta I_s = g_1 g_2 I_p I_{s,0} d \frac{\Gamma_B/2}{(\Omega_B - \Omega)^2 + (\Gamma_B/2)^2}.\tag{1.48}$$

Equation (1.48) shows that the signal's gain is linearly proportional to the interaction length and has a Lorentzian spectrum, centred at Ω_B with the full width at half maximum of Γ_B. The shape of this spectrum is shown on figure 1.5.
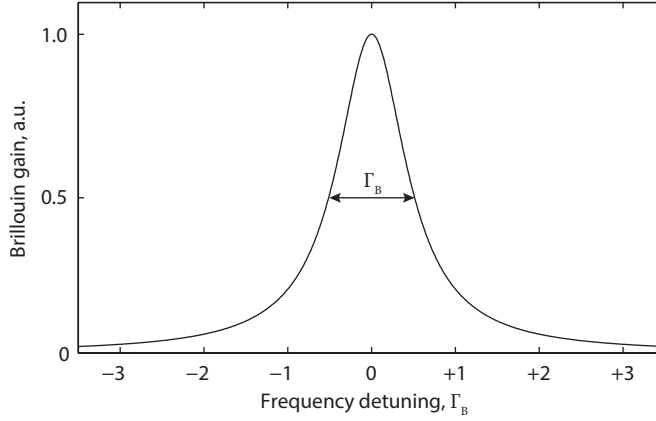
Figure 1.5: Brillouin gain shape.

1.3 Temperature/strain dependence of the SBS

Let's see how Brillouin frequency shift depends on temperature and staring of the medium. Starting with equation (1.5) for the Brillouin frequency shift let's write corresponding derivatives:

$$\nu_{\mathrm{B}} = \frac{2nV_{\mathrm{a}}}{\lambda} \,, \tag{1.49}$$

$$\frac{\partial \nu_{\mathrm{B}}}{\partial T} = \frac{2}{\lambda} \left(V_{\mathrm{a}} \frac{\partial n}{\partial T} + n \frac{\partial V_{\mathrm{a}}}{\partial T} \right) = \nu_{\mathrm{B}} C_T \,, \tag{1.50}$$

$$\frac{\partial \nu_{\mathrm{B}}}{\partial \epsilon} = \frac{2}{\lambda} \left(V_{\mathrm{a}} \frac{\partial n}{\partial \epsilon} + n \frac{\partial V_{\mathrm{a}}}{\partial \epsilon} \right) = \nu_{\mathrm{B}} C_\epsilon \,, \tag{1.51}$$

where C_T and C_ϵ are temperature and strain coefficients, respectively. These coefficients depend on the composition of the fibre (amount and type of dopant used), but the typical values are 1.1 MHz/K to 1.3 MHz/K for temperature [46, 47] and 0.055 MHz/μϵ for strain dependence [46, 48]. Thus, if the fibre strain remains constant, a change in Brillouin frequency can be directly translated into a change of the temperature; alternatively, for a constant temperature, a change in the Brillouin frequency gives a change in the strain. This opens a possibility for using Brillouin scattering to detect a change in temperature or strain. Moreover, if Brillouin scattering is localised in one way or another, this measurement can be done in a distributed way.

Chapter 2

Phase-correlated sensing

In order to create a distributed Brillouin sensor the interaction between the two optical waves has to be localised. In time-domain systems: Brillouin optical time-domain reflectometry (BOTDR) and Brillouin optical time-domain analysis (BOTDA), it is achieved by using a pulsed wave [10, 48, 49]. This localises the interaction to the section of the fibre overlapping with the pulse at a given moment, not unlike in traditional optical time-domain reflectometry setups, based on Rayleigh scattering.

In traditional correlation-based techniques (BOCDA, BOCDR) the interaction is localised through correlation between frequencies of the pump and the signal [24]. While this technique has shown an impressive spatial resolution [30, 50], it has an intrinsic limitation of the number of resolved points. This chapter introduces phase-correlation technique that relies on modifying the phases of two interacting waves. As it was shown in section 1.2.1, the Brillouin interaction depends on the phase difference between the two interacting waves. This opens a possibility of using phase modulation of these waves to localise the interaction between them.

2.1 Localising the Brillouin interaction by phase modulation

Let's consider pump and signal waves with phases modulated by a pseudo-random bit sequence (PRBS) that applies a phase shift of either 0 or π. Stimulated Brillouin scattering is based on the interference between the pump and the signal and therefore it depends on the phase difference between the two waves. Figure 2.1a shows phases of phase-modulated pump and signal at three moments of time. We can see that in the centre phases of two waves are perfectly correlated and always take the same value while at other positions phases of the two waves are absolutely uncorrelated. This leads to the acoustic wave being efficiently generated only at the correlation point, and outside of it the acoustic wave amplitude changes randomly never reaching the steady state (figure 2.1b).
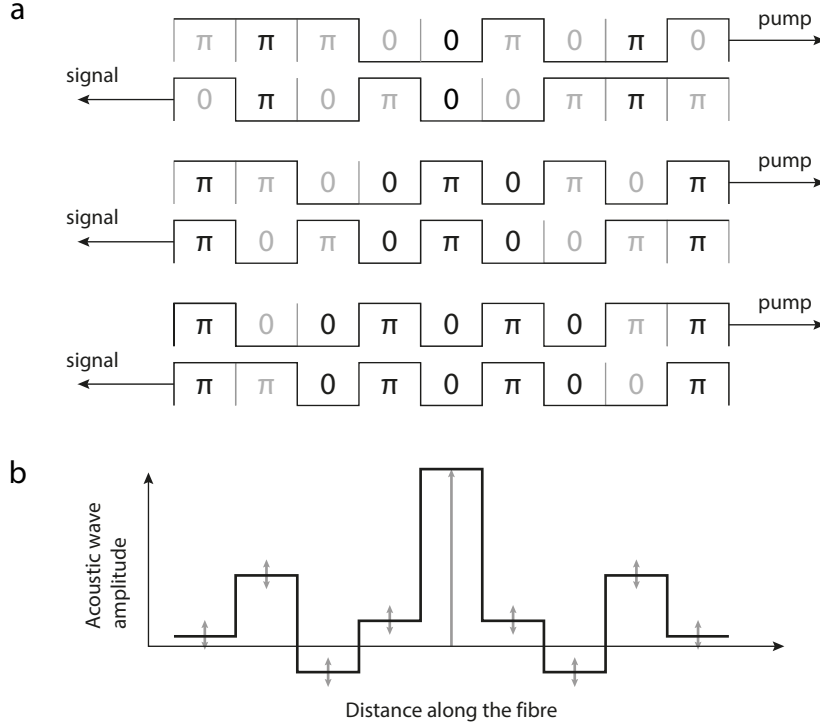
Figure 2.1: a) Counterpropagating phase-coded pump and signal waves. Note that the phases of two waves are always the same at the correlation peak (black letters) while outside they change between the same and the opposite (grey letters); b) Resulting acoustic wave amplitude: stable in the correlation peak and oscillating outside of it.

To find how acoustic wave changes in time and how it interacts with the optical waves we start with defining $\Pi(t)$ – the rectangular function (see figure 2.2a):

$$\Pi(t) = \begin{cases} 0 & |t| > 1/2 \\ 1/2 & |t| = 1/2 \\ 1 & |t| < 1/2 \end{cases}, \tag{2.1}$$

and through it we define function $f_{\mathrm{PRBS}}(t)$ based on a pseudo-random bit sequence (PRBS):

$$f_{\mathrm{PRBS}}(t) = \sum_q \xi_q \Pi\big((t - qT_{\mathrm{bit}})/T_{\mathrm{bit}}\big), \tag{2.2}$$

where ξ_q is a pseudo-random sequence of zeroes and ones with the period of N_{bits}; thus, $\xi_q \equiv \xi_{q+N_{\mathrm{bits}}}$. An example of $f_{\mathrm{PRBS}}(t)$ can be seen on figure 2.2b.
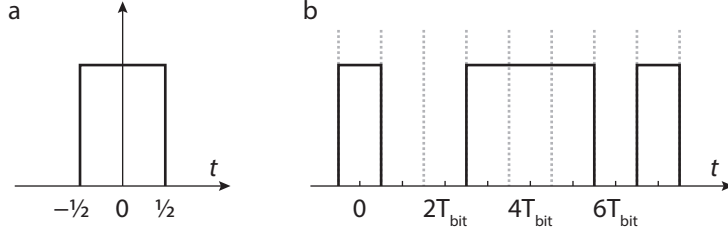
Figure 2.2: a) Rectangular function; b) PRBS based function $f_{\text{PRBS}}(t)$

Let's consider the pump and the signal – defined the same way as in section 1.2:

$$E_{\text{p}}(z,t) = A_{\text{p}}(z,t)e^{j(k_{\text{p}}z - \omega_{\text{p}}t)} + \text{c.c.} , \tag{2.3}$$

$$E_{\text{s}}(z,t) = A_{\text{s}}(z,t)e^{j(-k_{\text{s}}z - \omega_{\text{s}}t)} + \text{c.c.} , \tag{2.4}$$

and modulate their phases using $f_{\text{PRBS}}(t)$ applying a phase shift of 0 or π:

$$A_{\text{p,s}}\left[e^{j(k_{\text{p,s}}z - \omega_{\text{p,s}})} + \text{c.c.}\right] \longrightarrow A_{\text{p,s}}\left[e^{j(k_{\text{p,s}}z - \omega_{\text{p,s}})}e^{j\Delta\phi_{\text{p,s}}} + \text{c.c.}\right] , \tag{2.5}$$

$$\Delta\phi_{\text{p,s}} = \pi\, f_{\text{PRBS}}\left(t - t_{\text{p,s}}(z)\right) . \tag{2.6}$$

where $t_{\text{p,s}}(z)$ is given by the propagation time for the pump and the signal. Let's define the length of the sensing fibre L and consider the signal wave to be additionally delayed by t_{delay}. Setting the z-axis origin at the pump end of the fibre one can obtain the following equations for $t_{\text{p,s}}(z)$:

$$t_{\text{p}}(z) = \frac{k_{\text{p}}z}{\omega_{\text{p}}} \approx \frac{z n_{\text{eff}}}{c} , \tag{2.7}$$

$$t_{\text{s}}(z) = \frac{k_{\text{s}}(L - z)}{\omega_{\text{s}}} + t_{\text{delay}} \approx \frac{(L - z)n_{\text{eff}}}{c} + t_{\text{delay}} . \tag{2.8}$$

In these equations group refractive index is used; however, throughout this work an approximation of non-dispersive medium will be used, unless specified otherwise. Thus, the group and the phase refractive indices will be considered equal to each other.

As it was shown in section 1.2.1, the force affecting the acoustic wave (the right term in equation (1.19)) depends on the time average of the square of the total electrical field amplitude:

$$\begin{aligned}
E(z,t) = &A_{\text{p}}\left[e^{j(k_{\text{p}}z - \omega_{\text{p}}t)}e^{j\pi\, f_{\text{PRBS}}(t - t_{\text{p}}(z)(z))} + \text{c.c.}\right] \\
&+ A_{\text{s}}\left[e^{j(-k_{\text{s}}z - \omega_{\text{s}}t)}e^{j\pi\, f_{\text{PRBS}}(t - t_{\text{s}}(z)(z))} + \text{c.c.}\right] .
\end{aligned} \tag{2.9}$$

Taking the time average $\langle E^2 \rangle = \langle E E^* \rangle$ of equation (2.9) and keeping only the terms with the acoustic frequency one obtains the following result:

$$\langle E^2 \rangle = A_{\mathrm{p}} A_{\mathrm{s}}^* e^{j(qz-\Omega t)} \left\langle e^{j\pi [f_{\mathrm{PRBS}}(t-t_{\mathrm{p}}(z)) - f_{\mathrm{PRBS}}(t-t_{\mathrm{s}}(z))]} \right\rangle . \tag{2.10}$$

The complex exponential function to be averaged can take values of ± 1 depending on the difference between the phases of pump and signal, which takes values of 0 and π. It is easy to see that for $t_{\mathrm{p}} = t_{\mathrm{s}}$ the argument of the exponential function is equal to 0 at all the times. Due to the periodicity of the PRBS it also holds for propagation times differing by an integer number of PRBS periods:

$$t_{\mathrm{p}} = t_{\mathrm{s}} + m T_{\mathrm{bit}} N_{\mathrm{bits}} . \tag{2.11}$$

At other positions the phases are absolutely uncorrelated, meaning that the force responsible for the acoustic wave generation averages to zero. Combining equations (2.7), (2.8) and (2.11) it is possible to find positions of correlation peaks:

$$z_{\mathrm{c},m} = \frac{c}{2n_{\mathrm{eff}}} \left(m N_{\mathrm{bits}} T_{\mathrm{bit}} + t_{\mathrm{delay}} \right) + \frac{L}{2} . \tag{2.12}$$

As one can see, the separation between two correlation peaks $z_{\mathrm{sep}} = z_{\mathrm{c},m+1} - z_{\mathrm{c},m}$ is given by the product of the bit duration and the number of bits in the sequence:

$$z_{\mathrm{sep}} = \frac{c}{2n_{\mathrm{eff}}} N_{\mathrm{bits}} T_{\mathrm{bit}} . \tag{2.13}$$

Thus, unlike BOCDA and BOCDR techniques, it is possible to increase the separation between correlation peaks without changing the spatial resolution, by simply increasing the number of bit in the PRBS.

2.1.1 Scanning the position of the correlation peak

From equation (2.12) it can be seen that the position of a correlation peak can be changed by varying t_{delay} or T_{bit}. While the first method seems to be more logical and straightforward, it requires the use of either an optical delay or separate modulation systems for the pump and the signal waves. Both of these changes increase the complexity of the experimental setup; thus, the second method – varying T_{bit} – is the commonly used method in correlation-based setups. Though the spatial resolution is directly related to the bit duration, for high order correlation peaks (large values of m) the change ΔT_{bit} of the bit

duration required to scan the whole fibre length is very small.

$$\Delta z_{c,m} = \left(\frac{c}{2n_{\text{eff}}} (mN_{\text{bits}}(T_{\text{bit}} + \Delta T_{\text{bit}}) + t_{\text{delay}}) + \frac{L}{2} \right)$$
$$- \left(\frac{c}{2n_{\text{eff}}} (mN_{\text{bits}}T_{\text{bit}} + t_{\text{delay}}) + \frac{L}{2} \right) = L \,, \tag{2.14}$$

$$\frac{c}{2n_{\text{eff}}} mN_{\text{bits}}\Delta T_{\text{bit}} = L \,, \tag{2.15}$$

$$\Delta T_{\text{bit}} = \frac{2n_{\text{eff}}L}{cmN_{\text{bits}}} \,. \tag{2.16}$$

Using equation (2.13) for the separation between the correlation peaks it can be rewritten:

$$\Delta T_{\text{bit}} = \frac{L}{mz_{\text{sep}}} T_{\text{bit}} \,. \tag{2.17}$$

Since for unambiguous sensing only a single correlation peak can appear in the fibre the separation between the correlation peaks has to be longer than the sensing length $z_{\text{sep}} > L$ which allows to rewrite the previous equation:

$$\Delta T_{\text{bit}} < T_{\text{bit}}/m \,, \tag{2.18}$$
$$\Delta T_{\text{bit}}/T_{\text{bit}} < 1/m \,. \tag{2.19}$$

This way, using a high-order correlation peak ($m > 20$) the spatial resolution will change just by few percent during the scan of the whole fibre, negligibly affecting the spatial resolution of the system.

2.2 Spatial resolution

2.2.1 Correlation peak shape

In order to define the spatial resolution of a distributed sensor, its response to a temperature or strain perturbation has to be found. And to do that, the shape of the correlation peak (longitudinal distribution of the acoustic wave amplitude) has to be calculated. For a perfectly rectangular phase modulation of the pump and the signal waves it can be done analytically by solving equations (1.18) and (1.19) using equation (2.9) for the electrical field. Detailed calculations can be found in appendix A; they show that the correlation peak has a triangular shape with the bottom width given by the bit duration – 18 mm for the 90 ps bit duration used in the further experiment. This gives the value of the full width at half maximum (FWHM) of 9 mm, which is normally considered to be the spatial resolution of such sensors.
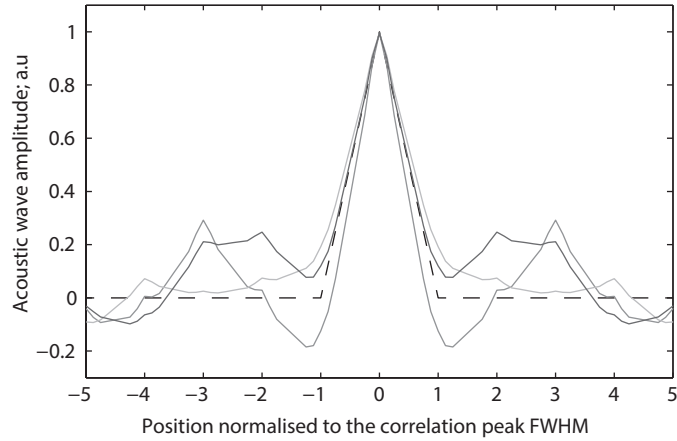
Figure 2.3: Acoustic wave amplitude in the vicinity of the correlation peak: average (dashed line) and several instantaneous values (solid lines). The horizontal axis is normalised to the correlation peak FWHM
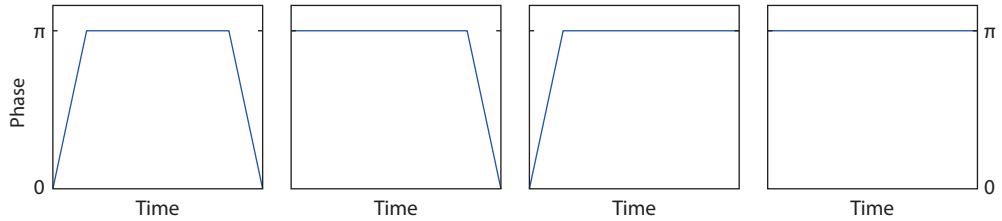
Figure 2.4: Phase patterns to concern when calculating the shape of the correlation peak.

It should be mentioned here that while the average amplitude of the acoustic wave has a triangular shape, the amplitude at a given time changes randomly, affecting the edges of the correlation peak as well. Figure 2.3 shows that the amplitude of gratings generated randomly outside of the correlation peak can easily reach one third of the correlation peak's amplitude.

In real life experiments the phase modulation is never perfect due to the limited bandwidth of the experimental setup components. For example, the PRBS generator used in our experiment has the typical 20 %–80 % transition time of 23 ps, while the bandwidth of the phase modulator is equal to 12 GHz. In this case the shape of the correlation peak has to be calculated numerically by simulating the counterpropagating waves. For simplicity we can assume that the phase changes linearly from 0 to π with the transition time of about 80 ps given by the phase modulator bandwidth. Note, that while for the case of
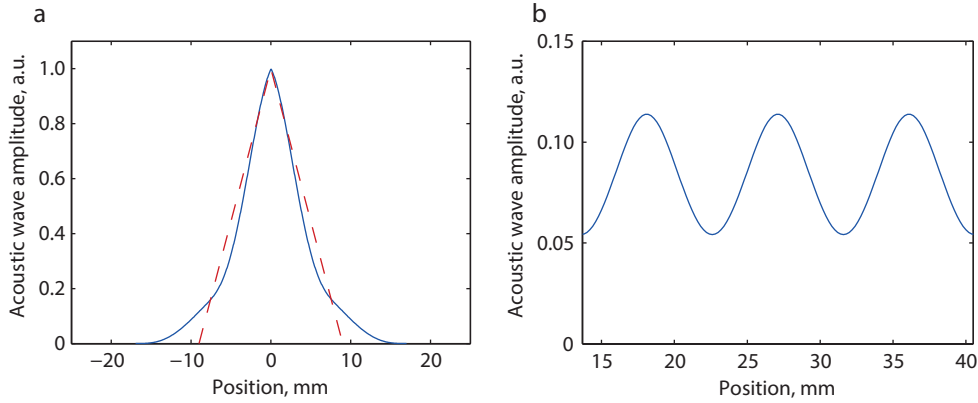
Figure 2.5: a) The shape of the correlation peak for perfect square phase modulation (dashed line) and imperfect modulation (solid line); b) Weak gratings caused by imperfect phase modulation.

a perfect modulation the shape of the correlation peak is given by the convolution of two rectangular functions, it is not enough to convolve two trapezoid phase pulses to find the shape of the correlation peak for the imperfect case. This convolution corresponds only to the case when phases of both waves switch at both sides of the bit. To find the real peak shape the convolution of all the patterns (see figure 2.4) have to be considered and the average of all the results taken as the final answer.

The result of this simulation is shown on figure 2.5a and are compared to the case of the perfect rectangular modulation. There is an obvious change in the correlation peak shape, the FWHM is decreased from 9 mm to 7.4 mm while the bottom is broadened from 18 mm to 28 mm. Another effect given by the non-instantaneous phase transition is the generation of stable weak gratings along the fibre. Figure 2.5b shows three connected consecutive gratings separated by 9 mm being generated outside the correlation peak (note that the vertical axis in figure 2.5b is normalised to the maximum amplitude of the correlation peak shown in figure 2.5a). It can be seen that the amplitude of these gratings varies from 5.5 % to 11 % of the correlation peak amplitude.

The reflectivity of each weak grating (given by the integral of the acoustic wave amplitude) is equal to ~15 % of the correlation peak reflectivity. Since the phases of pump and signal are uncorrelated at the weak gratings' positions, the direction of the energy transfer between the optical waves is random, adding a significant noise to the system. The accumulated noise from this effect is linearly proportional to the interaction length between pump and signal waves given by the pump pulse duration.

The change in the correlation peak shape and the presence of weak permanent gratings can be also explained by examining the spectrum of the phase-modulated light. Fig-
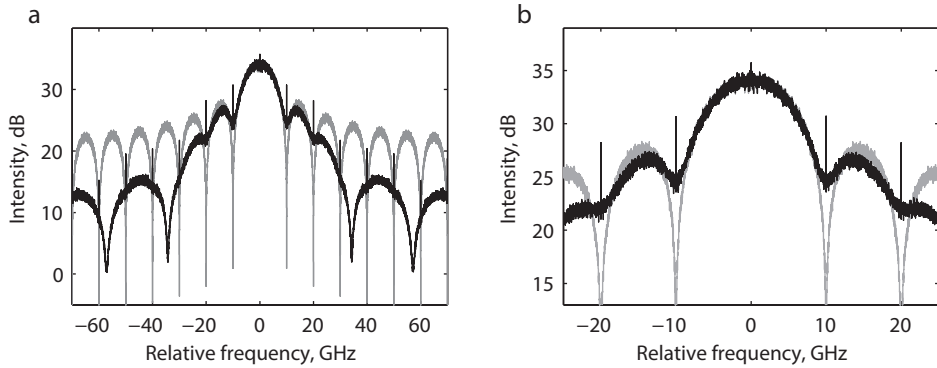
Figure 2.6: Theoretically calculated spectrum for light modulated with a PRBS with a 10 GHz bitrate for perfectly rectangular modulation (grey line) and non-instantaneous transition between phases (black line).

ure 2.6 shows the predicted spectrum for both perfect and imperfect modulation of phases. First, it can be seen that non-instantaneous transition between two phase values suppresses higher-order components of the spectrum, effectively making it narrower. This explains the broadening of the correlation peak. Additionally, strong lines appear at frequencies equal to the integer number of the bitrate – where the spectrum of the perfectly-modulated light goes down to zero. These lines generate the weak gratings which are separated by a distance proportional to the inverted bitrate.

2.2.2   Correlation peak response

Intuitively, the spatial resolution of the system is given by the smallest detectable perturbation. Let's consider a uniform fibre with a certain Brillouin frequency ν_0 and a uniform section of length d with a different, well-separated Brillouin frequency ν_h (referred hereafter as *hotspot*). In this configuration the gain at a frequency offset ν_0 sharply drops to zero in the hotspot position, while the gain at the frequency ν_h goes from zero to its maximum value. However, the measured gain values behave differently due to a finite spatial resolution of the system.

The gain response of the sensor is given by the convolution of the acoustic wave amplitude with a rectangular function given by the hotspot size. Figure 2.7 shows the simulated gain trace along the fibre for three distinct hotspot sizes, for frequencies ν_0 and ν_h. The shaded area of the correlation peak represents its convolution with the hotspot. Let's consider a hotspot detectable if the measured gain at ν_h exceeds the gain at ν_0 at some section of the fibre. Based on this, the three cases on figure 2.7 represent the conditions of undetectable, barely detectable, and well detected hotspots.

24
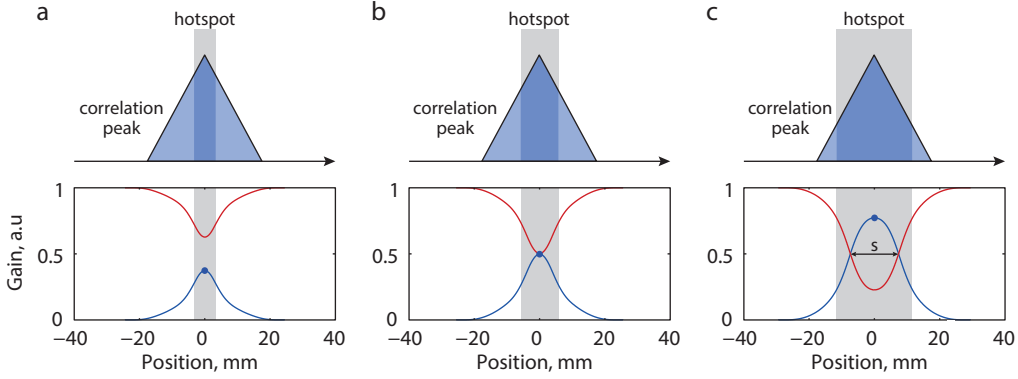
Figure 2.7: Simulated longitudinal Brillouin gain response for ν_0 (red line) and ν_H (blue line), around hotspots of different lengths: (a) short undetected, (b) barely detected, and (c) long well-detected hotspot.

2.2.3 Spatial resolution and sampling interval

It is important to remember that in a real system not only the spatial resolution is finite but so is the sampling interval. In order to reliably detect a hotspot, the sampling interval cannot be longer than the fibre section where the measured gain at ν_h exceeds the gain at ν_0, which is equivalent to gain at ν_h exceeding 0.5 (see s on figure 2.7c). If the sampling interval is longer than s – the hotspot detection range – the hotspot will not be reliably detected (the sampling can simply miss the hotspot detection region). Under this consideration, the hotspot presented on figure 2.7b is only theoretically detectable with a continuous sampling.

Having an analytical expression of the correlation peak shape allows us to derive an analytical expression for the gain response and the maximum sampling interval required by the system. In order to provide a general solution, independently of the specific bandwidth limitation of our PRBS generator, a triangular correlation peak will be considered in the following mathematical formulation.

Let's consider a hotspot with a given length δ and a triangular correlation peak with FWHM d that is offset from the hotspot centre by an arbitrary shift l (see top part of figure 2.8a). The shape of a correlation peak with integral equal to unity is given by

$$\rho(z) = \frac{1}{d}\left(1 - \left|\frac{z+l}{d}\right|\right),\tag{2.20}$$

for $-d \leq z + l \leq d$. The measured gain is given by the convolution between the correlation
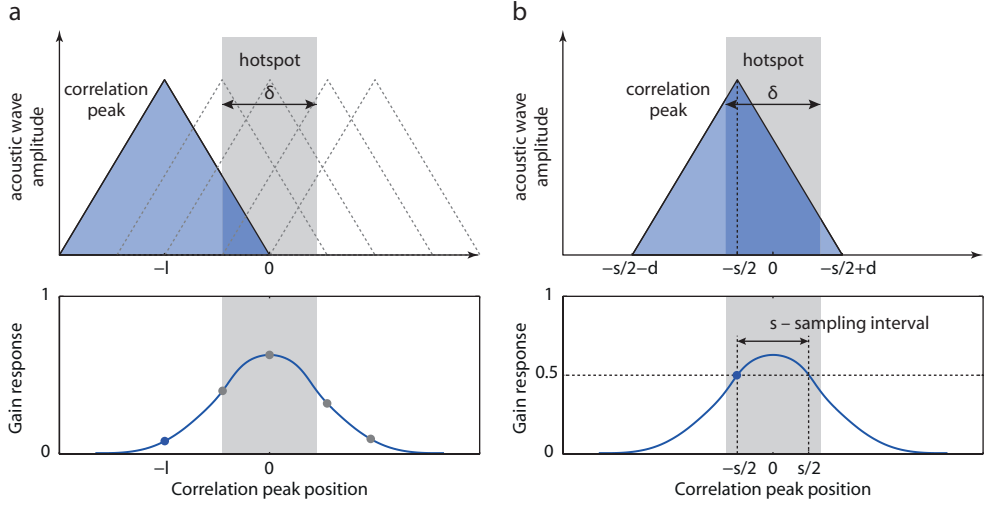
Figure 2.8: Calculating the gain response of a phase-correlation sensor for a triangular hotspot for a) general case and b) correlation peak is shifted from the hotspot by a half of the sampling interval.

peak and the hotspot:

$$\int_{-\delta/2}^{\delta/2} \frac{1}{d}\left(1 - \left|\frac{z+l}{d}\right|\right) dz\,. \tag{2.21}$$

The lower part of figure 2.8a shows the gain response calculated for several positions of the correlation peak. As it was said before, to find the sampling interval s that ensures detection of a hotspot with a given length δ, one has to find the point at which the gain reaches half of its maximum value (see figure 2.8b), which leads to the following equation:

$$\int_{-\delta/2}^{\delta/2} \frac{1}{d}\left(1 - \left|\frac{z+s/2}{d}\right|\right) dz = \frac{1}{2}\,. \tag{2.22}$$

The dark blue area on figure 2.8 represents the integral in the equation. Considering that the integral of the whole correlation peak is equal to 1, the sum of surfaces outside the correlation hotspot (light blue triangles in figure 2.8) has also to be equal to $1/2$. These triangles have bases $d - (s/2 + \delta/2)$ and $d - (-s/2 + \delta/2)$ for the left and the right one, respectively. Thus, their total surface can be easily found through triangle similarity, replacing the integral in equation (2.22):

$$\frac{1}{d^2}\left((d - \delta/2 - s/2)^2 + (d - \delta/2 + s/2)^2\right) = \frac{1}{2}\,. \tag{2.23}$$
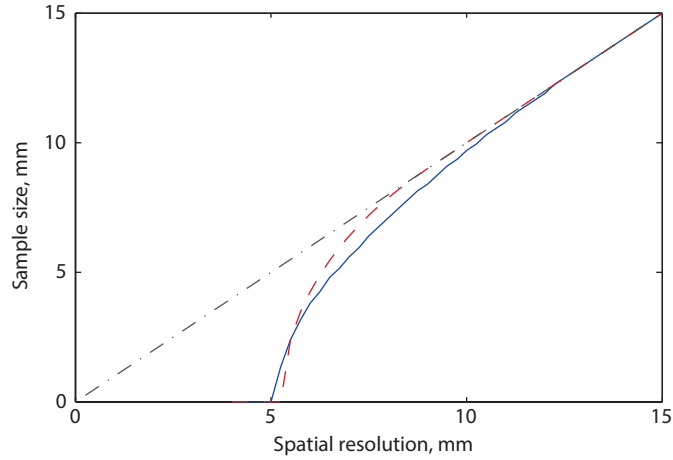
Figure 2.9: Minimum sampling interval required to obtain a given spatial resolution for the perfect square modulation (dashed red line) and the non-instantaneous phase modulation (solid blue line). The dash-dotted black line represents the asymptotic case commonly used in the state-of-the-art considering a sampling interval equal to the spatial resolution.

This equation can be easily solved for s:

$$s = \sqrt{-2d^2 + 4d\delta + \delta^2}\,. \tag{2.24}$$

Equation (2.24) gives the largest sampling interval s for a reliable detection of a hotspot of length δ using a correlation peak FWHM equal to d. This expression is valid for a hotspot size δ ranging from $2d(1 - 1/\sqrt{2})$, the smallest detectable hotspot size, up to the FWHM of the correlation peak d, at which the dependence reaches the asymptote $s = \delta$. The dashed line on figure 2.9 shows the result of this calculation for $d = 14\,\mathrm{mm}$. The best possible spatial resolution (the case presented at figure 2.7b) is equal to 5.2 mm.

For the case of nonistantaneous phase transition the relation between the sampling interval and the spatial resolution has to be derived numerically by convolving the correlation peak with the hotspot. The solid blue line in figure 2.9 shows the the result of this calculation; the best possible spatial resolution in this case is equal to 5 mm[1]. Generally, for a given spatial resolution a sensor with imperfect modulation requires a smaller sampling interval than the one with the perfectly rectangular phase modulation.

---

[1]It may look strange that the spatial resolution is slightly better for the imperfect modulation, but one needs to remember that the noise levels are higher for such a case, thus, the overall performance of the imperfect system is worse.
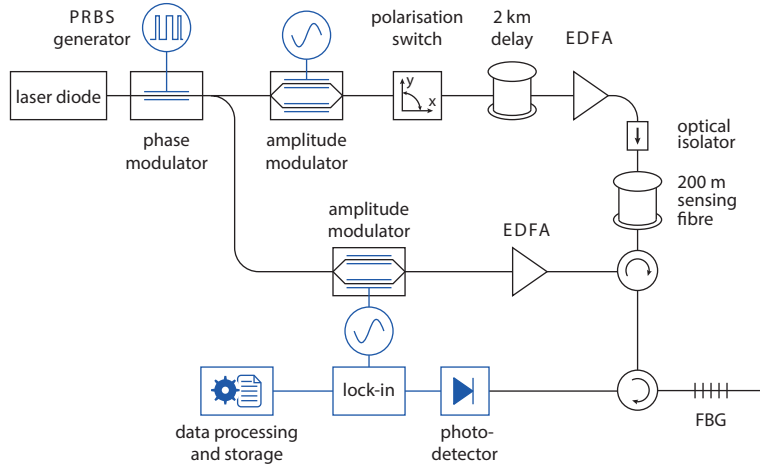
Figure 2.10: Experimental setup for phase-coding sensing

2.3 Experiment

2.3.1 Setup

The experimental implementation of the phase-correlated sensing technique is shown on figure 2.10. The output of a distributed-feedback diode laser (DFB) passes through a phase modulator driven by a PRBS generator. The clock of the generator was set to 11 GHz which corresponds to the bit duration of 90 ps. The phase-modulated light is split in two arms with a 50/50 fibre coupler. The bottom branch is used to generate the pump wave; it starts with an EOM that applies a slow amplitude modulation, required for further lock-in detection. Further, the light gets amplified by an EDFA and is launched into the sensing fibre through a circulator.

The top branch is used to generate the signal wave; first, the light passes through an electro-optic modulator (EOM) driven by an high-frequency (≈10.86 GHz) signal, generating two side-bands equally separated from the carrier frequency. The two side-bands pass through a polarisation switch, required to mitigate the polarisation dependence of the Brillouin interaction [51]. Further, a delay fibre is used to position a high-order correlation peak inside the sensing fibre (as it was described in section 2.1.1). Finally, the side-bands are amplified in an erbium-doped fibre amplifier (EDFA) and launched inside the 200 m long sensing fibre through an optical isolator.

After interacting with the pump inside the sensing fibre the signal wave is filtered on a fibre Bragg grating (FBG), leaving only one of the side-bands. The selected side-band is detected by a photodetector connected to the input of a lock-in amplifier.

a

b
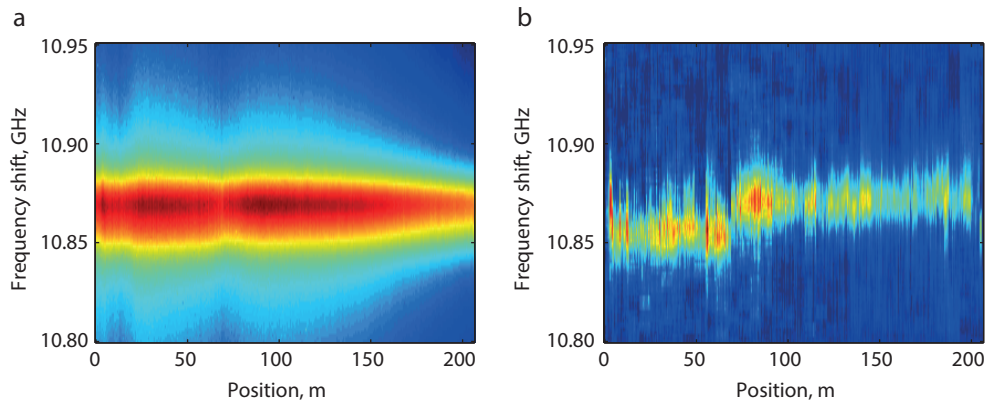
Figure 2.11: Brillouin gain spectrum measured along the 200 m fibre: a) raw measurement and b) processed data with the background removed.
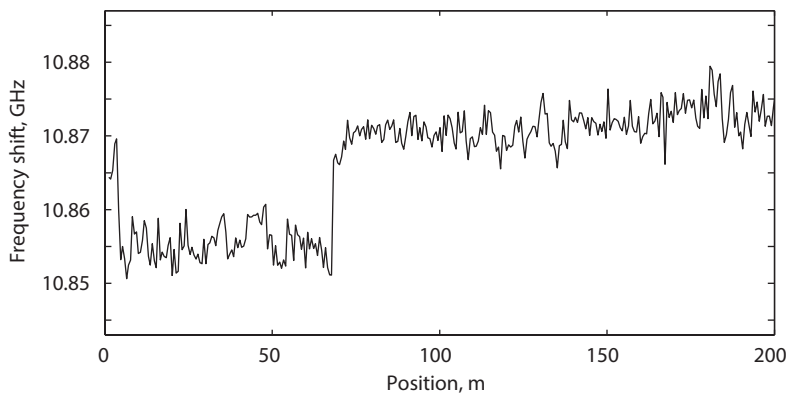
Figure 2.12: Brillouin frequency measured along a 200 m fibre

2.3.2 Measurement

By tuning the clock (and, therefore, the bit duration) of the PRBS generator, 300 positions were addressed along the sensing fibre; for each, the Brillouin gain spectrum (BGS) was measured. The result of this measurements can be seen on figure 2.11a. Due to the presence of random-gratings, to the phase shift not being perfectly equal to π, and to other spurious effects, the measurement contains a strong background signal and no details can be discerned. However, the shape of this background is given by the noise integrated over the whole fibre length and therefore it is the same for all the measurements. This way, the measurements during which the correlation peak is positioned outside of the sensing
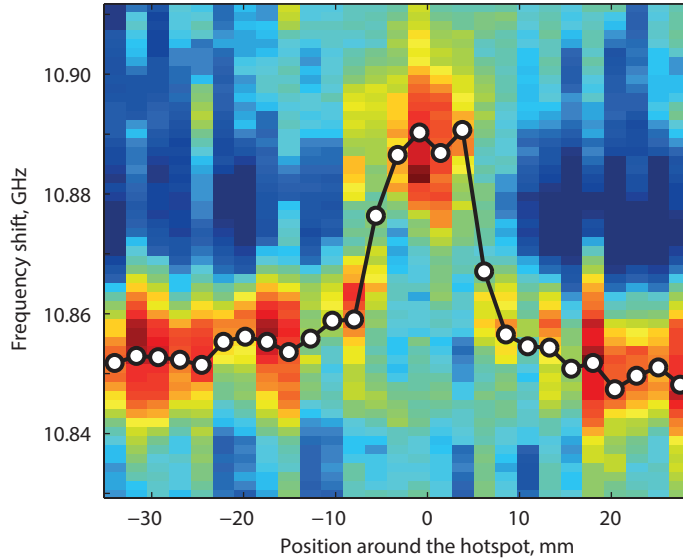
Figure 2.13: Brillouin gain spectrum measurement for a 10 mm long hotspot positioned at the end of a 200 m long fibre and the extracted Brillouin frequency shift (white dots)

fibre can be used as a reference to normalise other measurements, leaving only the gain at a given point. The results of this normalisation are shown on figure 2.11b. After the normalisation the Brillouin frequency shift was determined at each position using a standard fitting algorithm with the results shown on figure 2.12. It can be seen that the fibre consists of two sections with Brillouin frequencies of 10.872 GHz and 10.855 GHz.

2.3.3   Spatial resolution

The spatial resolution that would normally be expected for the bit duration of 90 ps is equal to 9 mm – the FWHM of a triangular correlation peak. However, as it was shown in section 2.2.3 not only the shape of the correlation peak deviates significantly for a perfect triangle, but also the spatial resolution of the system depends on the sampling interval. In order to verify the theoretical model, a 10 mm long hotspot was placed at the end of the sensing fibre (where the SNR reaches the minimum value) and the BGS was measured for the positions around it. Figure 2.13 shows that the hotspot is clearly resolved with observable shift of the Brillouin frequency from 10.852 GHz to 10.888 GHz, which corresponds to a temperature change of 33 °C. The detection of a 1 cm hotspot at a 200 m distance means that the system is capable of resolving more than 20 000 separate points.

The gain along a 10 mm long hotspot was predicted using the theoretical model for the
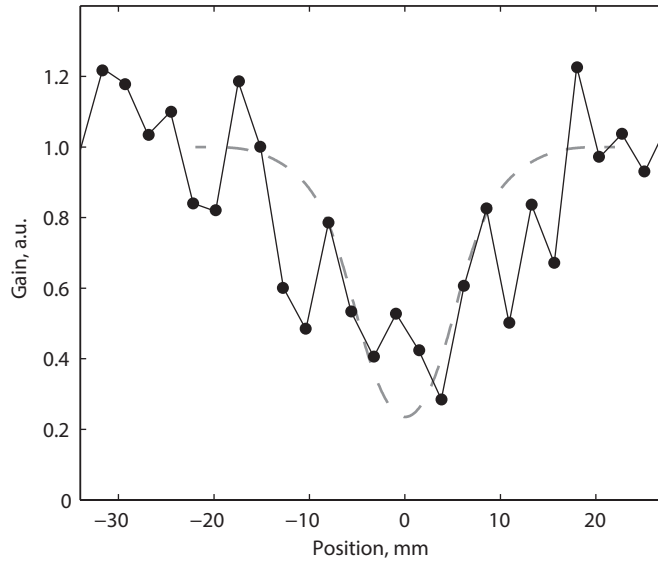
Figure 2.14: Measured (solid line) and theoretically predicted (dashed line) Brillouin gain along the hotspot for the Brillouin frequency of the unheated fibre (10.852 GHz).

spatial resolution presented in section 2.2. The results of this modelling are shown on figure 2.14 (dashed line) along with the actually measured gain (solid line) at the frequency shift of 10.852 GHz which corresponds to the Brillouin frequency shift of the unheated section of the fibre. It can be seen that the theoretically predicted drop of the Brilloiun gain is the same as measured (within the noise range of the system). However, the measured "dip" in the gain is twice broader than the predicted one (26 mm versus 12 mm). This can be explained by the transfer of the heat along the fibre which can be seen on figure 2.13 – the transition from the hotspot's Brillouin frequency to the frequency of unheated fibre is not instantaneous and follows the exponentially decaying behaviour. This heat transfer effectively increases the size of the hotspot, making impossible the direct application of the theoretical model.

2.3.4 Spectral filtering of phase-modulated signal

A set of problems that limit the performance of the system comes from the spectral broadening caused by the high-frequency phase modulation. In the experiment the PRBS bit rate was higher than the Brillouin frequency shift (11 GHz vs 10.86 GHz) meaning that the Rayleigh scattering from the pump wave strongly overlaps with the signal wave (see simulated spectra on figure 2.15), making it impossible to separate the two without intro-
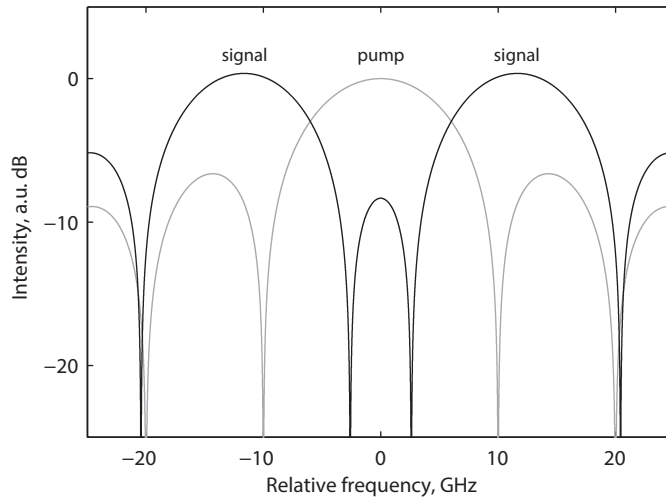
Figure 2.15: Overlapping spectra of phase-modulated pump (grey) and signal (black)

ducing any distortion. Moreover, in order to select a single signal side-band (and filter out the Rayleigh scattering from the pump) an FBG has to be used. However, an FBG is a highly dispersive element that can significantly change the phase distribution within the light spectrum. For the phase-modulated light it leads to a phase-to-intensity conversion.

Figure 2.16 shows the measurement of the dispersion-induced phase-to-intensity conversion for the signal reflected on the FBG used in the experiment. It can be seen that the amplitude of the oscillations exceeds 5 % of the average intensity while the thermal noise of the photodetector is one order of magnitude lower. Moreover, these oscillations are periodic with the period given by the period of the PRBS. This can potentially lead to a stroboscopic effect during the lock-in detection.

2.4 Discussion

Phase-correlation technique showed a capability of resolving more than 20 000 separate points. A further improvement is limited by the noise and the background signal accumulated over the whole fibre length. For the sensing length of 200 m this background accounts for 99 % of the whole response. To some extent this problem can be solved by replacing the PRBS with the Golomb code which was shown to suppress the acoustic wave generation outside of correlation peaks [52, 53]. But for a significant improvement the noise of the system has to be made independent from the measurement distance.
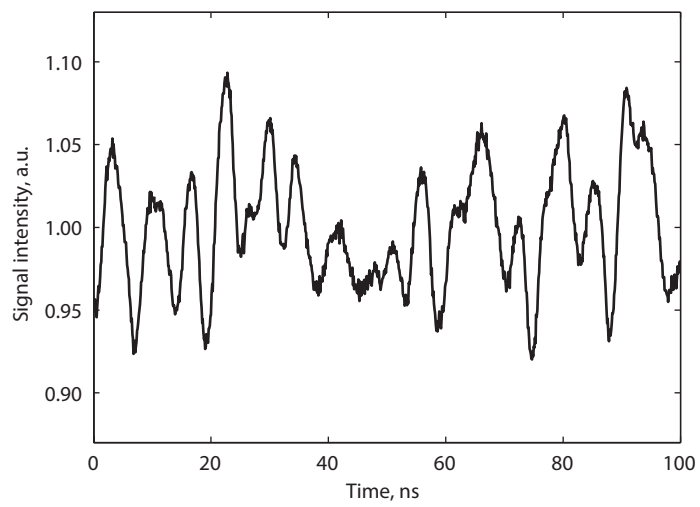
Figure 2.16: Effect of phase to intensity conversion after filtering the signal wave on a FBG

Chapter 3

Time-gated phase-correlation technique

The phase-correlation technique using continuous waves works well over short distances; but as the fibre length increases, the noise from the randomly generated gratings and modulation imperfections increases as well. As it was observed, the randomly-generated weak gratings and the imperfections in the phase modulation are capable of producing a strong background signal. In fact, in the experiment with a 200 m long sensing fibre, shown in the previous chapter, only 1 % of the detected signal corresponds to the useful gain. Even though the strong background signal can be subtracted from all the measurements, it's presence can significantly reduce the SNR of the measurement. This effect scales linearly with the fibre length and effectively limits the system to a maximum of 100 000 points [4], e.g. 1 km sensing range with 10 mm spatial resolution. Additionally, only one correlation peak is allowed within the fibre leading to a single point being measured at a time. Both of these limitations can be overcome by gating the continuous pump wave intensity with an pulse and detecting the signal wave in time domain.

3.1 Time gating

A simple explanation of this technique is shown on figure 3.1. A phase modulated pump pulse and a continuous signal wave counterpropagate inside the fibre. Since the PRBS is periodic, the phase pattern in the pump pulse is present multiple times in the signal wave, leading to multiple correlation peaks being positioned inside the fibre (figure 3.1ab). The pump-signal interaction is limited to the position of the pump pulse; when the pump pulse overlaps with the position of a correlation peak, the acoustic wave starts to grow and the signal wave gets amplified. As in the case of the continuous pump, randomly-generated weak gratings appear outside of the correlation peaks; but the noise accumu-
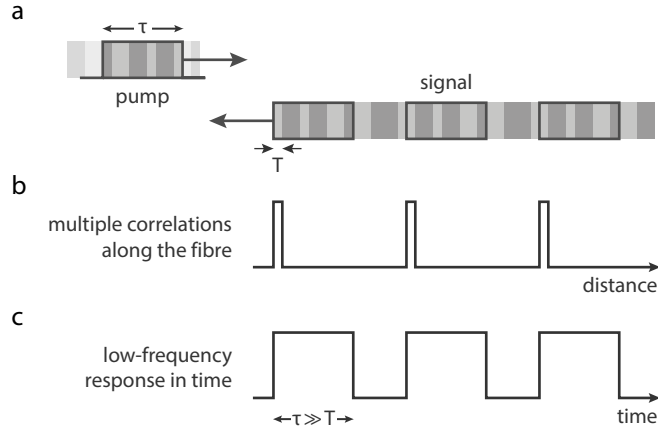
Figure 3.1: Combining phase modulation with time-gating of the pump wave: a) phase-modulated pulsed pump and continuous signal; b) multiple correlation peaks generated along the fibre; c) Time-domain response from each correlation peak.

lated from them is limited by the pump pulse duration and, therefore, is independent of the sensing fibre length. For a pump pulse shorter than the PRBS period, the responses of the multiple correlation peaks along the fibre can be detected simultaneously within a single temporal trace (figure 3.1c).

In purely time-domain high resolution sensors (DPP, etc.) the detection bandwidth is given by the spatial resolution. For example, to achieve 1 cm spatial resolution a bandwidth of 10 GHz is needed. At the same time, for the time-gated phase-correlation sensor the bandwidth is given by the duration of the pump pulse that can be on the scale of tens of nanoseconds. Therefore, a bandwidth below 100 MHz can be used, significantly reducing the noise in the detection system.

3.1.1 Experimental setup

The experimental setup that combines phase correlation with time-domain acquisition is shown on figure 3.2. As before, the output of a distributed feedback laser diode is directed into a phase-modulator driven by a pseudo-random bit sequence applying a phase shift of either 0 or π. Two PRBS durations were used in the experiment: 32 767 bits ($2^{15} - 1$) and 1023 bits ($2^{10} - 1$) which will be further referred to as *long* and *short* respectively. A bit duration of 140 ps was used, corresponding to a 14 mm FWHM of the correlation peak.

After the phase modulation the light is split by a coupler. The lower branch is used to create the pump pulses; first, the light passes through an electro-optical modulator and is modulated by a microwave signal, generating two spectral side-bands. One of the side-
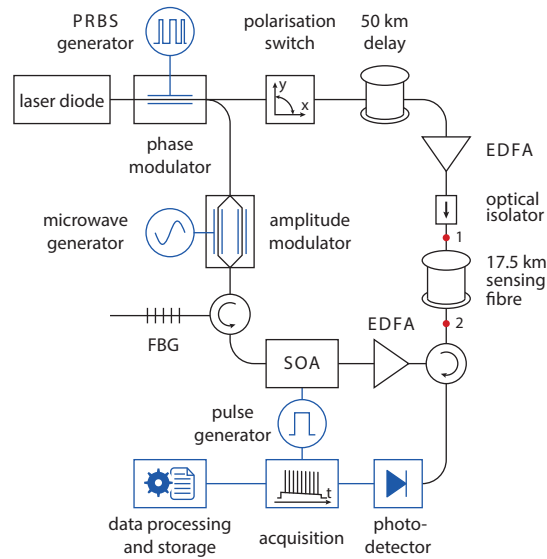
Figure 3.2: Experimental setup. EDFA: erbium-doped fibre amplifier; FBG: fibre Bragg grating; PRBS: pseudo-random binary sequence; SOA: semiconductor optical amplifier.

bands is selected on a fibre Bragg grating connected via an optical circulator. After that, the pulses are generated in a semiconductor optical amplifier that ensures the extinction ratio of more than 50 dB. An erbium-doped fibre amplifier (EDFA) is used to boost the pulse amplitude to achieve the best sensor response while avoiding the nonlinear effects.

The top branch on figure 3.2 is used to create the signal wave. The phase-modulated signal wave passes through a polarisation switch used, as before, to address both of the polarisation states to mitigate the polarisation dependence of the Brillouin interaction. A 50 km-long delay fibre is used to allocate the higher order correlation peaks inside the sensing fibre. Further, the signal is amplified by an EDFA to compensate for the losses inside the delay fibre and is launched into the sensing fibre.

The pump and the signal are counterpropagating in a 17.5 km-long sensing fibre (a standard single-mode fibre); after they interact the signal is sent into the detection part of the setup. At the detection the signal is directed onto a 125 MHz photodetector followed by a 15 MHz low-pass filter to reduce the electrical noise. The detected time trace is immediately processed, saving the data corresponding to the gain on the correlation peaks and discarding the rest.

In order to minimise the impact of the phase-to-intensity conversion noise mentioned in section 2.3.4, the side-band generation and the spectral filtering were done in the pump branch. This change has two effects: the noise is naturally integrated within
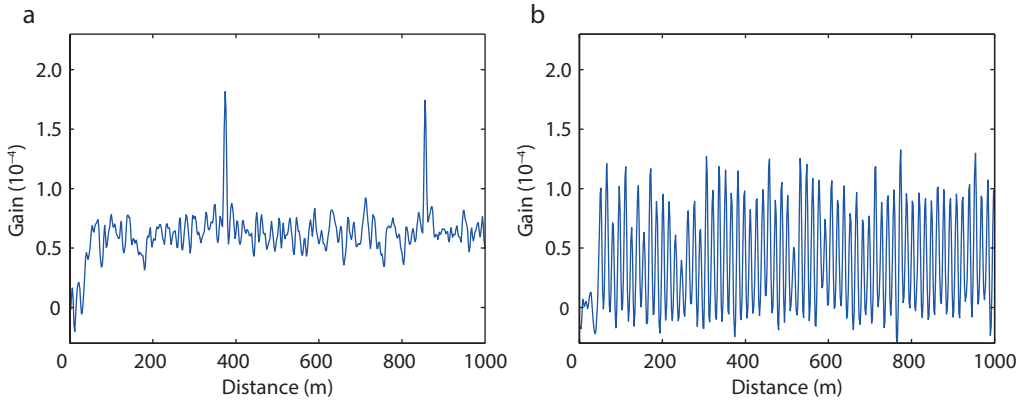
Figure 3.3: Gain along the fibre for a) long and b) short PRBS

the pump pulse; and, more importantly, only the low-frequency noise is transferred to the signal wave [54, 55]. This change reduced the measurement time by 10 times due to a smaller number of averages required in the detection system. The only effect that this new implementation has is related to the Rayleigh scattering generated by the pump that reaches the photo-detector. Although the relative contribution of the Rayleigh backscattered signal can be reduced in relation to the correlation peaks response by optimising the probe power, there will be always a small Rayleigh component present in the measured traces. However, the spectral response of the Rayleigh scattering is naturally flat; therefore, this component has no real impact on the spectral measurements of the Brillouin gain, and can be easily eliminated by a simple data processing.

3.1.2 Time-domain traces

Figure 3.3 shows measured Brillouin gain acquired at the peak Brillouin gain frequency along the sensing fibre, for long (figure 3.3a) and short PRBS (figure 3.3b), using a pump pulse of 70 ns. Note that the correlation peak amplitudes vary slightly along the fibre because of the variations of the Brillouin frequency. For the long PRBS, correlation peaks are considerably separated (by 460 m) and a relatively strong background signal is observed. This background signal is caused by the spectral properties of the phase-modulated light and will be explained later. For the short PRBS, the separation between correlation peaks becomes small (14 m), and the background signal almost disappears.

This background signal originates from the non-zero linewidth of the Brillouin gain spectrum. The spectra of the two phase-modulated waves consist of multiple lines, separated spectrally by the PRBS repetition rate. Figure 3.4 shows the spectrum measured for the light modulated with a 127 bit long PRBS. A zoom-in shown on figure 3.4 shows
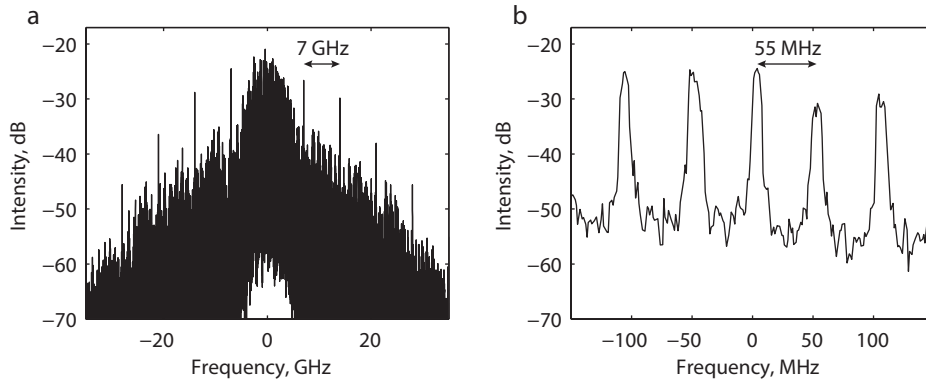
Figure 3.4: Spectrum of light modulated with the PRBS of 127 bits and bit rate of 7 GHz (line separation 55 MHz)
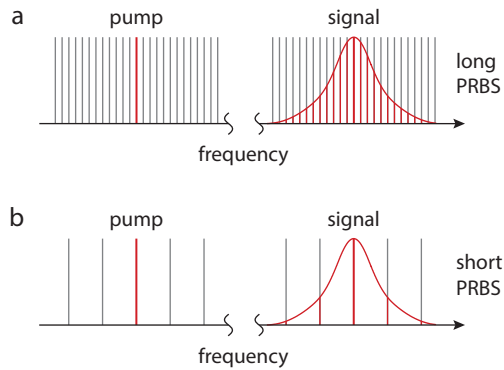
Figure 3.5: Cross-interaction between multiple spectral lines of phase-modulated pump and signal waves for a) long and b) short PRBS (the line separation is not to scale)

spectral lines with separation of $7\,\mathrm{GHz}/127\ =\ 55\,\mathrm{MHz}$. For the long and short PRBS used in the experiment the line separation is equal to 215 kHz and 6.8 MHz, respectively, which is beyond the resolution of the available optical spectrum analyser.

Due to a small line separation and the 30 MHz width of the Brillouin gain, each spectral line in the pump wave can interact with more than one hundred lines in the probe for the long PRBS case, whilst for the short PRBS, this number goes down to only five (see figure 3.5). This explains the strong difference in the background level for two time traces in figure 3.3. Te origin of this behaviour is the presence of slowly varying components in the modulation signal – slow enough for the acoustic wave to follow them.

3.2 Optimal pump pulse duration

One of the parameters of the system that needs to be optimised to achieve the best performance is the duration of the pump pulse. The pulse duration has actually multiple distinct effects on the measured traces. For pulses shorter than ~30 ns, the acoustic wave at each correlation peak does not have enough time to reach the steady state amplitude, leading to a poor sensor response. In addition, short pulses require large detection bandwidth, which increases the noise of the measurements. On the other hand, longer pulses introduce more noise accumulated from randomly-generated gratings, weak permanent gratings coming from the non-instantaneous phase change, and other spurious effects, thus also leading to a decrease in SNR. The pump pulse duration also defines the minimum separation between consecutive correlation peaks so that their responses do not overlap. An optimum pulse width has to be found to minimise the measurement time.

3.2.1 Pump pulse duration and the system's response

In order to find the time evolution of the acoustic wave amplitude in the correlation peak, equation (1.28) for the acoustic wave amplitude has to be solved:

$$\frac{\partial Q(z,t)}{\partial t} + \Gamma_A Q(z,t) = j g_1 A_p(z,t) A_s^*(z,t).$$ (3.1)

At the centre of the correlation peak the phases of the pump and the signal are perfectly correlated, meaning that the term $A_p(z=0,t)A_s^*(z=0,t)$ does not change in time[1]. It means that equation (3.1) can be simplified and solved to find the evolution of the acoustic wave in time (setting the z-axis origin in the centre of the correlation peak and assuming that the interaction between the optical waves starts at $t=0$):

$$Q(z=0,t) = j g_1 A_p A_s^* \int_0^t \exp\left(-(t-t')\Gamma_A)\right) \mathrm{d}t'$$

$$= \frac{j g_1 A_p A_s^*}{\Gamma_A} \left(1 - \exp\left(-t\Gamma_A\right)\right).$$ (3.2)

This equation gives the temporal response of the acoustic wave at the maximum amplitude of the correlation peak, while at other positions the interaction is weaker accordingly to the shape of the correlation peak as it was discussed in section 2.2.1.

The evolution of the amplitude of the signal wave is given by equation (1.38):

$$\frac{\partial A_s(z,t)}{\partial z} - \frac{1}{v_g}\frac{\partial A_s(z,t)}{\partial t} = -\frac{1}{2} j g_2 A_p(z,t) Q^*(z,t),$$ (3.3)

---

[1]Since the gain is very low we can apply the small gain approximation and consider amplitudes of the pump and the signal to be constant when calculating the amplitude of the acoustic wave

where v_g is the group velocity and g_2 is elasto-optic coupling coefficient. Let's define the effective size d_eff of the correlation peak through the asymptotic shape of the correlation peak:

$$d_\mathrm{eff} = \frac{1}{Q(z = 0, t = +\infty)} \int\limits_{-\infty}^{+\infty} Q(z, t = +\infty)\, \mathrm{d}z \,, \tag{3.4}$$

which allows us to replace an arbitrarily shaped correlation peak with a rectangular one with the width of d_eff and amplitude $Q(z = 0, t)$ from equation (3.2). Since the bit duration is much shorter than the acoustic phonon lifetime, we can consider the hotspot as a point source of gain, solving equation (3.3) at each point of time in a quasi-steady-state condition:

$$\frac{\partial A_\mathrm{s}(z, t)}{\partial z} = -\frac{1}{2} j g_2 A_\mathrm{p}(z, t) Q^*(z, t) \,, \tag{3.5}$$

$$\Delta A_\mathrm{s} = -\frac{1}{2} j g_2 A_\mathrm{p} Q(z = 0, t) d_\mathrm{eff} \,, \tag{3.6}$$

$$\Delta A_\mathrm{s} = \frac{g_1 g_2 |A_\mathrm{p}|^2 A_\mathrm{s}}{2\Gamma_\mathrm{A}} \left(1 - \exp\left(-\Gamma_\mathrm{A} t\right)\right) \,. \tag{3.7}$$

Here ΔA_s represents the sensor response at the correlation peak. Since the measurement is performed by a photodetector, the following signal intensity is detected:

$$I_\mathrm{s} = |A_\mathrm{s} + \Delta A_\mathrm{s}|^2 = A_\mathrm{s}^2 + 2A_\mathrm{s}\Delta A_\mathrm{s} + \Delta A_\mathrm{s}^2 \,. \tag{3.8}$$

The third term is actually very small and can be safely neglected, giving the final equation for the useful signal of the system:

$$\begin{aligned}
\Delta I_\mathrm{s}(t) &= \frac{g_1 g_2 I_\mathrm{s} I_\mathrm{p} d_\mathrm{eff}}{\Gamma_\mathrm{A}} \left(1 - \exp\left(-\Gamma_\mathrm{A} t\right)\right) \\
&= g_\mathrm{cp} I_\mathrm{s} \left(1 - \exp\left(-\Gamma_\mathrm{A} t\right)\right) \,,
\end{aligned} \tag{3.9}$$

where I_s, I_p are intensities of the signal and the pump wave and $g_\mathrm{cp} = g_1 g_2 I_\mathrm{p} d_\mathrm{eff}/\Gamma_\mathrm{A}$ is the asymptotic gain on the correlation peak. This signal grows while the pump pulse overlaps with the correlation peak and sharply goes to zero after it has passed.

For the measurement bandwidth adjusted to the inverted pump pulse width t_PW, the measured signal can be considered to be given by the time average of equation (3.9), as:

$$\begin{aligned}
\Delta I_\mathrm{s,msr} &= \frac{g_\mathrm{cp} I_\mathrm{s}}{t_\mathrm{PW}} \int\limits_0^{t_\mathrm{PW}} \left(1 - \exp\left(-t\Gamma_\mathrm{A}\right)\right) \mathrm{d}t \\
&= g_\mathrm{cp} I_\mathrm{s} \left(1 - \frac{1 - \exp\left(-\Gamma_\mathrm{A} t_\mathrm{PW}\right)}{\Gamma_\mathrm{A} t_\mathrm{PW}}\right) \,.
\end{aligned} \tag{3.10}$$
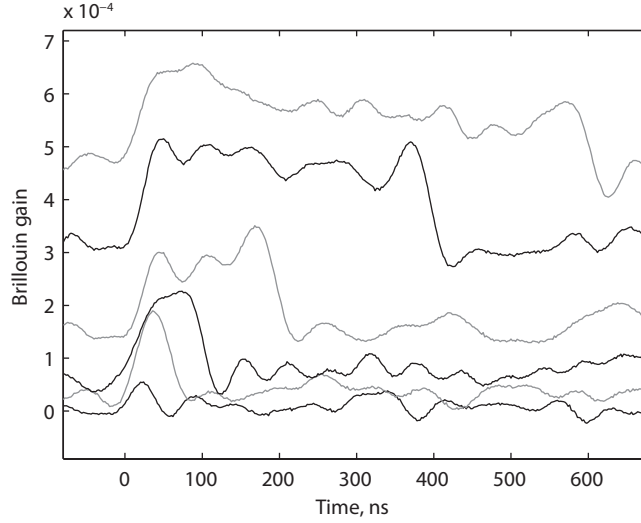
Figure 3.6: Time-domain response for pump pulse durations of 30, 60, 100, 200, 400, and 600 ns.

Knowing the gain g_{cp} provided by the correlation peak and the standard deviation σ_N of the measurement noise, equation (3.10) can be used to predict the signal-to-noise ratio (SNR) of the system, as:

$$ SNR = \frac{\Delta I_{\mathrm{s,msr}}}{\sigma_N} \, . \tag{3.11} $$

3.2.2 Experimental verification

In order to determine the optimal pump pulse duration, the signal-to-noise ratio of the measurements and the acquisition time have been evaluated for the pump pulse widths ranging from 30 ns up to 200 ns, for the long PRBS. Then the procedure has been repeated for the short PRBS, but in this case a maximum pulse duration of 130 ns has been used to avoid significant overlapping of the responses of consecutive correlation peaks. In this experiment the electrical low-pass filter in the receiver has been removed to avoid signal distortion for short pulse durations. The measured noise for all the traces was found to be given by the thermal noise of the photodetector, meaning that the noise from the random and weak gratings is negligible for these pump pulse durations. The measured time response of one correlation peak is shown on figure 3.6. It can be seen that initially the time response grows in amplitude, but eventually it reaches the steady state and after that simply gets longer. Also note the background signal that was mentioned in section 3.1.2, it can be seen that it grows rapidly and distorts the measurement.
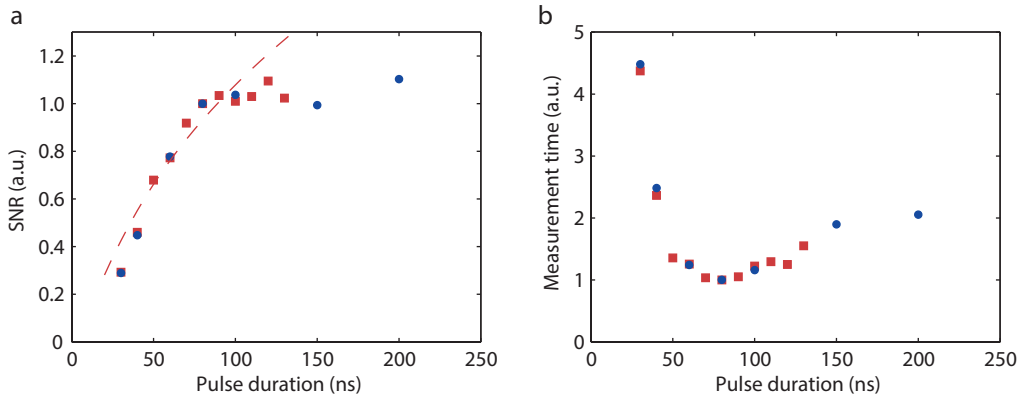
Figure 3.7: a) Signal-to-noise ratio and b) measurement time dependence on the pump pulse duration for short (squares) and long (circles) PRBS; dashed line shows theoretically predicted SNR.

Time traces were filtered digitally to match the bandwidth to the inverse of the pump pulse duration and the SNR was measured for each trace. Figure 3.7a shows results of this measurement for both analysed cases as a function of the pulse duration; the theoretical SNR predicted using the measured noise and equations (3.10) and (3.11) is shown as well. Measurements are normalised to the SNR obtained with the pulse duration of 70 ns, which was later used in the experiment. It should be mentioned, though, that the absolute SNR for the long PRBS is slightly lower due to the higher background component that introduces some noise into the signal. As it was shown before, the SNR grows with the pulse duration since *i)* the acoustic wave has more time to grow and, *ii)* longer pulses require smaller detection bandwidth. The theoretical SNR shows a good agreement with the measurements for the pump pulse duration below 90 ns (see figure 3.7a). After 90 ns the measured SNR reaches a plateau, for the short PRBS it is caused by the overlap between responses of two consecutive peaks, while for the long PRBS this is caused by distortions originating from the increased background signal.

The SNR and the pump pulse duration define the measurement time since they give the required number of averages and the number of positions scanned, respectively. Figure 3.7b how the expected measurement time depends on the pump pulse duration. Amplitudes in both curves have been normalised to the case of 70 ns pulse duration for a better comparison with our final experiment. The actual measurement time with the short PRBS is 32 times smaller than the one for long PRBS due to the larger number of simultaneously addressed correlation peaks. Figure 3.7b shows that the minimum measurement time is obtained for pulses ranging between 60 ns and 90 ns, which also corresponds to the range showing the maximum SNR in figure 3.7a.
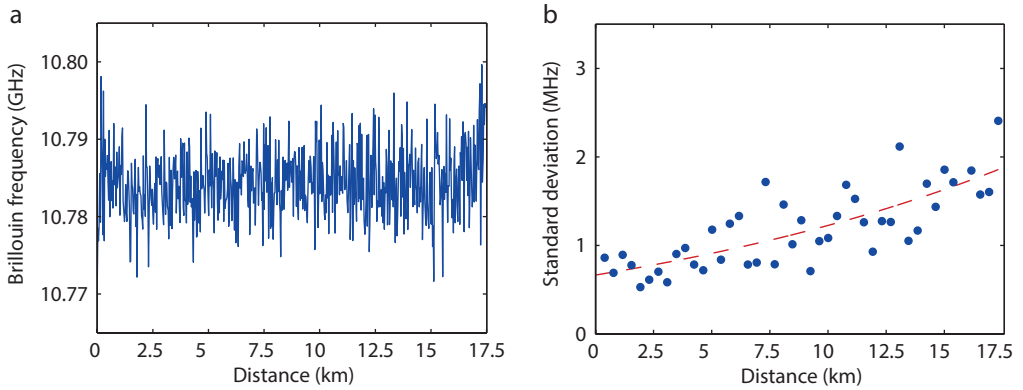
Figure 3.8: a) Measured Brillouin frequency distribution along a 17.5 km long fibre and b) respective frequency uncertainty

3.3   Experiment

3.3.1   Measurement along a 17.5 km long fibre

Based on the previous pulse optimisation of the pump pulse duration, the pulse width of 70 ns and the short PRBS of $2^{10} - 1$ bits (1023 bits) have been used in our experiment to maximise the number of correlation peaks in the temporal traces and minimise the measurement time. Moreover, pulses of 70 ns ensure the absence of temporal overlapping between responses of consecutive correlation peaks. At the same time, the reached SNR for this pulse duration corresponds to about 90 % of the maximum SNR (reached at 90 ns), representing a negligible penalty (less than 0.5 dB) with respect to the optimal SNR level.

A PRBS duration of 1023 bits with bit duration of 140 ps gives a correlation peak separation of 14.3 m, allowing for a simultaneous measurement of about 1200 points along the 17.5 km-long fibre in a single temporal trace. The Brillouin gain has been measured using 512 times averaged temporal traces, while the Brillouin frequency has been retrieved by fitting the spectrum at each position with a quadratic curve [56]. Results of this fitting are shown in figure 3.8a. It can be seen that the Brillouin frequency shift is successfully measured along the whole fibre. Note that the strong variation of measured Brillouin frequency shift is beyond system's uncertainty (as it will be shown in the next paragraph) and is due to the actual variation of the Brillouin frequency shift along the fibre.

In order to estimate the uncertainty of the measurement, the standard deviation of the retrieved Brillouin frequency has been evaluated along the whole fibre by repeating the measurements multiple times. Figure 3.8b depicts the uncertainty of the estimated Brillouin frequency as a function of distance, showing an expected exponential growth along the fibre, which reaches the average value of 1.8 MHz at the farthest fibre end.

44
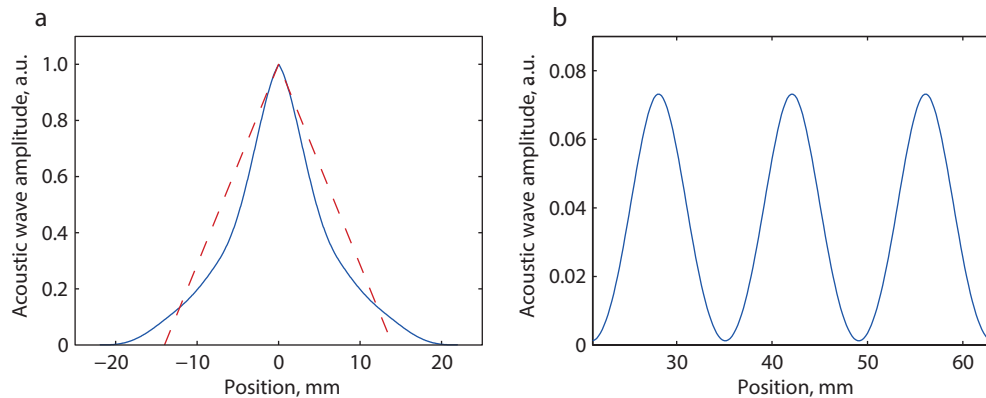
Figure 3.9: a) The shape of the correlation peak for 140 ps bit duration; b) Weak gratings caused by imperfect phase modulation

3.3.2 Spatial resolution

The modelling of the correlation peak shape and the spatial resolution presented in section 2.2 was repeated for the bit duration of 140 ps. The predicted shape of the correlation peak and the weak gratings generated outside of it are shown on figure 3.9. Comparing these results with the ones obtained for the bit duration of 90 ps (figure 2.5) we can see that the correlation peak shape is closer to the perfect case and the weak gratings' amplitude is reduced significantly (reflectivity of 3.5 % of the correlation peak's vs. 15 %).

The resulting relation between the sampling interval and the spatial resolution is shown on figure 3.10. It can be seen that the best spatial resolution reaches 8.2 mm for the perfect rectangular modulation and 7.7 mm for the noninstantaneous phase transition.[2] Also, generally, the curve for the imperfect modulation is closer to the one corresponding for the perfectly rectangular modulation than it was for the bit duration of 90 ps (figure 2.9). It can be easily explained – for a fixed transition time a lower-frequency phase modulation is closer to a perfectly rectangular one.

In order to check the spatial resolution of the implemented system a hotspot of 14 mm was placed at the farthest end of the sensing fibre (i.e. at 17.5 km distance). The Brillouin gain spectrum (BGS) was measured around the hotspot position and the Brillouin frequency was extracted for each fibre position, as shown in figure 3.11. The sampling interval within the hotspot has been set to 2.8 mm, which, according to the results presented on figure 3.10 gives an expected spatial resolution of 8 mm. The hotspot is clearly resolved with an observable heat transfer along the fibre. The measured Brillouin frequency profile

---

[2]Once again, the spatial resolution is better for the imperfect modulation, but in this case it is even more pronounced.
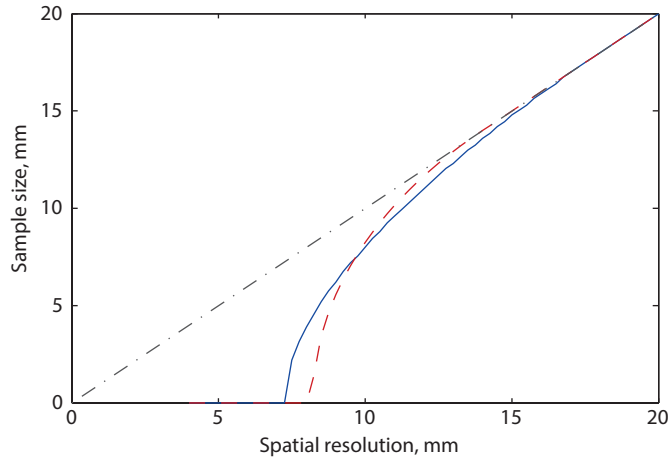
Figure 3.10: Minimum sampling interval required to obtain a given spatial resolution for the perfect square modulation (dashed red line) and the non-instantaneous phase modulation (solid blue line). The dash-dotted black line represents the asymptotic case of sampling interval being equal to the spatial resolution.

suggests that the spatial resolution is indeed better than 14 mm; however, it is difficult to make a definitive claim in this case due to the observed longitudinal heat transfer along the fibre.

For the verification of the spatial resolution, a sharp transition in the Brillouin frequency would be more appropriate. The strain-induced change in the Brillouin frequency is a promising source of such transition; for example, inside a standard optical connector. To fabricate fibre connectors (such as standard FC-PC or FC-APC connectors), the optical fibre is glued inside a ceramic ferrule which applies a strain to the fibre, resulting in a sharp shift of the Brillouin frequency. The Brillouin gain spectrum was measured inside the APC connectors at both ends of the sensing fibre (marked with red dots on figure 3.2).

The first measurement was carried out for connector 1, linking the farthest end of the sensing fibre and the attached isolator. At this point the system shows the lowest SNR, resulting in the most challenging condition to verify the high spatial resolution of the system. Figure 3.12a shows the measured Brillouin gain spectrum and the retrieved Brillouin frequency (white circles) at each fibre position. It can be seen that the 16 mm-long section under strain is clearly resolved with sharp transitions at both sides, demonstrating that the system is capable of resolving even shorter perturbations in Brillouin frequency shift. Figure 3.12b shows the gain response of the sensor at 10.86 GHz – the average Brillouin frequency shift outside the connectors. The drop of the Brillouin gain, as a consequence of the strain inside the connectors, is clearly observed. In addition, the sensor response

46
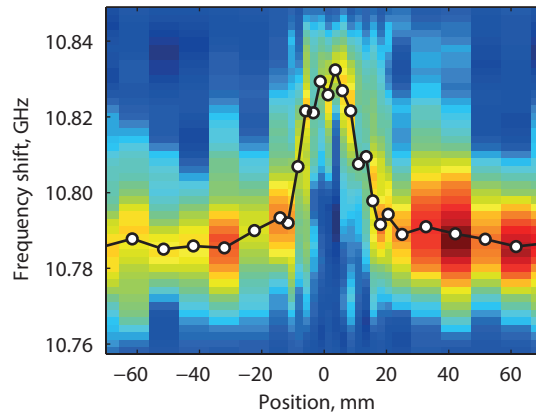
Figure 3.11: Brillouin gain spectrum measured in the vicinity of a 14 mm long hotspot positioned at the end of the 17.5 km long fibre. White circles show the extracted Brillouin frequency shift.

has been theoretically estimated based on the model presented in section 2.2.2. This response is also illustrated in the figure (red dashed line), showing a good agreement with the experimental trace and validating the theoretical model.

The measurement was repeated for connector 2 linking the beginning of the sensing fibre and the circulator. At this position the SNR of the measurements shows the maximum value, so that it was possible to perform the measurement with the shortest available bit duration of 80 ps. The modelling was repeated, predicting a spatial resolution of 4.5 mm for the sampling interval of 2 mm. Figure 3.12c shows the measured Brillouin spectrum and the retrieved BFS, while figure 3.12d compares the experimental and theoretically-predicted gain response versus fibre location at the average peak gain frequency of 10.87 GHz. Once again, a good agreement is observed.

The agreement between the theory and the experiment in both measurements validates the theoretical model and the approach presented in section 2.2 for the spatial resolution of a phase-correlation Brillouin sensor. It means that the spatial resolution obtained with a sampling interval of 4.7 mm and bit duration of 140 ps is equal to 8.3 mm, as shown on figure 3.10. Thus, the system is capable of resolving 2 100 000 points along the whole sensing fibre.

3.3.3 Brillouin scattering in tapered fibres

The high spatial resolution of phase-correlation Brillouin sensors can be used to measure Brillouin gain in small devices, e.g. tapered fibres. A tapered fibre is produced by gently
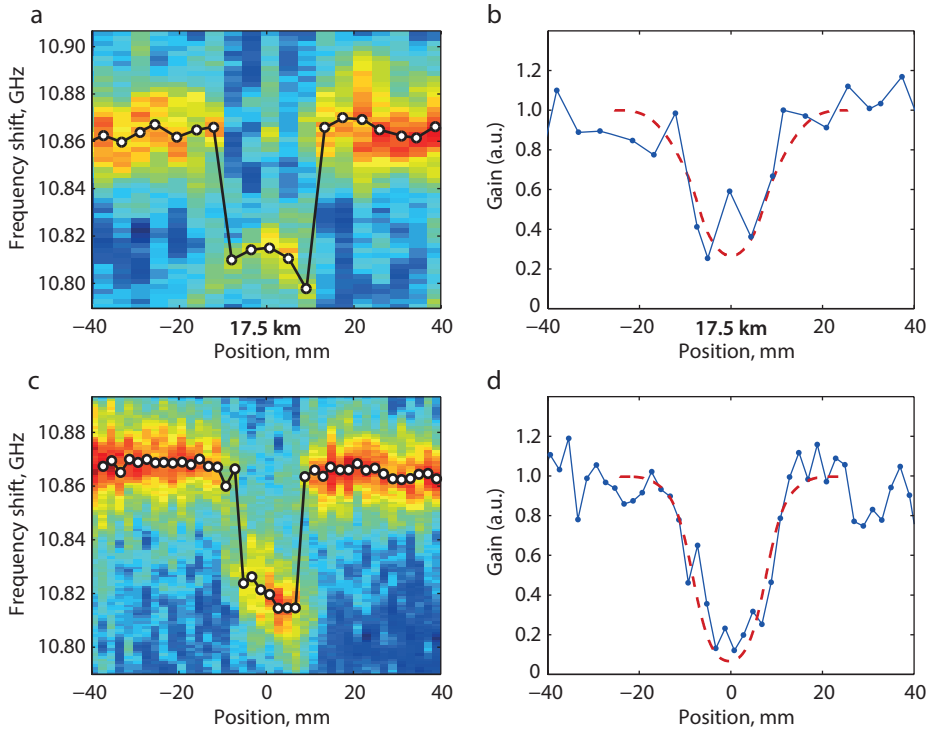
Figure 3.12: (a) Brillouin gain spectrum and extracted Brillouin frequency (white dots) inside the connector 1 at the farthest end of the 17.5 km-long fibre using 140 ps bit duration; (b) gain for the average Brillouin frequency of the fibre: measured (blue line) and theoretically predicted (dashed red line); (c) and (d) the same information for the measurement of connector 2 at the beginning of the fibre with the bit duration of 80 ps.

stretching an optical fibre while it is heated, e.g. over a flame, such that the glass becomes soft. This procedure makes the fibre thinner over some length; normally, on a scale of several millimetres or centimetres. Tapered fibres have a large number of optical properties that make them attractive for both fundamental physics and photonic technologies. In addition to providing strong light confinement and enhanced nonlinear optical effects [57, 58], they also exhibit a large evanescent field, enabling applications not currently possible with conventional optical fibres.

As the diameter of a fibre changes along the tapered region, so does the acoustic mode configuration; at small diameters surface acoustic modes appear which can significantly increase Brillouin scattering efficiency. This effect was modelled [59] but not experimentally studied. We decided to apply the phase-correlation sensing technique to measure
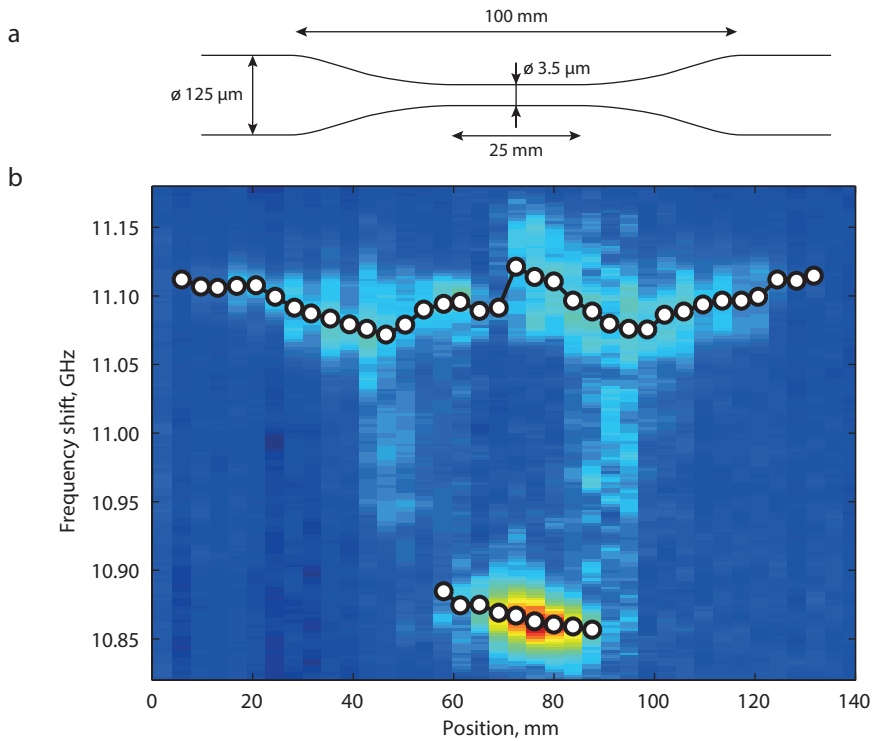
Figure 3.13: a) Silica tapered fibre structure; b) Brillouin gain measurement along the taper. White dots correspond to the fitting of Brillouin frequency shift for two modes.

Brillouin gain spectrum along two tapered fibre samples.

The first sample was manufactured from a standard single mode fibre, with the tapered region length of 25 mm and the diameter of 3.5 µm as shown on figure 3.13a. The measured Brillouin gain spectrum is shown on figure 3.13b along with the extracted Brillouin frequency shift. As the diameter of the fibre decreases Brillouin gain spectrum splits into two peaks: one close to 11.1 GHz – Brillouin frequency of untapered fibre. The other Brillouin gain peak starts 11.07 GHz and quickly shifts to 10.85 GHz as diameter of the fibre decreases. Inside the waist region Brillouin gain for the second peak is three times larger than for the first which can be attributed to a better overlap between optical waves and the acoustic wave mode responsible for this peak.

In the second experiment a chalcogenide (As_2Se_3) sample was used. This sample had a 13 cm long tapered region with a diameter of 1.65 µm. Figure 3.14 shows the measured Brillouin gain spectrum and the extracted Brillouin frequency shift, which is lower for chalcogenide fibres. No fine structure was observed in this measurement, except for a
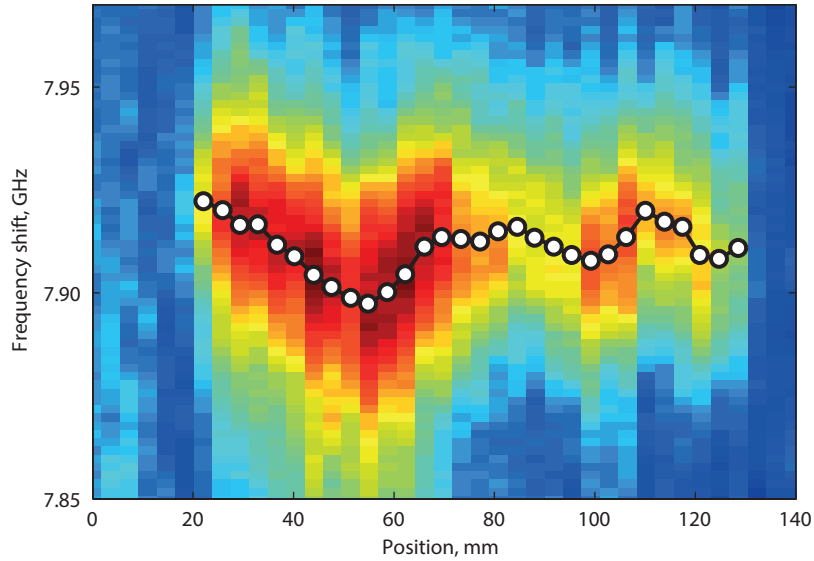
Figure 3.14: Brillouin gain measurement along the chalcogenide taper. White dots correspond to the fitting of Brillouin frequency shift.

minor variation of Brillouin frequency shift.

A more interesting picture appears when Brillouin gain spectrum is observed separately for two polarisation states of the signal wave, as seen on figure 3.15. It can be seen that for each polarisation Brillouin gain goes from the maximum value to the minimum and back again. This behaviour is caused by the birefringence that rotates polarisations of the pump and the signal making them either co-aligned (maximum gain) or orthogonal (no gain). The observed beat length of 4 cm corresponds to a birefringence of approximately 3.9×10^{-5}. It means that the tapered region may have a slightly elliptical shape that is preserved along the whole waist region.

A detailed analysis of this data is outside of the scope of this work, but it clearly shows that the phase-correlated sensing technique allows for a detailed measurement of Brillouin gain spectrum in compact devices, showing how fine structure affects Brillouin frequency shift, and revealing the birefringence.

3.4   Discussion

As it was shown in this chapter, time gating significantly improves the performance of a phase-correlated sensor, increasing the number of points by two orders of magnitude (2 000 000 versus 20 000 points). For the first time in the history of distributed Brillouin

50
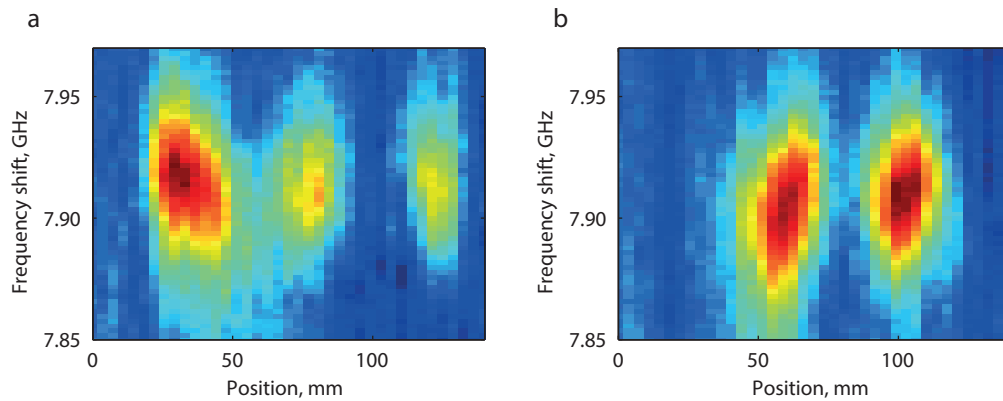
Figure 3.15: Brillouin gain measurement along the chalcogenide taper measured separately for two polarisation of signal wave. Oscillations between maxima and minima of gain are a sign of birefringence.

sensing, measurements with centimetre scale resolution are demonstrated at a distance of tens of kilometres.

The theoretical model introduced in the previous chapter is expanded to calculate the signal-to-noise ratio depending on the duration of the pump pulse. Once again, a good agreement is observed between the modelling and the experimental results, proving that the spatial resolution of the system is better than the full width at half maximum of the correlation peak.

Measurements of the Brillouin gain spectrum along tapered fibres show that the phase-correlation technique can be a powerful tool in studying such optical elements. It can show how the modal configuration (optical and acoustic) depends on the geometrical structure and reveal its irregularities.

Chapter 4

Addressing the limits

Time gating allowed increasing the number of points resolved by a phase-correlated sensor by two orders of magnitude. However, as any other technique, this one has its own limitations. Combining high spatial resolution with long measurement distance brings together limiting factors of both domains: fibre losses, nonlinear effects, long measurement time due to a point-by-point measurement. This chapter addresses the limitations and proposes solutions that can be used to minimise their effect or overcome them completely.

4.1 Power limitations

The measured Brillouin gain is proportional to the power of the pump wave, which makes raising the power the most straight-forward way of increasing the signal-to-noise ratio. However, nonlinear effects set a limit to pump power, especially for long sensing distances. For standard single mode fibres (SMF) this limit is given by the modulation instability (MI), which, for fibres longer than 15 km limits the peak power of the pump wave to some 100 mW [46]. Modulation instability occurs only in systems exhibiting anomalous dispersion, which is the case for the SMF at the commonly used wavelengths. Specifically designed dispersion-shifted fibres (DSF) exhibit normal dispersion making modulation instability impossible. Using such fibres it is possible to extend the limit for the pump power to about 400 mW [46] at which the stimulated Raman scattering starts to occur.

However, using DSF in phase-correlated setups proves to be impossible due to the spectral characteristics of the interacting waves. As it was shown in the previous chapter the spectrum of a light wave modulated with a PRBS consists of multiple equidistant lines with the separation equal to the period of the PRBS $1/N_{\mathrm{bits}}T_{\mathrm{bit}}$ (see figure 3.4). Optical waves with such spectrum are very prone to another nonlinear effect called four-wave mixing (FWM), which in this case leads to an energy transfer between the spectral compo-
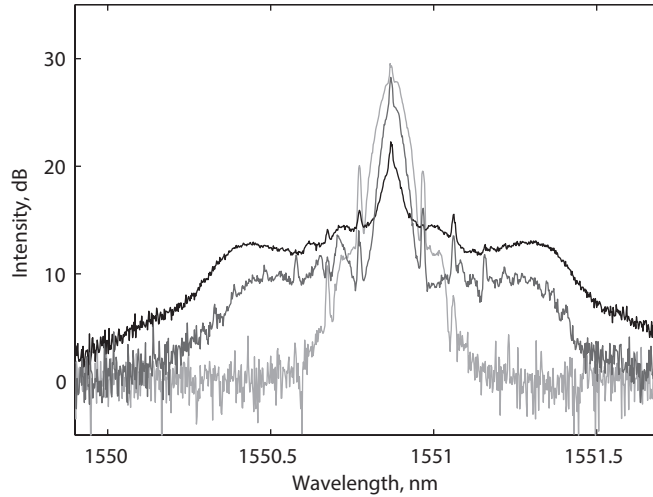
Figure 4.1: Spectral distortion of phase-modulated signal due to a combination of four-wave mixing and self-phase modulation.

nents. In DSF this effect is especially pronounced due to the zero dispersion wavelength being close to the interacting waves. It makes application of DSF in phase-correlation sensors impossible. Figure 4.1 shows how nonlinear effects distort the spectrum of phase-modulated light.

Pulse coding has been proved to be an efficient technique to overcome limitations of the pump power. In this method a single pump pulse is replaced by a set of pulses with the same peak power. Responses of each pulse sum up together creating a trace with a bigger response, which though cannot be used directly. The measurement has to be repeated with several configurations of pulses producing, after post-processing, a final measurement with an improved signal-to-noise ratio.

All the pulse-coding techniques used in classic time-domain sensors [16, 17, 19] can be directly applied to the time-gated phase-correlation technique. Moreover, London *et al.* [60] showed due to specifics of the correlation-based technique, other coding schemes can be applied.

4.2 Number of points and measurement time

The number of points that a sensor is capable of resolving is given by the quotient of the measurement distance and the spatial resolution. Thus, it can be increased by both improving the spatial resolution and extending the sensing distance. However, it can be shown that the measurement time increases highly nonlinearly for both ways.

54
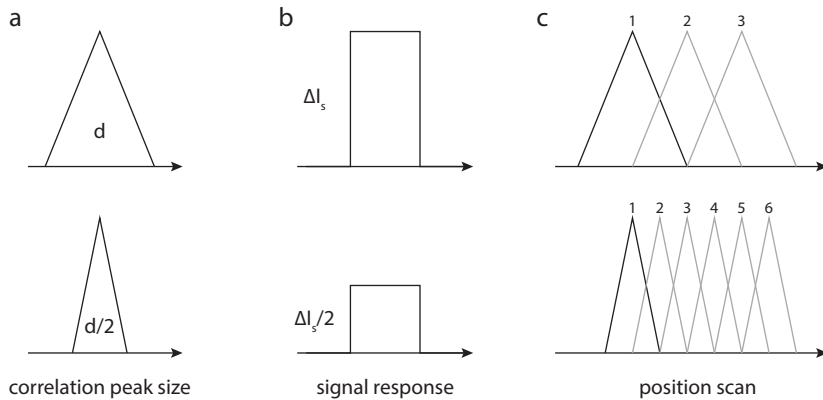
Figure 4.2: System's reaction to a twofold change in the spatial resolution: a) correlation peak size is halved; b) signal intensity change drops twice; c) number of correlation peak positions doubles.

4.2.1 Spatial resolution improvement

Let's see how the measurement time changes when the spatial resolution changes twofold, e.g. from 2 cm to 1 cm. First, as it can be seen from figure 4.2ab the size of the correlation peak decreases twice leading to a twofold drop in the measured change in the signal wave intensity (see equation (3.9)). In order to compensate the following change in the SNR, the number of averages has to be increased four times. Additionally, the number of correlation peak positions that have to be scanned to address the whole fibre increases twofold as seen on figure 4.2c, leading to an additional increase in the measurement time.

Overall it leads to a cubic dependence of the measurement time on the spatial resolution, e.g. for a given distance a sensor capable of resolving 1 000 000 points would be 1000 times slower than a sensor with just 100 000 points.

There is also a direct limitation for the spatial resolution given by the spectral shape of the phase-modulated light (already discussed in section 2.3.4). The spectral width of the modulated waves is given by the bit rate of the PRBS which defines the spatial resolution. A higher spatial resolution requires a faster phase modulation, which makes spectra of interacting waves overlap heavily, introducing a strong noise during the filtering process. It means that while achieving a higher spatial resolution is possible (e.g. using amplified stimulated emission of an EDFA as a light source [61]) it will certainly lead to a decrease in the SNR and, therefore, in measurement distance.

55
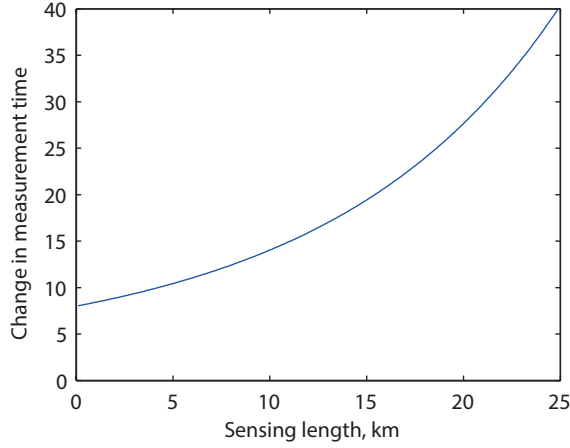
Figure 4.3: Measurement time change for a twofold increase in the sensing distance.

4.2.2 Distance improvement

Derivation of the measurement time impact to a twofold increase in the sensing distance is not as straightforward. First, the time of flight through the fibre linearly depends on its length; thus, the time needed to acquire a single time trace will grow twice. The change in the signal wave intensity will drop down for two reasons: first, the losses in the fibre scale exponentially with the distance; second, the limit for the pump power depends on the nonlinear effects which makes it inversely proportional to the effective length of the fibre $L_{\text{eff}} = (1 - \exp(-\alpha L))/\alpha$, where α is the loss coefficient with the typical value of $0.05\,\text{km}^{-1}$ in SMF for the wavelength of $1.5\,\mu\text{m}$. The required number of averages for each acquired time trace is inversely proportional to the square of the signal-to-noise ratio, that depends linearly on the pump power. Overall it gives the following dependence of the measurement time on the sensing distance:

$$t_{\text{msr}} \propto \frac{\left(1 - e^{-\alpha L}\right)^2}{e^{-2\alpha L}} L \qquad (4.1)$$

where the numerator of the fraction corresponds to the decrease in pump power due to the nonlinearity limit, the denominator corresponds to the increasing loss (a factor 2 is due to the back-and-forth propagation), and multiplier L is the linear increase of the time of flight. Figure 4.3 shows how much the measurement time increases when the sensing length is doubled, depending on the original fibre length. It can be seen that it starts with 8 – the same as for the twofold improvement of the spatial resolution – but it quickly grows up, reaching more than 25 for a 20 km long fibre.

Thus, improving the spatial resolution is always preferable to an equivalent improvement in the sensing distance. Yet, as it was mentioned before, the spatial resolution cannot be improved indefinitely due to the spectral reasons. Once the limit is reached, the only way to further increase the number of points would be extending the measurement distance.

One way to do that is to directly compensate fibre losses by a distributed amplification of the pump and the signal waves. Using Raman amplification measurement distances up to 100 km were achieved [11–14]. Since the spectrum of Raman amplification is much broader than spectra of phase-modulated pump and signal it should not introduce any distortion and, thus, can be directly applied in phase-correlation sensing.

4.2.3 Finding an optimal bit duration

In fact, the measurement time can vary even for a fixed number of points. As it was shown in section 2.2 the same spatial resolution can be achieved with multiple combinations of bit duration and sampling interval. Even though these combinations provide the same spatial resolution, the performance of the system (and, thus, the measurement time) are not the same. As it was shown in section 3.3.2 the imperfection of the phase modulation does not have a significant effect for a bit duration of 140 ps. Thus, it is possible to use the analytical expressions obtained for the perfectly rectangular modulation in order to find the values that give the shortest measurement time.

The measurement time t_{msr} is inversely proportional to the sampling interval, since a shorter sampling interval leads to more points being simultaneously addressed along the fibre. It is also inversely proportional to the square of the bit duration – the change in the signal intensity is linearly proportional to the bit duration, thus the required number of averages is reduced quadratically. Overall $t_{\mathrm{msr}} \propto 1/sd^2$; in order to find its minimum we rewrite the denominator using equation (2.24) for the sampling interval:

$$sd^2 = d^2\sqrt{-2d^2 + 4d\delta - \delta^2}\,. \tag{4.2}$$

Now we need to take its derivative in order to find the maximum position:

$$(sd^2)' = 2d\sqrt{-2d^2 + 4d\delta - \delta^2} + \frac{d^2}{2\sqrt{-2d^2 + 4d\delta - \delta^2}}(-4d + 4\delta), \tag{4.3}$$

$$d = \frac{(5 \pm \sqrt{13})}{6}\delta\,. \tag{4.4}$$

The maximum is achieved for the plus sign, giving $d = (5 + \sqrt{13})/6\delta \approx 1.43\delta$ with the corresponding sampling interval $s \approx 0.79\delta$. figure 4.4 shows how for a given spatial resolution the measurement time depends on the correlation peak size. We can see that for the derived $d \approx 1.43\delta$ the measurement time is 40 % shorter than for the straightforward solution of $d = \delta$.
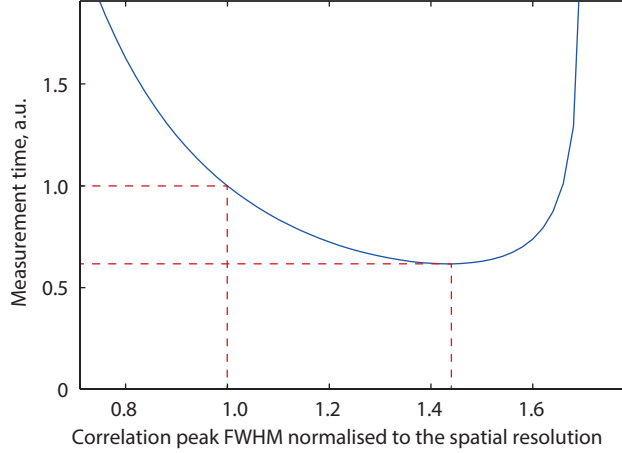
Figure 4.4: Measurement time for a given bit duration for a fixed spatial resolution.

4.3 Temperature-dependent position of correlation peaks

Every distributed fibre sensor uses the speed of light and the refractive index of the fibre[1] to determine the physical position of the interaction. For the phase-correlated technique this dependence is observed in equation (2.12):

$$z_{c,m} = \frac{c}{2n_{eff}} \left(m N_{bits} T_{bit} + t_{delay} \right) + \frac{L}{2} . \tag{4.5}$$

Refractive index defines the separation between correlation peaks and a shift of their positions due to a relative delay between the pump and the signal waves. As the temperature of the fibre changes so does the refractive index, affecting the correlation peak positioning. Thermal expansion also affects the propagation time, but it's effect on the propagation time is one order of magnitude smaller [62] and for simplicity it will not be considered in calculations. The change of the refractive index with the temperature is known to be $\xi = 10^{-5} \, K^{-1}$ [62]. For a small number of points this change is too small to affect the system in a significant way. However, as the number reaches hundreds of thousands of points, it can affect the longitudinal accuracy of the sensor which to be accounted for.

---

[1]Once again, a non-dispersive medium approximation is used, i.e. the group refractive index is considered to be equal to the phase refractive index.

4.3.1 Uniform temperature shift

Let's start with a simple case of a uniform temperature change along the fibre, leading to a change in the effective refractive index of Δn_{eff}. In this case the equation (4.5) can be applied directly to find the new position of the correlation peak:

$$
\begin{aligned}
z'_{\text{c},m} &= \frac{c}{2(n_{\text{eff}} + \Delta n_{\text{eff}})}(mN_{\text{bits}}T_{\text{bit}} + t_{\text{delay}}) + \frac{L}{2} \\
&\approx \frac{c}{2n_{\text{eff}}}(mN_{\text{bits}}T_{\text{bit}} + t_{\text{delay}})\left(1 - \frac{\Delta n_{\text{eff}}}{n_{\text{eff}}}\right) + \frac{L}{2}\,.
\end{aligned}
\tag{4.6}
$$

The difference between equations (4.5) and (4.6) gives the amount by which the correlation peak position shifts due to the temperature change:

$$
\begin{aligned}
\Delta z_{\text{c},m} &= -\frac{\Delta n_{\text{eff}}}{n_{\text{eff}}}\frac{c}{2n_{\text{eff}}}(mN_{\text{bits}}T_{\text{bit}} + t_{\text{delay}}) \\
&= -\frac{\Delta n_{\text{eff}}}{n_{\text{eff}}}\left(z_{\text{c},m} - \frac{L}{2}\right)\,.
\end{aligned}
\tag{4.7}
$$

The change in the position of the correlation peak is proportional to its initial distance from the centre of the fibre, thus, affecting the most the measurements at the beginning and at the end of the fibre.

To check this dependence the Brillouin frequency shift was measured around a hotspot positioned at the end of a 17.5 km long fibre for three values of the ambient temperature, results of this measurements are shown on figure 4.5. It can be seen that the measured position of the correlation peak increases with the temperature, changing by 27 cm when the temperature grows by 5 K which is in a good agreement with equation (4.7):

$$
\frac{\Delta n_{\text{eff}}}{n_{\text{eff}}}\left(z_{\text{c},m} - \frac{L}{2}\right) = \frac{5 \times 10^{-5}}{1.44}\left(17.5\,\text{km} - \frac{17.5\,\text{km}}{2}\right) = 30\,\text{cm}\,.
\tag{4.8}
$$

4.3.2 Arbitrary temperature distribution

In order to find how the correlation peak positioning changes for an arbitrary distribution of refractive index (given by the temperature) we have to rewrite equations (2.7) and (2.8) for the propagation times of the pump and the signal waves and then use equation (2.11) to find positions of the correlation peaks. Equations for the propagation times are:

$$
t_{\text{p}}(z) = \frac{1}{c}\int_0^z n_{\text{eff}}(z)\,\mathrm{d}z\,,
\tag{4.9}
$$

$$
t_{\text{s}}(z) = \frac{1}{c}\int_z^L n_{\text{eff}}(z)\,\mathrm{d}z + t_{\text{delay}}\,.
\tag{4.10}
$$
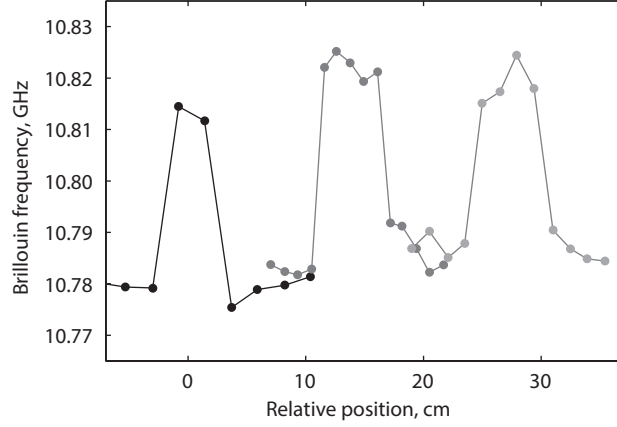
Figure 4.5: Measured Brillouin frequency shift along the fibre for several ambient temperatures

Combining them together it is possible to write the equation for the position of the correlation peaks:

$$\frac{1}{c}\int_{0}^{z_{\text{c},m}} n_{\text{eff}}(z)\, \mathrm{d}z = \frac{1}{c}\int_{z_{\text{c},m}}^{L} n_{\text{eff}}(z)\, \mathrm{d}z + t_{\text{delay}} + mT_{\text{bit}}N_{\text{bits}}. \tag{4.11}$$

During a measurement multiple points are acquired, let's define $t = t_{\text{delay}} + mT_{\text{bit}}N_{\text{bits}}$ – the position of a measurement point in time domain, which is known since all the elements that define it are known. For each point the temperature $T_t(t)$ (that can be converted to a refractive index $\bar{n}_{\text{eff},t}(t)$) is measured.[2] The goal is to find the dependence $z(t)$ which allows to position all the measured points at correct locations. Let's define two limiting time points t_0 and t_{end} so that $z(t_0) = 0$ and $z(t_{end}) = L$. Rewriting equation (4.11) using newly defined variables we can get a shorter form[3]

$$\frac{1}{c}\int_{0}^{z(t)} n_{\text{eff}}(x)\, \mathrm{d}x = \frac{1}{c}\int_{z(t)}^{L} n_{\text{eff}}(x)\, \mathrm{d}x + t\,, \tag{4.12}$$

$$\int_{0}^{z(t)} n_{\text{eff}}(x)\, \mathrm{d}x - \int_{z(t)}^{L} n_{\text{eff}}(x)\, \mathrm{d}x = ct\,. \tag{4.13}$$

---

[2]The subscript t is used to distinguish between the measured distribution in time domain and the distribution in distance that we want to find.

[3]Variable x will be used for the longitudinal coordinate under the integral, while z will be used for the integral range.

We also rewrite $n_{\text{eff}}(z)$ as a sum of its average and a small variation $\Delta n_{\text{eff}}(z)$:

$$n_{\text{eff}}(z) = \bar{n}_{\text{eff}} + \Delta n_{\text{eff}}(z) \,. \tag{4.14}$$

The average refractive index $\bar{n}_{\text{eff}}$ can be found knowing the average of longitudinal temperature distribution $T(z)$, which in first approximation is equal the average of the measured $T_t(t)$. Similarly we can rewrite $z(t)$ as the sum of the zero order approximation and a variation:

$$z(t) = \frac{L}{2} + \frac{ct}{2\bar{n}_{\text{eff}}} + \Delta z(t) \,. \tag{4.15}$$

Let's also note that by the definition of average:

$$\frac{1}{L} \int_0^L n_{\text{eff}}(z) \,\mathrm{d}z \equiv \bar{n}_{\text{eff}} \,, \tag{4.16}$$

therefore:

$$\int_0^L \Delta n_{\text{eff}}(z) \,\mathrm{d}z \equiv 0 \,. \tag{4.17}$$

Using this, we can rewrite the left term of equation (4.13):

$$\int_0^{z(t)} n_{\text{eff}}(x) \,\mathrm{d}x - \int_{z(t)}^L n_{\text{eff}}(x) \,\mathrm{d}x = \int_0^{z(t)} n_{\text{eff}}(x) \,\mathrm{d}x - \left(\int_0^L n_{\text{eff}}(x) \,\mathrm{d}x - \int_0^{z(t)} n_{\text{eff}}(x) \,\mathrm{d}x \right)$$

$$= 2 \int_0^{z(t)} n_{\text{eff}}(x) \,\mathrm{d}x - \bar{n}_{\text{eff}} L \,, \tag{4.18}$$

and thus rewrite the integral equation (4.13) in an even simpler form

$$2 \int_0^{z(t)} n_{\text{eff}}(x) \,\mathrm{d}x = ct + \bar{n}_{\text{eff}} L \,. \tag{4.19}$$

By using t_0 as the argument for this equation and remembering that $z(t_0) = 0$ we can obtain a simple equation for $\bar{n}_{\text{eff}}$

$$\bar{n}_{\text{eff}} = -\frac{ct_0}{L} \,. \tag{4.20}$$

The integral term of this equation can be rewritten in terms of time-domain coordinate:

$$2 \int\limits_{0}^{z(t)} n_{\text{eff}}(x)\,\mathrm{d}x = 2 \int\limits_{t_0}^{t} \bar{n}_{\text{eff},t}(\tau)\,\mathrm{d}\left(\frac{L}{2} + \frac{c\tau}{2\bar{n}_{\text{eff}}} + \Delta x(\tau)\right)$$

$$= 2 \int\limits_{t_0}^{t} \left(\bar{n}_{\text{eff}} + \Delta\bar{n}_{\text{eff},t}(\tau)\right)\left(\frac{c}{2\bar{n}_{\text{eff}}} + \Delta x'(\tau)\right)\mathrm{d}\tau$$

$$\approx \int\limits_{t_0}^{t} \left(c + \frac{\Delta\bar{n}_{\text{eff},t}(\tau)c}{\bar{n}_{\text{eff}}} + 2\bar{n}_{\text{eff}}\Delta x'(\tau)\right)\mathrm{d}\tau \qquad (4.21)$$

$$= c(t - t_0) + \frac{c}{\bar{n}_{\text{eff}}} \int\limits_{t_0}^{t} \Delta\bar{n}_{\text{eff},t}(\tau)\,\mathrm{d}\tau + 2\bar{n}_{\text{eff}} \int\limits_{t_0}^{t} \Delta x'(\tau)\,\mathrm{d}\tau$$

$$= c(t - t_0) + \frac{c}{\bar{n}_{\text{eff}}} \int\limits_{t_0}^{t} \Delta\bar{n}_{\text{eff},t}(\tau)\,\mathrm{d}\tau + 2\bar{n}_{\text{eff}}(\Delta z(t) - \Delta z(t_0)).$$

Remembering that $\bar{n}L = -ct_0$ (equation (4.20)) and $\Delta z(t_0) = 0$ (since $z(t_0)$ is equal to zero by the definition of t_0) let's return to equation (4.21):

$$c(t - t_0) + \int\limits_{t_0}^{t} \Delta\bar{n}_{\text{eff},t}(\tau)\,\mathrm{d}\tau + 2\bar{n}_{\text{eff}}\Delta z(t) = -ct_0 + ct, \qquad (4.22)$$

$$\Delta z(t) = -\frac{c}{2\bar{n}_{\text{eff}}^2} \int\limits_{t_0}^{t} \Delta\bar{n}_{\text{eff},t}(\tau)\,\mathrm{d}\tau. \qquad (4.23)$$

Or, in terms of the temperature (as before, $\xi = 10^{-5}K^{-1}$ is the refractive index change with the temperature):

$$\Delta z(t) = -\frac{c\xi}{2\bar{n}_{\text{eff}}^2} \int\limits_{t_0}^{t} \Delta T(\tau)\,\mathrm{d}\tau. \qquad (4.24)$$

Figure 4.6 shows how this algorithm can be applied. The measured temperature distribution gets integrated and $\Delta z(t)$ is calculated from it. After that, this displacement is added to the zero order approximation (equation (4.15)) leading to the final equation for the dependence of longitudinal position on the position in time domain:

$$z(t) = \frac{L}{2} + \frac{ct}{2\bar{n}_{\text{eff}}} - \frac{c\xi}{2\bar{n}_{\text{eff}}^2} \int\limits_{t_0}^{t} \Delta T(\tau)\,\mathrm{d}\tau. \qquad (4.25)$$
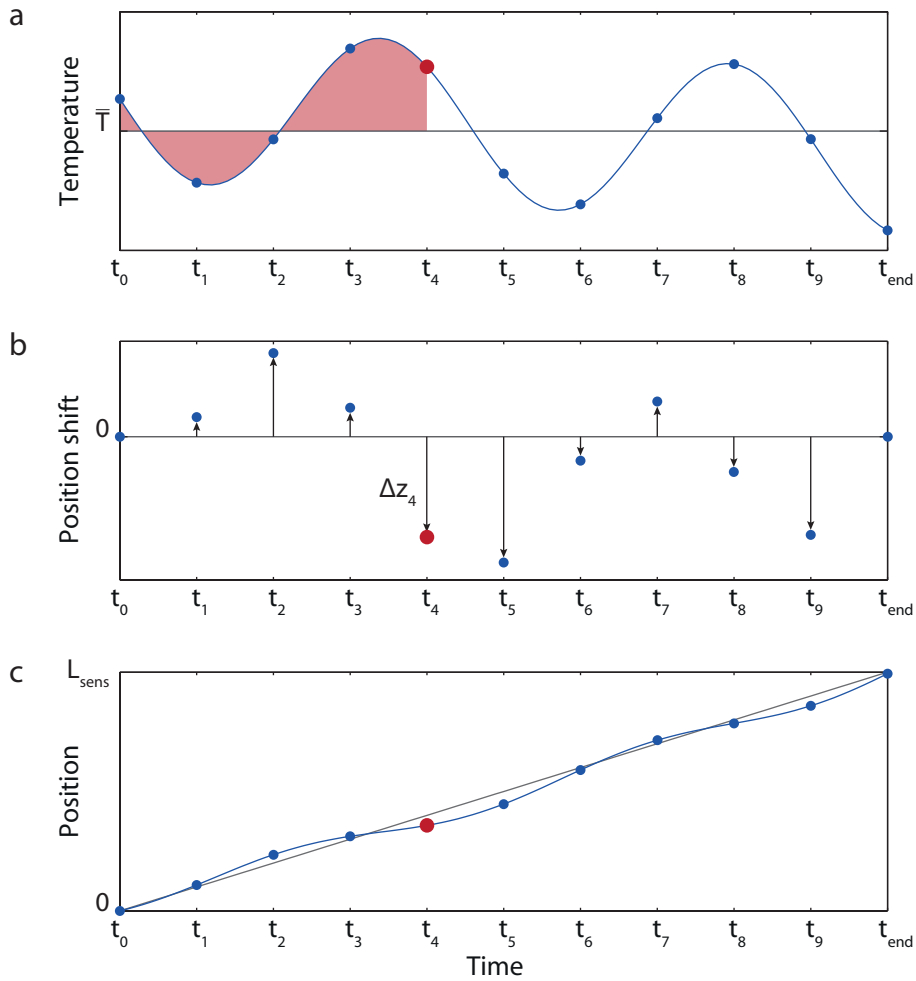
Figure 4.6: Compensation of positioning for the temperature varying along the fibre: a) integrating the measured temperature distribution; b) calculating displacement for each point; c) adding displacement to the zero order approximation of the uniform temperature.

Using this equation it's possible to correctly determine longitudinal position of measured data points, accounting for the temperature-dependent refractive index variation.

4.4   Discussion

Summing things up we can see that while there are multiple problems standing in the way of further improving the number of points resolved using phase-correlation technique, there exist techniques that to some extent allow overcoming them. The measurement time of a sensor can be improved – without changing the experimental setup – by choosing the optimal combination of correlation peak size and sampling interval. It means that clearly there is a margin for increasing performance of the phase-correlation technique.

As the number of points will go up the issue of the temperature dependence of the refractive index will become more pronounced. Still, the presented algorithm will be able to compensate for it, unless extreme temperatures are used. However, since Brillouin frequency shift depends not only on temperature but also on strain, the measurement has to be organised in a way that prevents transversal load of the fibre. With minor modifications this algorithm can be applied to other distributed temperature sensors, e.g. BOTDA.

Chapter 5

Brillouin dynamic gratings in polarisation-maintaining fibres

As it was shown in section 1.2, the acoustic wave generated during the SBS works as a distributed reflector, with the same working principle as fibre Bragg gratings (FBG's). This allows dynamically creating FBG's with lengths of metres or tens of metres – length unachievable by the traditional methods of FBG creation: the interferometric method utilising an ultraviolet laser and the point-by-point writing by femtosecond pulses. Such dynamically generated reflectors are called Brillouin dynamic gratings (BDG's).

Due to the Doppler effect, a dynamic grating has two reflection peaks for two propagation directions. The frequencies of these two peaks are equal to frequencies of two pumps – the light waves used to create the BDG. Thus in a standard single-mode fibre the spectrum of light reflected for a BDG will overlap with the spectrum of one of the pump waves, making it problematic to isolate just the reflection. While it was shown to be possible [63], a combination of very weak birefringence and temperature dependence of the refractive index makes such a system unstable in time.

This issue can be circumvented by using highly birefringent optical fibres, also called polarisation maintaining (PM) fibres. In such fibres the axial symmetry is broken, separating the two polarisation modes which significantly facilitates usage of BDG's. This technique has found many applications such as high-resolution temperature sensing [5], microwave filter generation [6, 36], and optical signal processing [7, 35]. This chapter is dedicated to finding new applications of BDG's for optical signal processing and filtering.

5.1   Brillouin dynamic gratings theory

One of the most commonly used type of PM fibre is made by drilling two holes in the fibre preform and inserting rods of glass with different properties. After the fibre is drawn and
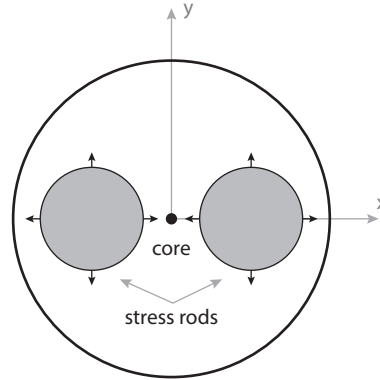
Figure 5.1: Panda fibre profile

starts cooling down these rods introduce transversal stress due to a difference between thermal expansion coefficients. This transversal stress changes the refractive index along one of the axes, inducing the birefringence. Due to the resulting fibre profile, depicted on figure 5.1, this type of fibre is called Panda.

5.1.1 BDG generation

Let's think of the BDG as a uniform fibre Bragg grating, generated by two counterprogating optical waves – *pump 1* and *pump 2* – polarised along the x-axis of a PM fibre, with the frequency detuning between them corresponding to the Brillouin frequency shift:

$$\nu_{B,x} = \frac{2n_x V_a}{\lambda_x} = \frac{2n_x V_a \nu_p}{c} \, , \tag{5.1}$$

where ν_p is the average frequency of two pumps[1]. The physical pitch of the dynamic grating is given by the interference between the two waves:

$$\Lambda = \frac{c}{2n_x \nu_p} \, . \tag{5.2}$$

For the light polarised along the y axis the resonant frequency given by this pitch will be different due to a different refractive index, giving the following equation for the resonant frequency of the probe wave:

$$\nu_{pr} = \frac{c}{2n_y \Lambda} = \frac{n_x}{n_y} \nu_p \, . \tag{5.3}$$

---

[1]Which for most practical applications can be replaced by the frequency of either of them.

66
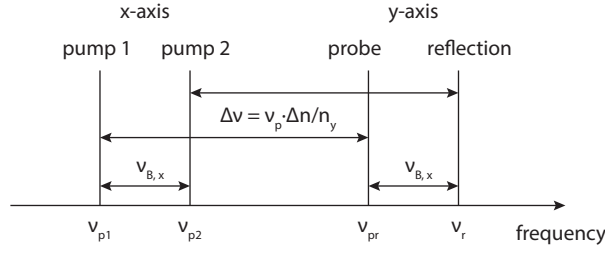
Figure 5.2: Frequencies of waves participating in generation and read-out of a BDG

Thus, the difference between pump 1 and the resonant probe wave is:

$$\Delta \nu = \nu_{\mathrm{pr}} - \nu_{\mathrm{p}} = \frac{n_x - n_y}{n_y} \nu_{\mathrm{p}} = \frac{\Delta n}{n_y} \nu_{\mathrm{p}}. \tag{5.4}$$

It can be easily seen that $\Delta \nu$ also gives frequency difference between pump 2 and the reflected wave (which is spectrally shifted from the probe due to the Doppler effect). Figure 5.2 shows frequencies of all the waves participating in a BDG experiment. Since the pump waves and the probe and its reflection are polarised along different axes and separated spectrally, it is quite easy to isolate the probe's reflection. It opens possibilities of applying the BDG's to various sorts of signal processing.

Now we should derive more strict equations that will allow us, for example, finding the time dependence of a pulse reflection. Once again we consider two counterpropagating continuous pump waves polarised along the x-axis. Their frequencies are $\omega_{\mathrm{p}1}$ and $\omega_{\mathrm{p}2}$, and the wave vectors are $k_{\mathrm{p}1} = n_x \omega_{\mathrm{p}1}/c$ and $k_{\mathrm{p}2} = n_x \omega_{\mathrm{p}2}/c$. The amplitude of the acoustic wave generated by the two pump waves is given by equations (1.10) and (1.41)[2]:

$$Q = \frac{g_1 A_{\mathrm{p}1} A_{\mathrm{p}2}^*}{\Gamma_{\mathrm{A}}}, \tag{5.5}$$

where $\Omega = \omega_{\mathrm{p}1} - \omega_{\mathrm{p}2}$, while the total acoustic wave is

$$\rho_{\mathrm{tot}} = \rho_0 + \left[Q e^{j(qz - \Omega t)} + \mathrm{c.c.} \right]. \tag{5.6}$$

where $q = k_{\mathrm{p}1} + k_{\mathrm{p}2}$.

Let's introduce a probe wave which is polarised along the y-axis and is copropagating with pump 1:

$$E_{\mathrm{pr}} = A_{\mathrm{pr}} e^{j(k_{\mathrm{pr}}z - \omega_{\mathrm{pr}}t)} + \mathrm{c.c.} \tag{5.7}$$

---

[2]Assuming that amplitudes of both pumps remain constant, i.e. the Brillouin interaction between them is weak.

Using equation (1.31) we can write the nonlinear polarisation, keeping only the first order frequency components:

$$
\begin{aligned}
P &= \epsilon_0 \rho_0^{-1} \gamma_e \left(Q e^{j(qz-\Omega t)} + \text{c.c.} \right) \left(A_{\text{pr}} e^{j(k_{\text{pr}}z - \omega_{\text{pr}}t)} + \text{c.c.} \right) \\
&= \epsilon_0 \rho_0^{-1} \gamma_e \left(Q^* A_{\text{pr}} e^{j(-(q-k_{\text{pr}})z - (\omega_{\text{pr}}-\Omega)t)} + \text{c.c.} \right).
\end{aligned}
\tag{5.8}
$$

This nonlinear polarisation will generate a reflected wave with frequency $\omega_{\text{r}} = \omega_{\text{pr}} - \Omega$ and wave vector $k_{\text{r}} = n_y \omega_{\text{r}}/c$. The highest reflection will occur when the nonlinear polarisation is phase-matched with the reflected wave, i.e. when $q - k_{\text{pr}} = k_{\text{r}}$. This allows for calculating the central wavelength of the dynamic grating:

$$
q - k_{\text{pr}} = n_y \omega_{\text{r}}/c
\tag{5.9}
$$

$$
k_{\text{p1}} + k_{\text{p2}} - k_{\text{pr}} = n_y \omega_{\text{r}}/c
\tag{5.10}
$$

$$
(n_x(2\omega_{\text{p1}} - \Omega) - n_y \omega_{\text{pr}})/c = n_y(\omega_{\text{pr}} - \Omega)/c
\tag{5.11}
$$

$$
n_x(2\omega_{\text{p1}} - \Omega) = n_y(2\omega_{\text{pr}} - \Omega).
\tag{5.12}
$$

Since $(n_x - n_y)\Omega$ is a second-order term, it can be neglected simplifying the equation:

$$
n_x \omega_{\text{p1}} = n_y \omega_{\text{pr}}.
\tag{5.13}
$$

or

$$
\omega_{\text{pr}} = \frac{n_x}{n_y} \omega_{\text{p1}},
\tag{5.14}
$$

$$
\Delta\omega = \omega_{\text{pr}} - \omega_{\text{p1}} = \frac{\Delta n}{n} \omega_{\text{p1}},
\tag{5.15}
$$

the same result as equation (5.4), obtained with the simple FBG model.

5.1.2   Reflection from a dynamic grating

Let's see what happens when a rectangular probe pulse is sent onto the BDG in a general case, when the birefringence may vary along the fibre. We start with rewriting the nonlinear polarisation obtained in equation (5.8) using $\omega_{\text{r}} = \omega_{\text{pr}} - \Omega$, the frequency of the reflected light, and $K = q - k_{\text{pr}}$, the wave vector of the nonlinear polarisation wave (and, therefore, of the BDG):

$$
P = \epsilon_0 \rho_0^{-1} \gamma_e \left(Q^* A_{\text{pr}} e^{j(-Kz - \omega_{\text{r}}t)} + \text{c.c.} \right).
\tag{5.16}
$$

The wave vector of the reflected light is

$$
k_{\text{r}} = \frac{\omega_{\text{r}} n_y}{c}.
\tag{5.17}
$$

As it was mentioned before, the resonant case of probe being perfectly tuned to the grating's reflection peak corresponds to the case of $K = k_r$. This condition does not necessarily holds, but we can write $k_r = K + \Delta k$, where Δk corresponds to the difference between two wave vectors due to the probe's detuning from the resonance and/or birefringence variations.

Let's look for a solution for the reflected wave in the form of:

$$E_r = A_r(z, t)e^{j(-Kz-\omega_r t)} + \text{c.c.} \tag{5.18}$$

The wave equation for the electrical fields (equation (1.30)) will look this way[3]

$$-K^2 A_r - j2K\frac{\partial A_r}{\partial z} + \frac{\omega_r^2 n_y^2}{c^2}A_r + j\frac{2\omega_r n_y^2}{c^2}\frac{\partial A_r}{\partial t} = -\frac{\omega_r^2 \gamma_e}{\rho_0 c^2}Q^* A_{pr}. \tag{5.19}$$

Using $K = k_r - \Delta k$, remembering $\omega_r n_y/c = k_r$, and keeping only the first order terms:

$$-(k_r^2 - 2k_r\Delta k + \Delta k^2)A_r - j2K\frac{\partial A_r}{\partial z} + k_r^2 A_r + j\frac{k_r n_y}{c}\frac{\partial A_r}{\partial t} = -\frac{\omega_r^2 \gamma_e}{\rho_0 c^2}Q^* A_{pr}, \tag{5.20}$$

$$+2k_r\Delta k A_r - j2K\frac{\partial A_r}{\partial z} + j\frac{k_r n_y}{c}\frac{\partial A_r}{\partial t} = -\frac{\omega_r^2 \gamma_e}{\rho_0 c^2}Q^* A_{pr}. \tag{5.21}$$

This equation can be rewritten for a steady-state condition:

$$-2k_r\Delta k A_r + j2K\frac{\partial A_r}{\partial z} = \frac{\omega_r^2 \gamma_e}{\rho_0 c^2}Q^* A_{pr}. \tag{5.22}$$

Remembering $K \approx k_r$, elasto-optic coefficient $g_2 = \omega\gamma_e/2nc\rho_0$[4], and reintroducing the longitudinal dependence of variables:

$$j\Delta k(z)A_r + \frac{\partial A_r}{\partial z} = -j\frac{\omega_r \gamma_e}{2\rho_0 c n_y}Q^* A_{pr}(z), \tag{5.23}$$

$$j\Delta k(z)A_r + \frac{\partial A_r}{\partial z} = -jg_2 Q^* A_{pr}\exp\left(j\int_{z_0}^{z}\Delta k(\zeta)\,\mathrm{d}\zeta\right), \tag{5.24}$$

where the phase term in A_{pr} appears due to propagation in a nonuniform fibre, assuming the BDG with length L which starts at z_0. This equation can be solved (details can be found in appendix B):

$$A_r(z_0) = jg_2 Q^* A_{pr}\int_{z_0}^{z_0+L}\exp\left(j\int_{z_0}^{\xi}2\Delta k(\zeta)\,\mathrm{d}\zeta\right)\mathrm{d}\xi. \tag{5.25}$$

---

[3]Assuming slowly varying amplitudes

[4]Here and further ω will be used instead of ω_{p1}, ω_{p2}, ω_{pr}, and ω_r when the difference between the four frequencies is insignificant; same way n will be used instead of n_x and n_y.
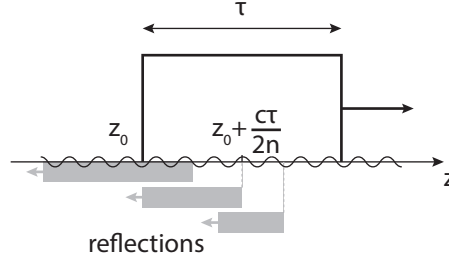
Figure 5.3: Reflections from a probe pulse. Note that reflections from positions farther than $z_0 + c\tau/2n$ did not reach z_0 yet

This equation represents a sum of reflections from the whole fibre with each one having a phase shift due to the refractive index variation along the fibre up to the point of reflection.

This solution can be applied to the case of a reflection from a pulse with duration τ. Let's consider an infinite BDG and see what happens at the moment at which the pulse has just passed z_0, as seen on figure 5.3. The reflected signal at position z_0 is an integral of reflections from z_0 to $z_0 + c\tau/2n$, since reflections from farther regions did not reach z_0 yet. At this position in time for the section between z_0 and $z_0 + c\tau/2n$ the situation is indistinguishable from the steady-state case with the BDG being generated solely within this region. Thus, the reflection at z_0 can be found using equation (5.25):

$$A_{\mathrm{r}}(z = z_0) = j g_2 Q^* A_{\mathrm{pr}}(z_0) \int_{z_0}^{z_0+c\tau/2n} \exp\left(j \int_{z_0}^{\xi} 2\Delta k(\zeta)\,\mathrm{d}\zeta \right) \mathrm{d}\xi \,. \tag{5.26}$$

Let's set $t = 0$ to the moment when the back edge of the pulse enters the BDG. At a moment t it will reach position $z = ct/n$:

$$A_{\mathrm{r}}(z = ct/n, t) = j g_2 Q^* A_{\mathrm{pr}}(z = ct/n) \int_{ct/n}^{ct/n+c\tau/2n} \exp\left(j \int_{ct/n}^{\xi} 2\Delta k(\zeta)\,\mathrm{d}\zeta \right) \mathrm{d}\xi \,, \tag{5.27}$$

and at the moment $2t$ the reflection from this point will come back to the beginning of the BDG. The probe amplitude $A_{\mathrm{pr}}(z = ct/n, t)$ is given by the probe amplitude at the entrance of BDG with an additional phase shift due to the variation of the refractive index:

$$A_{\mathrm{pr}}(z = ct/n) = A_{\mathrm{pr}}(z = 0) \exp\left(\int_{0}^{\frac{ct}{2n}} \Delta k(\xi)\,\mathrm{d}\xi \right) \,. \tag{5.28}$$

During the backpropagation the reflected signal will accumulate the same phase shift. We can now write the equation for the reflected signal at the entrance of the BDG at a given time:

$$A_\mathrm{r}(z=0,t) = jg_2 Q^* A_\mathrm{pr} e^{j\phi(t)} \int_{\frac{ct}{2n}}^{\frac{c(t+\tau)}{2n}} \exp\left(j\int_{\frac{ct}{2n}}^{\xi} 2\Delta k(\zeta)\,\mathrm{d}\zeta\right)\mathrm{d}\xi\,, \qquad (5.29)$$

$$\phi(t) = 2\int_0^{\frac{ct}{2n}} \Delta k(\xi)\,\mathrm{d}\xi\,. \qquad (5.30)$$

For a short pulse we can consider Δk to be constant within the distance $c\tau/2n$, and equation (5.29) can be simplified:

$$\begin{aligned}
A_\mathrm{r}(z=0,t) &= jg_2 Q^* A_\mathrm{pr} e^{j\phi(t)} \int_{\frac{ct}{2n}}^{\frac{c(t+\tau)}{2n}} \exp\left(j\int_{\frac{ct}{2n}}^{\xi} 2\Delta k\left(\frac{ct}{2n}\right)\mathrm{d}\zeta\right)\mathrm{d}\xi \\
&= jg_2 Q^* A_\mathrm{pr} e^{j\phi(t)} \int_{\frac{ct}{2n}}^{\frac{c(t+\tau)}{2n}} \exp\left(j2\Delta k\left(\frac{ct}{2n}\right)\left(\xi - \frac{ct}{2n}\right)\right)\mathrm{d}\xi \\
&= jg_2 Q^* A_\mathrm{pr} e^{j\phi(t)} \frac{\exp\left(j2\Delta k\left(\frac{ct}{2n}\right)\frac{c\tau}{2n}\right) - 1}{j2\Delta k\left(\frac{ct}{2n}\right)} \\
&\approx jg_2 Q^* A_\mathrm{pr} e^{j\phi(t)} \frac{c\tau}{2n}\,.
\end{aligned} \qquad (5.31)$$

5.2 Flip-flop

A classical flip-flop is and electronic circuit that has two stable states which are associated with logical 0 and 1. A flip-flop can be switched from one state to another using an electrical signal, enabling the usage flip-flops as storage elements. This makes them fundamental building blocks in digital electronics systems, including computers and communication devices. For a long time research activities have been carried out to create all-optical logic circuits which would ultimately lead to creation of a photonic computer, where information is stored and processed by optical means. This chapter demonstrates that an ideal distributed reflector can be used to create a all-optical flip-flop.

The reflection of a short pulse on a distributed reflector is a rectangular pulse (figure 5.4a). If two consecutive in-phase pulses are sent on the reflector their reflections will overlap, creating a reflection with amplitude twice as large (figure 5.4b). If the phase
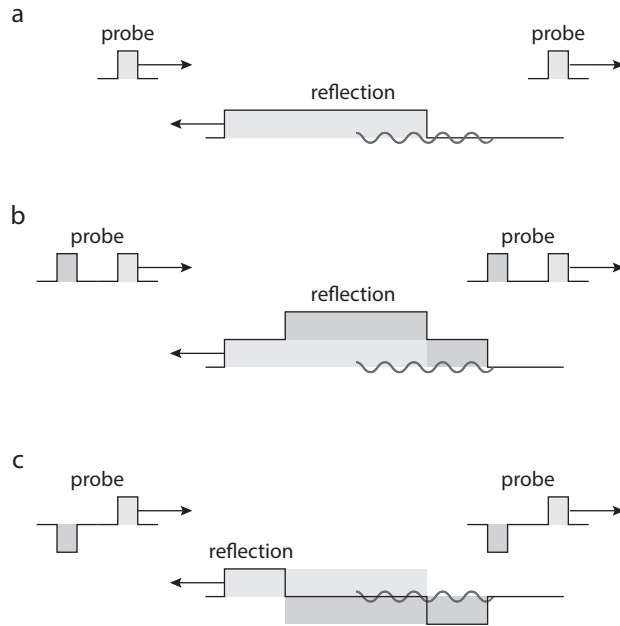
Figure 5.4: Pulse reflection from a distributed reflector. a) Single pulse produces rectangular reflection; b) Reflections from two consecutive pulses sum up intro a reflection with double amplitude; c) Reflections from two pulses with opposite phases cancel each other.

of the second pulse is shifted by π, two reflections will be out of phase, cancelling each other (figure 5.4c). Thus, a flip-flop can be created: one short pulse is used to switch it on, while turning off is achieved with another pulse with an opposite phase. The maximum storage time is given by the length of the reflector, while the switching time is given by the duration of the control pulses. This makes BDG's very attractive for this application as their length can potentially reach tens or even hundreds of metres.

5.2.1 Experimental setup

An experimental setup for the demonstration of an all-optical flip-flop is shown on figure 5.5 and it consists of two main parts. The first one is used to generate the BDG along a PM fibre. The output of a DFB laser, polarised along x-axis, is split into two branches with a coupler[5]. The light in the top branch corresponds to pump 2; it gets amplified by an EDFA to a power level of ~25 dB and is launched into a 20 m long PM fibre.

---

[5] All of the components of the setup are polarisation-maintaining unless specified otherwise
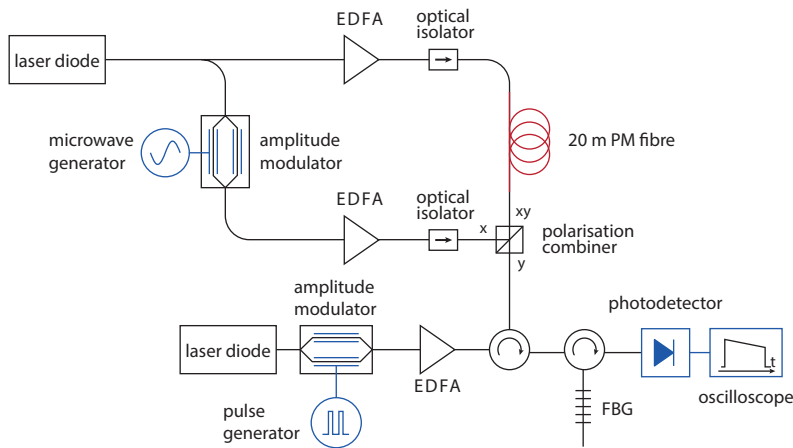
Figure 5.5: Experimental setup for the flip-flop experiment

In the bottom branch the light passes through an electro-optic modulator (EOM) driven by an RF generator with frequency corresponding to the Brillouin frequency of the PM fibre; thus, a two side-band pump 1 is generated. The side-bands are amplified by an EDFA to reach a power similar to pump 2 (the powers were tuned during the experiment to avoid nonlinearities, depletion, and other detrimental effects) and is launched into the PM fibre through a polarisation-dependent splitter. Note, that since pump 1 contains two spectral components, two gratings are generated inside the fibre, their resonant frequencies are separated by the double of the Brillouin frequency shift of the fibre, and either of the gratings can be used in the experiment.

In the second part of the experimental setup the probe wave is generated. The frequency of another DFB laser is tuned to match the resonant frequency of one of the BDG's in y-polarisation. Its output passes through an EOM driven by a pulse generator, amplified by an EDFA, and sent into the PM fibre through the polarisation splitter that aligns the polarisation of the probe along the y-axis. The signal reflected from the BDG is filtered on a fibre Bragg grating and is sent on a photodetector with a 5 GHz bandwidth connected to an oscilloscope.

Figure 5.6 shows the spectrum measured at the entrance of the FBG filter in the detection system. We can see a strong component of pump 2 which leaks into detection due to a cross-talk between two polarisations. The Rayleigh scattering is observed for two side-lobes of pump 1 and the probe. Yet, the probe and the reflection are well separated spectrally from pump waves which makes it easy to use an FBG to filter out everything but the reflection.
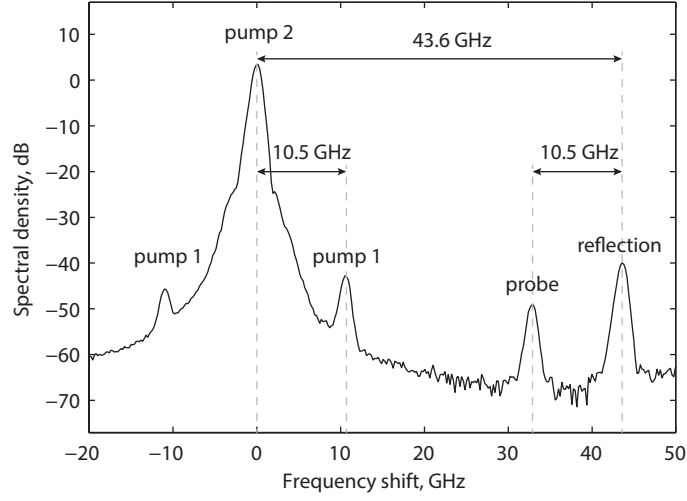
Figure 5.6: Measured spectrum of optical waves participating in the BDG experiment

5.2.2   Reflection of two pulses

Since two pulses are required to create a flip-flop it is necessary to calculate the signal that would be given by the interference of two pulses separated by Δt_{p}. Let's consider both pulses belonging to the same optical wave: $A_{\mathrm{pr},1} = A_{\mathrm{pr},2} = A_{\mathrm{pr}}$. We will also assume the pulses to be short enough to ignore the birefringence variation within their size – this way we can apply equation (5.31) to find the sum of two reflections:

$$
\begin{aligned}
A_{\mathrm{r,sum}}(t) &= A_{\mathrm{r}}(z = 0, t) + A_{\mathrm{r}}(z = 0, t - \Delta t_{\mathrm{p}}) \\
&= -j g_2 Q^* A_{\mathrm{pr}} \frac{c\tau}{2n} \left(e^{j\phi(t)} + e^{j\phi(t-\Delta t_{\mathrm{p}})} \right).
\end{aligned}
\tag{5.32}
$$

Using a simple formula for the sum of two complex exponents:

$$
e^{ja} + e^{jb} = 2 e^{j\frac{a+b}{2}} \cos\left(\frac{a-b}{2} \right),
\tag{5.33}
$$

it can be rewritten:

$$
\begin{aligned}
A_{\mathrm{r,sum}} &= -j g_2 Q^* A_{\mathrm{pr}} \frac{c\tau}{2n} \exp\left(j \frac{\phi(t) + \phi(t - \Delta t_{\mathrm{p}})}{2} \right) \cos\left(\frac{\phi(t) - \phi(t - \Delta t_{\mathrm{p}})}{2} \right) \\
&= -j g_2 Q^* A_{\mathrm{pr}} \frac{c\tau}{2n} \exp\left(j \frac{\phi(t) + \phi(t - \Delta t_{\mathrm{p}})}{2} \right) \cos\left(\frac{\Delta\phi(t, \Delta t_{\mathrm{p}})}{2} \right),
\end{aligned}
\tag{5.34}
$$

where $\Delta\phi(t, \Delta t_{\mathrm{p}})$ is the phase mismatch accumulated between the two points of reflection, which can be found using equation (5.30):

$$\Delta\phi(t, \Delta t_{\mathrm{p}}) = 2 \int\limits_{0}^{\frac{ct}{2n}} \Delta k(\xi)\,\mathrm{d}\xi - 2 \int\limits_{0}^{\frac{c(t-\Delta t_{\mathrm{p}})}{2n}} \Delta k(\xi)\,\mathrm{d}\xi = 2 \int\limits_{\frac{c(t-\Delta t_{\mathrm{p}})}{2n}}^{\frac{ct}{2n}} \Delta k(\xi)\,\mathrm{d}\xi\,. \tag{5.35}$$

In a uniform fibre without variations in birefringence the wave vector mismatch Δk is constant along the fibre; thus, this phase mismatch can be significantly simplified:

$$\Delta\phi(t, \Delta t_{\mathrm{p}}) = \frac{c\Delta t_{\mathrm{p}}}{n}\Delta k\,, \tag{5.36}$$

or, in terms of $\Delta\omega$, the frequency mismatch between the probe and the BDG peak:

$$\Delta\phi(t) = \Delta\omega\Delta t_{\mathrm{p}}\,. \tag{5.37}$$

Which gives the equation for the intensity of the reflection:

$$I_{\mathrm{r,sum}} = g_2^2|Q|^2 I_{\mathrm{pr}} \frac{c^2\tau^2}{4n^2} \cos^2(\Delta\omega\Delta t_{\mathrm{p}})\,, \tag{5.38}$$

using equation (5.5) for the acoustic wave amplitude, it can be rewritten:

$$I_{\mathrm{r,sum}} = \frac{g_1^2 g_2^2}{|\Gamma_{\mathrm{A}}|^2} I_{\mathrm{p1}} I_{\mathrm{p2}} I_{\mathrm{pr}} \frac{c^2\tau^2}{4n^2} \cos^2(\Delta\omega\Delta t_{\mathrm{p}})\,. \tag{5.39}$$

In order to check the birefringence uniformity of the 20 m PM fibre, two consecutive pulses were used to probe the BDG. The pulses were separated by 3 ns and their duration was set to the minimum available value of 350 ps. Figure 5.7a shows the measured reflection – the interference between reflections of two pulses. The signal shows strong oscillations, meaning that a phase shift of π can be accumulated within a back-and-forth propagation through a 30 cm section of fibre (given by the 3 ns separation between two pulses). The drop in the reflection intensity along the fibre can be explained by the depletion of pump 1 due to it's Brillouin interaction with pump 2.

To verify that the oscillations are indeed given by the variations of the birefringence, the experiment was repeated with the two ends of the PM fibre swapped (the beginning became the end and vice versa). The measured reflection intensity is shown on figure 5.7b, with the time inversed for an easier comparison with the first measurement. Two interference pattens match each other well, proving that the reason behind them is indeed the variations within the fibre.
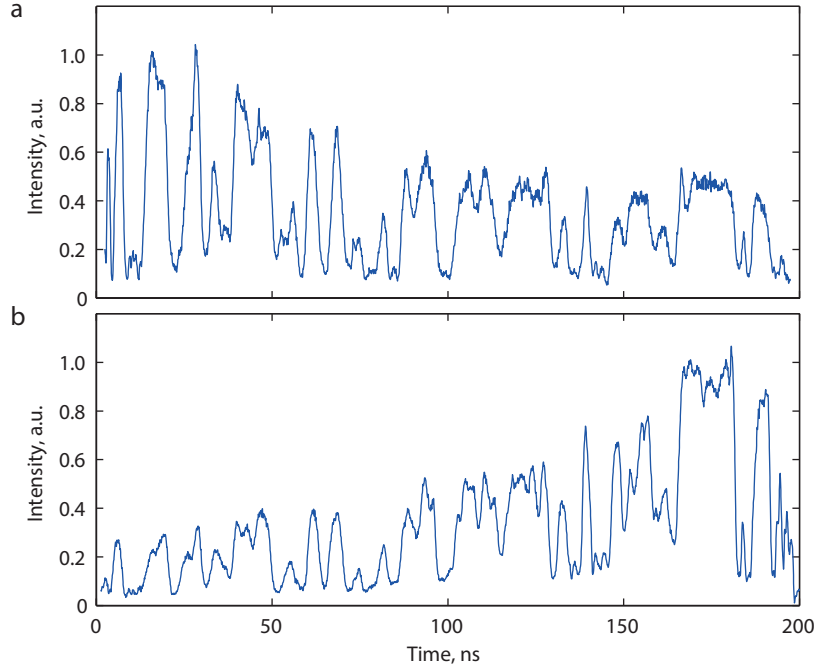
Figure 5.7: Reflection for two 350 ps pulses separated by 3 ns for direct (top) and reversed (bottom) fibre connection. The signal for the reversed fibre connection was reflected horizontally for a better comparison.

In fact, this interference pattern of the two pulse reflection can be used to determine the birefringence variation along the fibre. To do that the reflections was measured while varying the probe wave frequency for the minimum available pulse separation of 2 ns. The results of the measurement are shown on figure 5.8a, where each row corresponds to a trace similar to those on figure 5.7.

It can be seen that as the frequency of the probe changes, the reflection intensity at a given point goes from the maximum value to the minimum and back again. This happens because frequency detuning $\delta\omega$ introduces a change in wave vector mismatch:

$$\delta k = \frac{\delta\omega c}{n}\,, \tag{5.40}$$

which according to equation (5.35) introduces an additional phase mismatch between two reflections:

$$\delta\phi(t, \Delta t_{\mathrm{p}}) = \delta\omega\Delta t_{\mathrm{p}}\,. \tag{5.41}$$

If one tracks the change in $\delta\omega$ along the interference maxima (or minima) it would be equivalent to solving equation $\Delta\phi(t, \Delta t_{\mathrm{p}}) + \delta\phi = \mathrm{const}$ or finding the frequency detun-

a

b
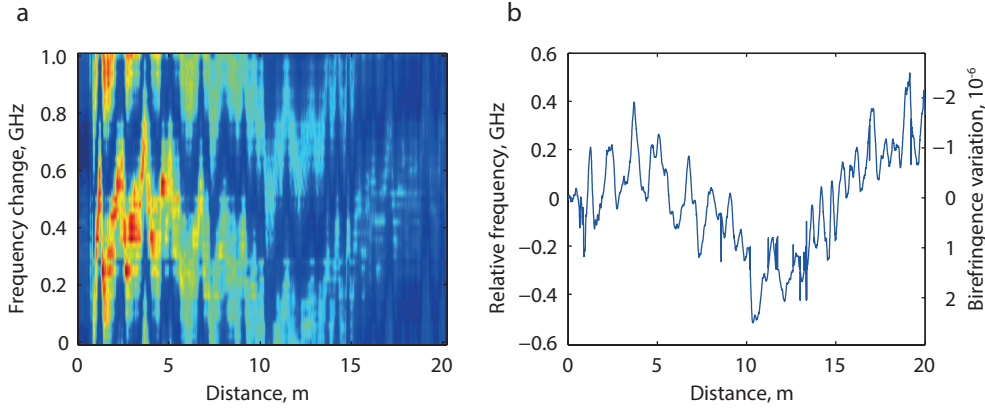
Figure 5.8: Measuring birefringence variation along the 20 m fibre. a) Dependence of reflected signal on frequency change; b) Extracted frequency detuning along the fibre and the corresponding birefringence variation.

ing that compensates for the birefringence variation:

$$\delta\omega(t) = -\frac{2}{\Delta t_{\mathrm{p}}} \int\limits_{\frac{c(t-\Delta t_{\mathrm{p}})}{2n}}^{\frac{ct}{2n}} \Delta k(\xi)\,\mathrm{d}\xi + 2\pi m\,, \tag{5.42}$$

where m is an integer number. It can be easily seen that the integral term corresponds to the average wave vector mismatch within the pulse separation. The change in the wave vector mismatch can be linked to the change of fibre's birefringence, allowing us to know how it varies along the fibre.

Fitting all the observable maxima/minima and combining the results it was possible to extract the $\delta\omega$ required to compensate for the birefringence variation along the fibre. It is shown on figure 5.8b along with the corresponding variation of birefringence $(n_x - n_y)/n_x$. The birefringence change of $\pm 2 \times 10^{-6}$ corresponds to a 1 % variation over the average birefringence of 2×10^{-4}. An estimation shows that for an acceptable performance the birefringence uniformity has to be improved tenfold, reducing the variations in the interference intensity down to 1 %.

Due to this strong nonuniformity of the fibre, further experiments were done using a 1 m long fibre – the pigtail of the polarisation combiner – which was found to be uniform enough. A phase modulator was added into the setup in order to change the phase of the second probe pulse by π as shown on figure 5.9. Measurements were done varying the separation between two pulses with and without the phase modulation. With the phase modulation turned off, two reflections arrive in phase showing positive interference (grey
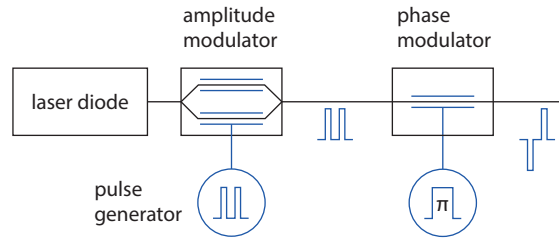
Figure 5.9: Generation of probe pulses with opposite phases
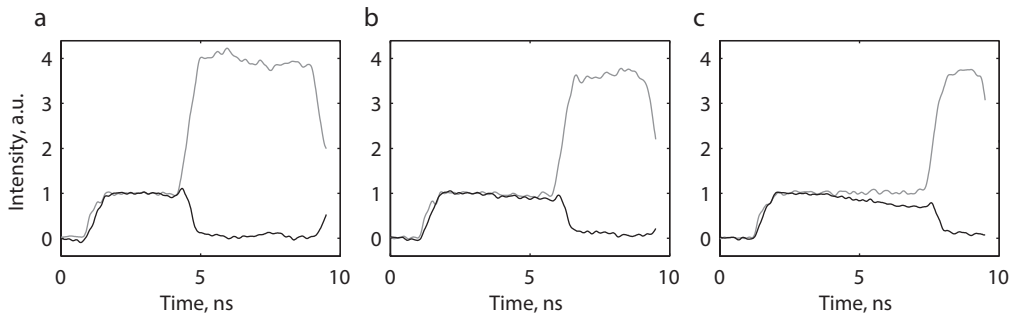
Figure 5.10: Flip-flop (black) and integrator (grey) operation in a 1 m patchcord for a pulse separation of: a) 3.5 ns; b) 5 ns; c) 6.5 ns. The first section of the signal corresponds to the reflection of the first pulse, the second to the destructive or constructive interference of two reflections.

lines on figure 5.10a-c); when the phase of the second pulse is changed by π two reflections arrive with opposite phases and cancel each other, showing the desired flip-flop operation (black lines on figure 5.10a-c)[6].

The previously observed change in phase shift between two reflections due to frequency tuning can be used to switch the system from integrator to flip-flop regime without using the phase modulator. In order to verify it the interference between the two reflections was measured depending on the frequency detuning and the pulse separation; the measurement results for the pulse separation of 2 ns, 4 ns and 7 ns are shown on figure 5.11. Afterwards, the intensity was predicted using equation (5.39). Figure 5.12 shows all the measured data (each row corresponds to a measurement similar to the measurements shown on figure 5.11) as well as the theoretically predicted response. A good match can be seen between the measurement and the modelling, with some discrepancies due to

---

[6]The drop in the flip-flop signal on figure 5.10c was caused by the frequency instability of the used lasers, leading to a change of experimental conditions between the two measurements.
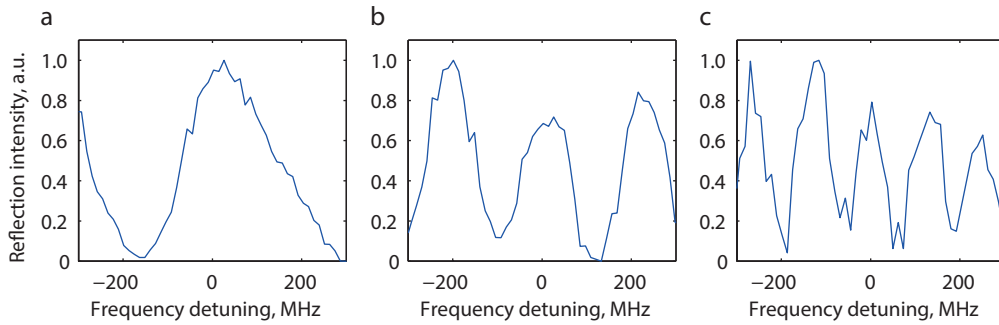
Figure 5.11: Intensity of the interference between two reflections depending on frequency detuning from the BDG peak for pulse separation of 2 ns, 4 ns and 7 ns.
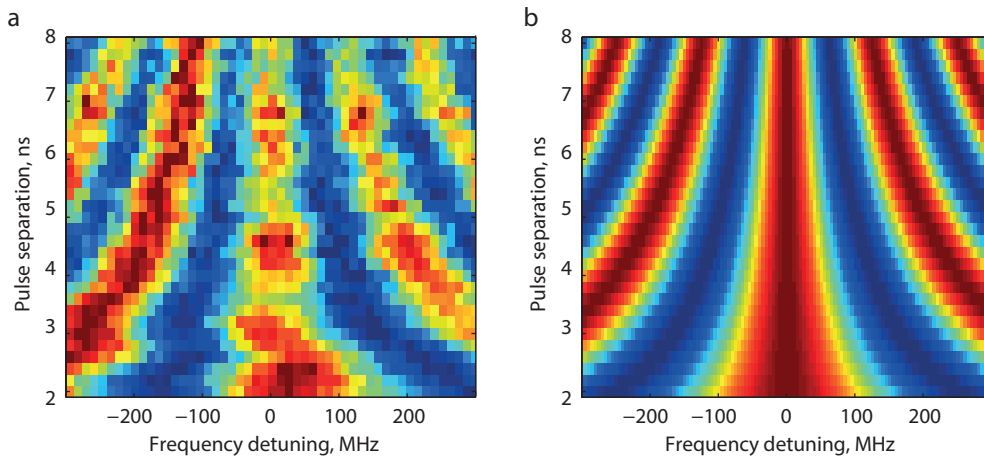
Figure 5.12: a) Measured and b) theoretically predicted reflection intensity depending on the probe's detuning from the peak of the BDG and the time separation between two pulses

the frequency instability of the lasers used in the experiment. It can be clearly seen that the system goes from integrator to the flip-flop operation and back again by simple detuning with the condition of flip-flop operation given by hyperbolas $\Delta\phi = \Delta\omega\Delta t_{\mathrm{p}} = (2m+1)\pi$.

Another way of generating two optical pulses would be splitting the pulse, delaying one copy, and recombining the two – as shown on figure 5.13. During the preliminary experiments it was found that the optical delay line rotates the light polarisation despite having a PM input-output fibre. To compensate for it an SMF optical circulator had to be
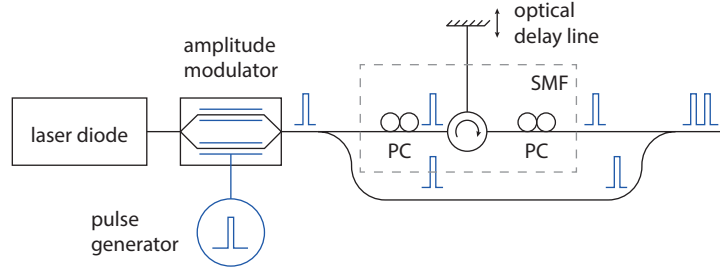
Figure 5.13: Generating two pulses with an optical delay line. The area in the grey rectangular contains a non-PM circulator and two polarisation controllers (PC).

used along with two polarisation controllers.

For this way of generating a double pulse the second probe pulse doesn't have the same complex amplitude as the first one – it contains a phase term given by the temporal delay:

$$A_{\mathrm{pr},2} = A_{\mathrm{pr}} e^{j\omega_{\mathrm{pr}}\Delta t_{\mathrm{p}}} . \tag{5.43}$$

To find the amplitude of the reflected wave we can write the equivalent of equation (5.32):

$$A_{\mathrm{r,sum}} = j g_2 Q^* A_{\mathrm{pr}} \tau \left(e^{j\phi(t)} + e^{j\phi(t-\Delta t_{\mathrm{p}})} e^{j\omega_{\mathrm{pr}}\Delta t_{\mathrm{p}}} \right) . \tag{5.44}$$

Thus, the cosine term in equation (5.34) will be changed to:

$$\cos\left(\frac{\phi(t) - \phi(t-\Delta t_{\mathrm{p}}) - \omega_{\mathrm{pr}}\Delta t_{\mathrm{p}}}{2}\right) = \cos\left(\frac{(\omega_{\mathrm{pr}} - \omega_{\mathrm{gr}})\Delta t_{\mathrm{p}} - \omega_{\mathrm{pr}}\Delta t_{\mathrm{p}}}{2}\right)$$
$$= \cos\left(\frac{\omega_{\mathrm{gr}}\Delta t_{\mathrm{p}}}{2}\right) . \tag{5.45}$$

The sum of the pulses reflections becomes independent on the probe's frequency; at the same time it becomes highly dependent on the pulse separation.

There is an intuitive explanation for the difference in system's behaviour for two methods of double pulse generation. The frequency dependent phase shift between reflections of two pulses originates from time delay between two reflections $\omega_{\mathrm{pr}}\Delta t_{\mathrm{p}}$. When two pulses are generated with a delay line the second pulse gets delayed by Δt_{p} and, therefore, accumulates exactly the same phase shift $\omega_{\mathrm{pr}}\Delta t_{\mathrm{p}}$. These two phase shifts cancel each other making the system (theoretically) independent of the probe's frequency.

Using a tunable optical delay line, the intensity of the double pulse reflection was measured while varying the pulse separation with a 1 fs step; the results of this measurement are shown on figure 5.14a. Oscillations with an average period of approximately
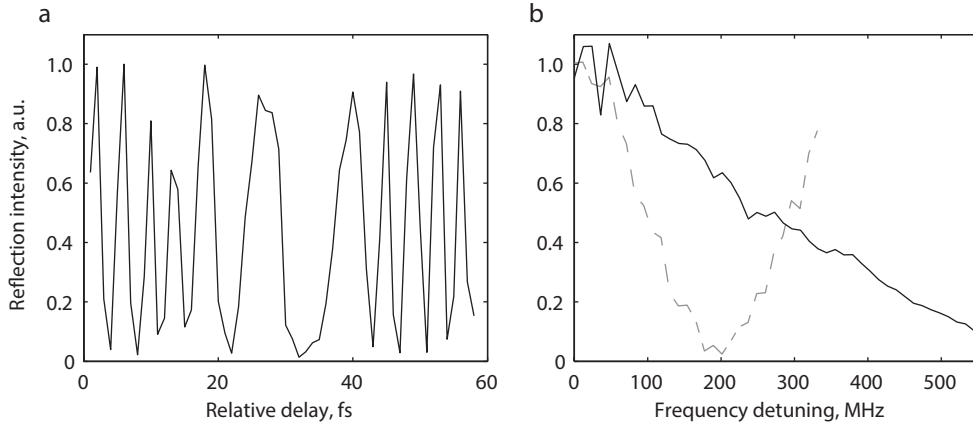
Figure 5.14: Reflection intensity for two pulses generated via an optical delay line depending on a) pulse separation and b) frequency detuning (dashed grey line is the reflection of two electrically generated pulses under the same conditions)

5 fs can be clearly observed, matching the expected value of $1/193\,\text{THz} = 5.2\,\text{fs}$ for the wavelength of 1555 nm. The irregularities in the oscillation shape can be explained by the properties of the delay line, which has the accuracy and the repeatability of 10 fs both.

The frequency of the probe wave was varied to check whether the reflection intensity depends on it. The results are shown on figure 5.14b along with the results obtained for a pair of pulses generated using the double pulse generator. It can be seen the dependence is still observable, though less than for the previous measurement. A possible explanation for this dependence would be a frequency dependency of the pulse separation. The fibre dispersion is not high enough to introduce such a strong dependence – a 2 ns pulse separation corresponds to a 0.4 m difference in optical path; in an optical fibre with the dispersion of $17\,\text{ps}\,\text{km}^{-1}\,\text{nm}^{-1}$ with frequency tuning over 500 MHz it provides a delay of:

$$\delta\Delta t_{\text{p}} = 17\,\text{ps}\,\text{km}^{-1}\,\text{nm}^{-1} \times 0.4\,\text{m} \times 1555\,\text{nm}\,\frac{500\,\text{MHz}}{193\,\text{THz}} \approx 0.03\,\text{fs}, \qquad (5.46)$$

while a delay of 2.5 fs is required to go from the maximum reflection to zero. However, as it was mentioned before, the optical delay line rotates the polarisation, meaning that a combination of x- and y-polarised light can propagate in its PM pigtail. This potentially lead to the part of the pulse being delayed affecting the reflection.

Overall, generation of two pulses directly in an intensity modulator is more attractive – the pulse separation can be changed easily in broad range, without being limited to the delay line range, while the system remains in the flip-flop mode (as long as the probe is tuned to the peak of the BDG).

5.3 Spectral properties of dynamic Brillouin gratings

Brillouin dynamic gratings can be used not only to process signals in time domain but in the spectral domain as well. By changing the wavelength of the pumps it is possible to tune the wavelength of the BDG, same can be done with the spectral shape. This section is dedicated to researching the spectral characteristics of BDG's and finding possible applications for them; for simplicity we are going to consider only uniform gratings.

5.3.1 Reflection spectrum of a BDG

To begin with we need to find the expected reflection spectrum of a uniform grating, the starting point for it is equation (5.25) rewritten for $z_0 = 0$:

$$A_{\mathrm{r}}(0) = jg_2 Q^* A_{\mathrm{pr}} \int_0^L \exp\left(j \int_0^\xi 2\Delta k(\zeta)\,\mathrm{d}\zeta \right) \mathrm{d}\xi\,. \tag{5.47}$$

For a uniform grating it is easy to solve:

$$
\begin{aligned}
A_{\mathrm{r}}(0) &= jg_2 Q^* A_{\mathrm{pr}} \int_0^L \exp(j2\Delta k\xi)\,\mathrm{d}\xi \\
&= jg_2 Q^* A_{\mathrm{pr}} \frac{\exp(j2\Delta kL) - 1}{j2\Delta k} \\
&= jg_2 Q^* A_{\mathrm{pr}} e^{j\Delta kL} \frac{e^{j\Delta kL} - e^{-j\Delta kL}}{j2\Delta k} \\
&= jg_2 Q^* A_{\mathrm{pr}} e^{j\Delta kL} \operatorname{sinc}(\Delta kL)L\,.
\end{aligned}
\tag{5.48}
$$

It can be rewritten for the intensity, using equation (5.5) for the acoustic wave amplitude:

$$I_{\mathrm{r}} = \frac{g_1^2 g_2^2}{|\Gamma_{\mathrm{A}}|^2} I_{\mathrm{p1}} I_{\mathrm{p2}} I_{\mathrm{pr}} \operatorname{sinc}^2(\Delta kL)L^2\,. \tag{5.49}$$

Reflection from a BDG was measured while varying the probe frequency. The resulting reflection spectrum is shown on figure 5.15a along with the predicted sinc^2 dependence. The first zero of the sinc function is positioned at 112 MHz which is equivalent to the wave vector mismatch:

$$\Delta k = \frac{2\pi n}{c} 112\,\mathrm{MHz} = 3.38\,\mathrm{m}^{-1}\,. \tag{5.50}$$

Given that for the first zero of sinc function $\Delta kL = \pi$, the expected length of the fibre is equal to 0.93 m which is in a good agreement with the approximately known fibre length of 1 m.

a

b
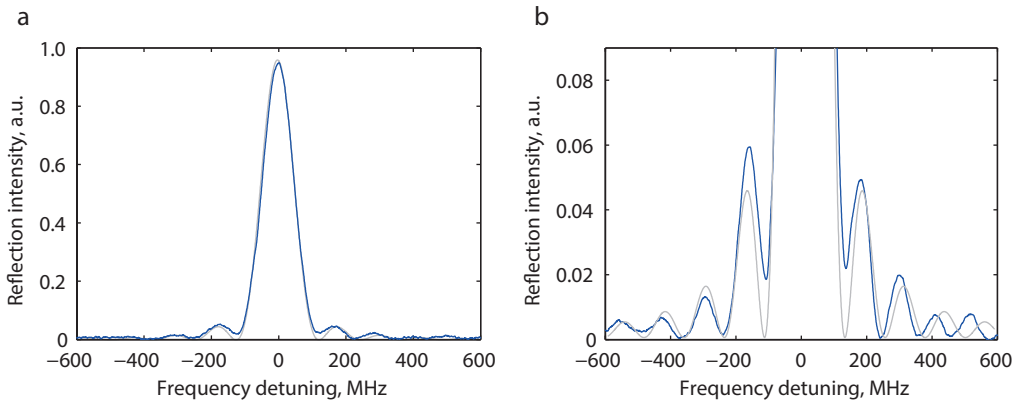
Figure 5.15: Reflection spectrum of a BDG generated in a 1 m long fibre: measured (blue line) and theoretically predicted (grey line)

Figure 5.15b shows a more detailed comparison between the measured and the theoretically predicted reflection spectrum; it is evident on this scale that the predicted spectrum does not match well with the measurement. This distortion can be easily attributed to the nonuniformity of the fibre's birefringence.

5.3.2 Dynamic grating with multiple spectral lines

The next step was to generate a BDG with multiple spectral lines by altering the pump waves. A modulator was positioned right after the laser used to create two pump waves and it was driven by an arbitrary waveform generator (AWG). During the experiment the AWG was set to produce one or several tones, generating side bands in the pump waves spectra.

The first experiment was performed to observe a BDG with well-separated spectral lines; a line separation of 224 MHz was chosen, corresponding to the second zero of the sinc-shaped reflection spectrum. Three measurements were performed: without modulating the pump, modulating it with a single 224 MHz tone (three spectral lines, including the carrier), and with a double-tone modulation with 224 MHz and 448 MHz (five spectral lines). Measured reflection spectra are shown on figure 5.16a–c. The multiple reflection lines are separated well enough not to interact with each other and their intensities are fairly uniform (less than 5 % variation).

One thing to be noted is that the reflection of each line decreases quadratically with the number of lines, it can be seen that in comparison to a single line (figure 5.16a) the reflection of each line is approximately 9 times lower for three lines (figure 5.16b) and 25 times for five (figure 5.16a–b). This can be easily explained: first, the EDFA's used to

Figure 5.16: Reflection spectrum of a BDG created with pumps consisting of a) single spectral line; b) three lines with 224 MHz spacing; c) five lines with 224 MHz spacing

amplify pump waves work in saturation, i.e. their output power is constant. This power is spread over multiple spectral lines, meaning that the power of each is inversely 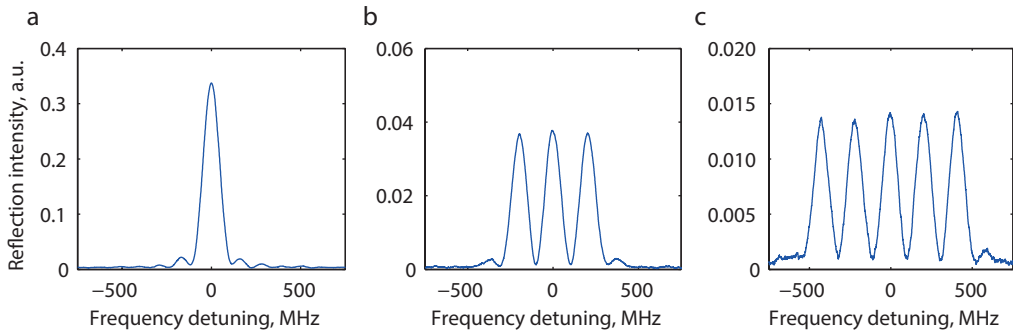proportional to the number of lines. Second, by looking at equation (5.49) for the reflection intensity we can see that it is proportional to the product of intensities of pump waves, therefore reflection intensity from each spectral line of the grating is inversely proportional to the square of the number of lines.

The next step was to decrease the separation between the spectral lines, combining them into a rectangular filter. The first experiment was done modulating the pumps with a single 112 MHz tone, corresponding to the first zero of the sinc-shaped spectrum of each grating. Figure 5.17a shows the resulting reflection spectrum; it is far from being uniform and symmetric. The central part consists of three overlapping lines which separation does not correspond to 112 MHz due to the manner the sinc-shaped spectra interfere with each other; the same interference produces strong side-lobes. The asymmetry of the spectrum originates from the asymmetry of each line's sinc-spectrum. It should be noted that the shape of the reflection spectrum highly depends on the separation between spectral lines; for example, for the separation of 108 MHz a fairly good reflection spectrum was observed, with a relatively flat top and suppressed side-lobes.

The experiment was repeated for pumps containing seven spectral lines; reflection spectrum was observed while varying the separation between spectral lines, and for the value of 110 MHz a fairly rectangular reflection with a single pair of side-bands was observed (figure 5.18a). Once again, the reflection spectrum strongly depended on the spectral separation – a change of 1 MHz in line separation completely distorted the spectrum (figure 5.18b). Note that four equidistant spectral lines are observed despite an odd (seven) number of spectral lines in the pump spectra. This further signifies the fact that combining multiple lines together is not an easy task and a further research has to be done to find a reliable way of getting a good reflection spectrum.
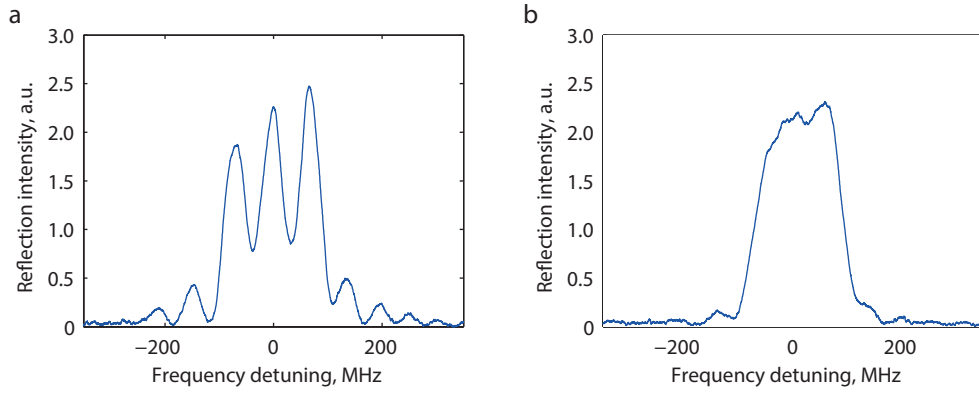
84

Figure 5.17: Reflection spectrum of a BDG created with pumps consisting of three lines with spacing of a) 112 MHz; b) 108 MHz
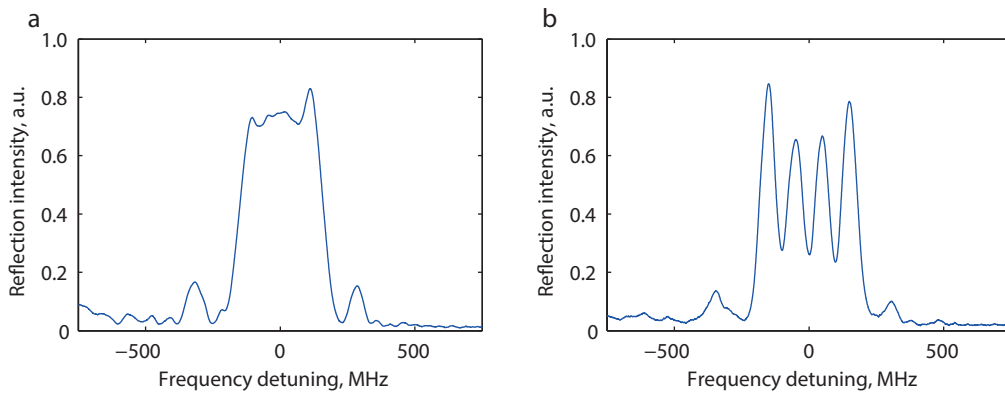
Figure 5.18: Reflection spectrum of a BDG created with pumps consisting of seven lines with spacing of a) 110 MHz; b) 109 MHz
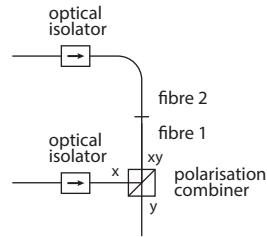
Figure 5.19: Fibre configuration used in the experiment

5.3.3 Dynamic gratings in multiple fibres

A potential problem may arise while conducting experiments with an experimental setup consisting of several fibre types. In all the previous experiments the output pigtail of the polarisation combiner was used as a 1 m long medium for BDG. However, it is followed by the pigtail of an optical isolator which can potentially be made of a different fibre. These fibres will be called *fibre 1* and *fibre 2* as shown on figure 5.19.

Indeed, once the frequency tuning range was expanded we could observe a second BDG, generated in fibre 2, as seen on figure 5.20a. The difference between resonant frequencies of two BDG's is equal to 2 GHz, which corresponds to a 5 % difference in bire-fringence between the two fibres. When pump waves with broad spectra are used, the spectra of two BDG can get even closer as on figure 5.20b where pump waves consist of three lines separated by 400 MHz. For a smaller difference in birefringence, or broader pump spectra, the two gratings may start overlapping making reflections from them interfere.

A fairly simple solution to this problem has been proposed – to rotate the fibre used as a BDG medium by 90°, swapping the x- and the y-axes. This transformation changes the sign of the birefringence, positioning the resonant frequency of the BDG on the other side of the pump line. A section of a PM fibre was spliced rotated by 90° and the reflection spectrum was measured for the BDG's generated inside this fibre. Figure 5.21 shows the obtained spectrum (black line) and the previously obtained spectrum from the polarisation combiner's pigtail (grey line). We can see that the reflection peak of the BDG in the rotated fibre is positioned on the other side of the pump line isolating it from the influence of BDG's generated in other, normally aligned fibres. We can also see that the frequency separation between the pump and the BDG is different for two fibres due to different birefringence values.
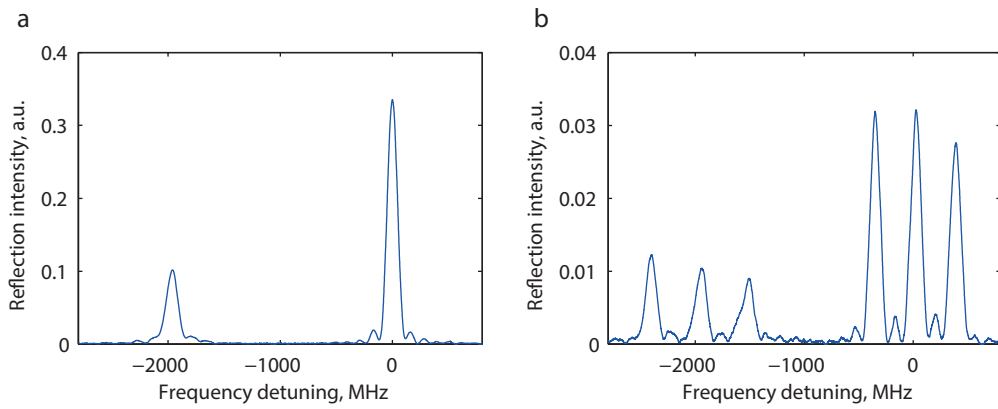
Figure 5.20: Reflection spectrum of BDG's generated in two consecutive fibres with pumps consisting of a) single spectral line; b) three lines with 400 MHz spacing
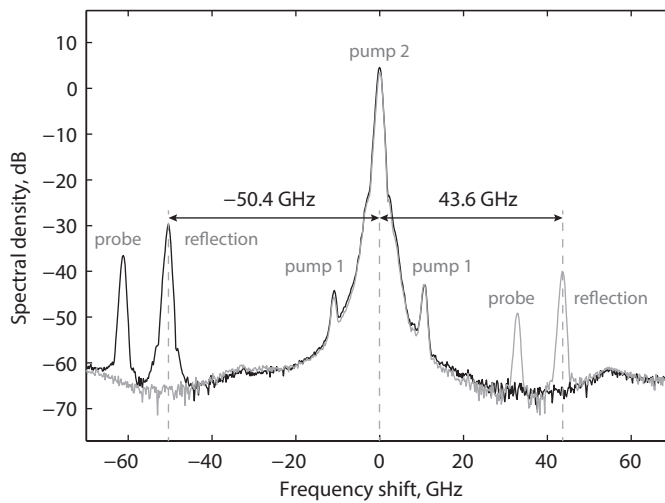
Figure 5.21: Reflection spectra for BDG generated in normal fibre (grey line) and a fibre spliced with a 90° rotation (black line)

87

5.4 Discussion

The theoretical model of Brillouin dynamic gratings presented in section 5.1 and expanded in following sections is experimentally verified. It means that the simplification of non-dispersive medium (leading to equality between the phase and group refractive index) holds under the experimental conditions. The presented model can be used to predict properties of Brillouin dynamic gratings and behaviour of systems that utilise them, making it easier to design further experiments.

Section 5.2 presents an all-optical flip-flop based on a 1 m long BDG, which corresponds to a maximum storage time of 10 ns showing that the application BDG's in this area is promising. The 1 m limitation is given by the birefringence uniformity in available PM fibres; and with a tenfold improvement in uniformity the distance can be extended to tens or even hundreds of metres. This will open a possibility to flip-flop operation over hundreds of nanoseconds or even several microseconds.

Section 5.3 dedicated to the spectral properties of BDG's shows that the spectrum of a dynamic grating can be manipulated by changing the spectra of pump waves. It is experimentally demonstrated that dynamic gratings with multiple spectral lines can be created by simply modulating pump waves with single or multiple tones. This allows for creation of dynamically tuned optical filters (or microwave filters, since a microwave signal can be carried by an optical wave). At the same time, creating a BDG with a broad flat spectrum proves to be a more difficult task due to the interference between spectra of each grating. The presented results are merely a preliminary work; further research activities are required to study the spectral properties of BDG's in detail, create a model that allows for designing of optical filters, and to apply this knowledge in practice to create arbitrarily shaped filters.

Conclusions and perspectives

Looking back at years of research it is possible to see which activities were fruitful and which became a dead end, even if attracting a lot of attention at early stages. Without having the power of hindsight, looking forward and trying to determine which directions should be taken in future is a risky task. Still, I am going to make an attempt in it and show my view on the future of Brillouin dynamic gratings research by extrapolating my personal experience. I will begin with sensing applications.

Observations show that since 2008 the number of points in state-of-the-are Brillouin sensors has doubled on average every 1.5 years, figure C.1 shows this evolution. Highlighted points correspond to the results obtained during this thesis – phase-correlation technique quickly overcame other techniques in term on the number of resolved points, setting one record after another.
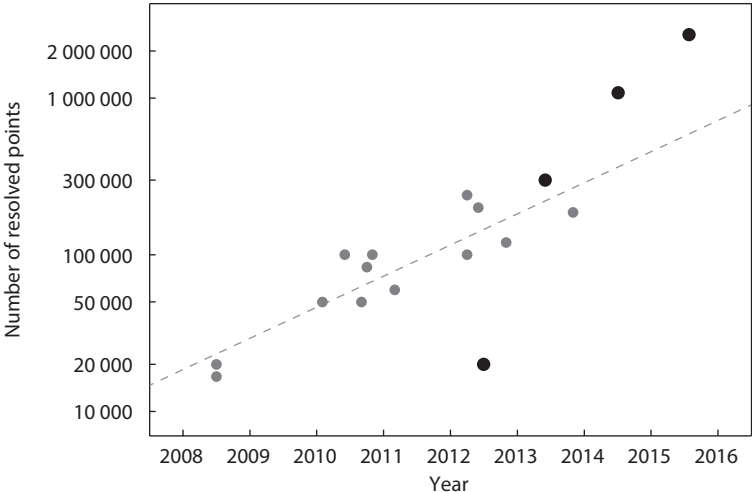

Figure C.1: Growth of the number of points measured by distributed Brillouin fibre sensors. Highlighted are the results obtained during this thesis.

A further increase in the number of resolved points is going to be difficult. When it comes to the distance, a two-fold increase from 17.5 km to 35 km would reduce the signal-to-noise ratio (SNR) by 7 dB which has to be somehow compensated for. On a bright side, any technique applicable to classic BOTDA setups can be readily applied to time-gated phase-correlation technique: e.g. Raman amplification and intensity pulse coding. The latter was already shown to be effective [60] – a 1112 bits long code allowed for a measurement over a 2.2 km long fibre with 2 cm resolution with the measurement time of 25 s (assuming zero latency of equipment).

Improving the spatial resolution is not an easier task. High spatial resolution requires pump and signal waves to have broad spectra which makes it impossible to separate them in detection without introducing significant distortion and, thus, decreasing the signal-to-noise ratio. It means that while improving the spatial resolution is possible [61] it will be hardly possible to improve the number of points this way.

At this stage a more desirable direction of improvement would be the measurement time. In its current state the demonstrated setup would require 14 hours to address all the 2 100 000 points (assuming zero latency of equipment). Even though for a given distance the measurement time scales cubically with the number of resolved points, a measurement of "just" 1 000 000 points would still require 1.5 hours. However, unlike sensing distance, measurement time scales quadratically with SNR. The above-mentioned 7 dB (5 times) improvement in SNR, required to double the sensing distance, can be used instead to speed up the measurement by a factor 25.

Even with a short measurement time, presently there is not much potential application for high spatial resolution sensing at these distances outside of the lab environment. There is a demand in oil industry for sensors with sensing range of 5–10 km with the spatial resolution of 10–20 cm. Yet, even at short distances this technique would be too expensive and complicated to be economically feasible, meaning that it will not leave the lab in near future, if ever. Meanwhile it will remain a very useful tool for a detailed measurement of Brillouin scattering properties of new devices, e.g. tapered fibres or microwires.

As for BDG's in polarisation maintaining fibres, one of the limiting factors for their application is the non-uniformity of fibres' birefringence. For most of the applications of PM fibres this uniformity is not important (as long as the linear polarisation is preserved along the fibre), that's why it is not necessary for fibre manufacturers to control this parameter. Improving the birefringence uniformity by one order of magnitude would make it possible to use BDG's of tens of metres long to create all optical flip-flops with storage time of hundreds of nanoseconds. Achieving this level of uniformity would require modelling of processes involved during the fibre cooling and a strong cooperation with fibre manufacturers. Objectively, I have to admit that creation of a bulk flip-flop system will not justify this amount of work; especially since it can be potentially replaced by a miniature silicon-on-chip device.

On the other hand, manipulating the spectrum of a dynamic grating is something that should be researched deeper as this application does not require long fibres. BDG's with arbitrary spectra can be used for filtering of optical signals, microwave photonics applications, or dispersion compensation (since the properties of dynamic gratings depend on the phases of the waves that generate them).

Lately, very impressive results were obtained, showing how Brillouin scattering efficiency is drastically increased in nanoscale silicon wires [64–67] (once can also read two overviews of the work done in this field [68, 69]). These results show an at least three order of magnitude improvement in linear Brillouin gain in comparison with optical fibres. It means that several metres of an optical fibre can be potentially replaced with an optical nanowire with a length of several millimetres. Brillouin dynamic gratings have been already demonstrated in a photonic chip with a 4 µm width [70], opening the door for further work.

In conclusion, there is a lot of research to be done in Brillouin dynamic gratings field. This technique is 7 years old with only a handful of research groups working on it. As it was shown in this work, generation and read-out of BDG's can be modelled matching experimentally obtained results, meaning that feasibility of new ideas can be checked numerically before proceeding with experimental work.

Appendix A

Correlation peak shape derivation

In order to find the force driving the acoustic wave in phase-correlated sensing technique one has to find the time average term in the right part of equation (2.10):

$$p_{\text{st}} \propto \left\langle e^{j\pi[f_{\text{PRBS}}(t+t_{\text{p}}(z))-f_{\text{PRBS}}(t+t_{\text{s}}(z))]} \right\rangle . \tag{A.1}$$

In order to do that it is necessary to find the behaviour of the differential term of the exponent's argument:

$$f_{\text{PRBS}}\left(t + t_{\text{p}}(z)\right) - f_{\text{PRBS}}\left(t + t_{\text{s}}(z)\right) , \tag{A.2}$$

or, making a substitution $t + t_{\text{p}}(z) \longrightarrow t$ and $t_{\text{s}}(z) - t_{\text{p}}(z) \longrightarrow \Delta t$:

$$f_{\text{PRBS}}\left(t\right) - f_{\text{PRBS}}\left(t + \Delta t\right) . \tag{A.3}$$

Let's remember definitions of $\Pi\left(t\right)$ and $f_{\text{PRBS}}\left(t\right)$ given by equations (2.1) and (2.2)

$$\Pi\left(t\right) = \begin{cases} 0 & |t| > 1/2 \\ 1/2 & |t| = 1/2 \\ 1 & |t| < 1/2 \end{cases} , \tag{A.4}$$

$$f_{\text{PRBS}}\left(t\right) = \sum_q \xi_q \Pi\left((t - qT_{\text{bit}})/T_{\text{bit}}\right) , \tag{A.5}$$

Let's rewrite equation (A.2) using the definition of f_{PRBS}:

$$\begin{aligned}
f_{\text{PRBS}}\left(t\right) - f_{\text{PRBS}}\left(t + \Delta t\right) &= \sum_q \xi_q \, \Pi\left((t - qT_{\text{bit}})/T_{\text{bit}}\right) \\
&\quad - \sum_q \xi_q \, \Pi\left((t - qT_{\text{bit}} + \Delta t)/T_{\text{bit}}\right) .
\end{aligned} \tag{A.6}$$

93

We can separate Δt into an integer number of T_{bit} and the remainder:

$$\Delta t = (k + \alpha)T_{\text{bit}} , \tag{A.7}$$

where k is an integer number and $\alpha \in [0, 1)$. Using this definition and making a substitution $\tau = t/T_{\text{bit}}$ one can rewrite equation (A.6):

$$f_{\text{PRBS}}(t) - f_{\text{PRBS}}(t + \Delta t) = \sum_q \xi_q \Pi(\tau - q) - \sum_q \xi_q \Pi(\tau - q + k + \alpha) . \tag{A.8}$$

It is easy to see that $\sum_q \xi_q \Pi(\tau - q + k + \alpha) = \sum_q \xi_{q+k} \Pi(\tau - q + \alpha)$, thus we can write:

$$\sum_q \xi_q \Pi(\tau - q) - \sum_q \xi_q \Pi(\tau - q + k + \alpha)$$
$$= \sum_q \xi_q \Pi(\tau - q) - \sum_q \xi_{q+k} \Pi(\tau - q + \alpha) . \tag{A.9}$$

Using equation (A.4) – the definition of the rectangular function – one can calculate $\xi_q \Pi(\tau - q) - \xi_{q+k} \Pi(\tau - q + \alpha)$ (see figure A.1 for the explanation):

$$\xi_q \Pi(\tau - q) - \xi_{q+k} \Pi(\tau - q + \alpha) = \begin{cases} 0 & \tau < q + 1/2 - \alpha, \tau > q + 1/2 \\ -\xi_{q+k} & \tau \in (q - 1/2 - \alpha, q - 1/2) \\ \xi_q - \xi_{q+k} & \tau \in (q - \alpha, q + 1/2 - \alpha) \\ \xi_q & \tau \in (q + 1/2 - \alpha, q + 1/2) \end{cases} . \tag{A.10}$$

Note that $1/2$ values of rectangular function at its edges are ignored as they will not matter once the final answer is integrated to find the average value. Three nonzero terms can be written in form of rectangular functions:

$$\xi_q \Pi(\tau - q) - \xi_{q+k} \Pi(\tau - q + \alpha) = (\xi_q - \xi_{q+k}) \Pi\left(\frac{\tau - q - \alpha/2}{1 - \alpha}\right)$$
$$+ \xi_q \Pi\left(\frac{\tau - q + \alpha/2 - 1/2}{\alpha}\right) - \xi_{q+k} \Pi\left(\frac{\tau - q + \alpha/2 + 1/2}{\alpha}\right) . \tag{A.11}$$

Note that in special case of $\alpha = 0$ two last terms disappear, as they would represent rectangular functions with zero width. For nonzero α they can be combined together:

$$\xi_q \Pi\left(\frac{\tau - q + \alpha/2 - 1/2}{\alpha}\right) - \xi_{q+k} \Pi\left(\frac{\tau - q + \alpha/2 + 1/2}{\alpha}\right)$$
$$= \xi_{q-1} \Pi\left(\frac{\tau - q + \alpha/2 + 1/2}{\alpha}\right) - \xi_{q+k} \Pi\left(\frac{\tau - q + \alpha/2 + 1/2}{\alpha}\right)$$
$$= (\xi_{q-1} - \xi_{q+k}) \Pi\left(\frac{\tau - q + \alpha/2 + 1/2}{\alpha}\right) . \tag{A.12}$$
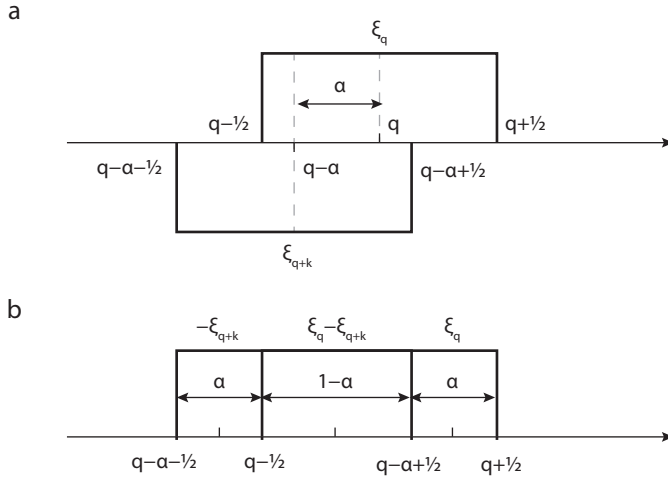
Figure A.1: Subtraction of two rectangular functions positioned at q and $q - \alpha$ with amplitudes ξ_q and ξ_{q+k} respectively. a) Two rectangular functions; b) Resulting difference as three rectangular functions.

Leading to to the final equation for the phase difference:

$$f_{\mathrm{PRBS}}(t) - f_{\mathrm{PRBS}}(t + (k + \alpha)T_{\mathrm{bit}})$$
$$= \sum_q (\xi_q - \xi_{q+k}) \Pi\left(\frac{\tau - q - \alpha/2}{1 - \alpha}\right) + \sum_q (\xi_{q-1} - \xi_{q+k}) \Pi\left(\frac{\tau - q + \alpha/2 + 1/2}{\alpha}\right). \quad (A.13)$$

Two sums represent two sets of rectangular functions interleaved with each other as shown on figure A.2. Since ξ_q is a pseudo-random sequence, two items ξ_q and ξ_{q+k} are completely uncorrelated with each other unless $k = mN_{\mathrm{bits}}$, an integer number of PRBS lengths:

$$\xi_q - \xi_{q+k} = \begin{cases} 0 & k = mN_{\mathrm{bits}}, m \in \mathbb{Z} \\ \mathrm{rand}\{0, \pm 1\} & \text{otherwise} \end{cases}, \quad (A.14)$$

or, once used as an argument of a complex exponential function:

$$e^{j\pi(\xi_q - \xi_{q+k})} = \begin{cases} 1 & k = mN_{\mathrm{bits}}, m \in \mathbb{Z} \\ \mathrm{rand}\{-1, 1\} & \text{otherwise} \end{cases}. \quad (A.15)$$

It means that outside of the correlation peak, forces that drive the acoustic wave average out to zero. Let's find how they behave within the correlation peak. Note, that two cases in equation (A.13) correspond to the correlation peak: $k = mN_{\mathrm{bits}}$ for the first sum
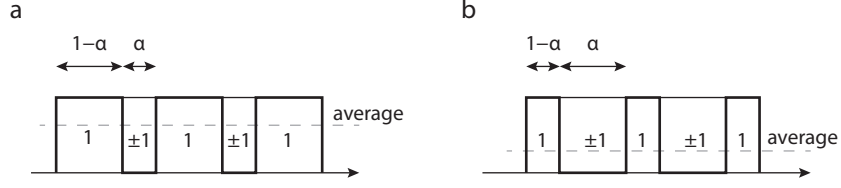
Figure A.2: Force driving an acoustic wave within a correlation peak for two values of α. Note that the average value of the force decreases
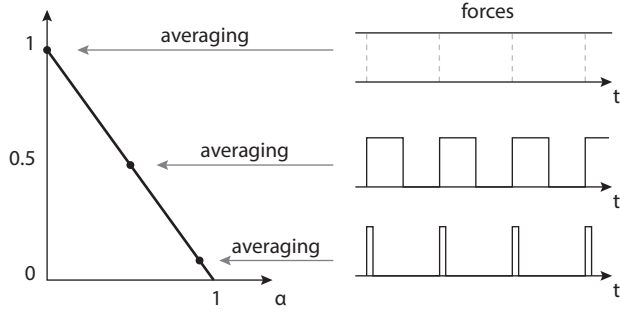
Figure A.3: Averaged force depending on distance from the correlation peak centre

and $k = mN_{\text{bits}} - 1$ for the second. The two represent two sides of the correlation peak, thus we can consider only the first one, knowing that the second one will give a symmetric solution.

Let's rewrite the term to be averaged in equation (A.1) using equations (A.13) and (A.15):

$$e^{j\pi[f_{\text{PRBS}}(t+t_{\text{p}}(z)) - f_{\text{PRBS}}(t+t_{\text{s}}(z))]}$$

$$= \exp\left(j\pi\left[\sum_q (\xi_q - \xi_{q+k})\,\Pi\left(\frac{\tau - q - \alpha/2}{1-\alpha}\right)\right.\right.$$

$$\left.\left. + \sum_q (\xi_{q-1} - \xi_{q+k})\,\Pi\left(\frac{\tau - q + \alpha/2 + 1/2}{\alpha}\right)\right]\right). \quad \text{(A.16)}$$

Figure A.2 shows how it behaves in time for two values of α, along with the averaged value. We can see that the average value of this term is given the average of the rectangular pulse train and it is equal to $1 - \alpha$ (see figure A.3) which gives a triangular shape of correlation peak.

96

Appendix B

Solving the differential equation for dynamic grating reflection

Solving equation (5.24) for reflection from a Brillouin dynamic grating is pretty straight-forward. Starting with the original equation:

$$j\Delta k(z)A_{\mathrm{r}}(z) + \frac{\partial A_{\mathrm{r}}(z)}{\partial z} = -jg_2 Q^* A_{\mathrm{pr}} \exp\left(j\int_{z_0}^{z} \Delta k(\xi)\,\mathrm{d}\xi\right), \qquad \text{(B.1)}$$

using the following substitutions:

$$\mathrm{f}(z) = j\Delta k(z)\,, \qquad \text{(B.2)}$$

$$\mathrm{g}(z) = j\int_{z_0}^{z} \Delta k(\xi)\,\mathrm{d}\xi\,, \qquad \text{(B.3)}$$

$$c = -jg_2 Q^* A_{\mathrm{pr}}\,, \qquad \text{(B.4)}$$

we can rewrite the original equation:

$$\mathrm{f}(z)A_{\mathrm{r}}(z) + \frac{\partial A_{\mathrm{r}}(z)}{\partial z} = c\exp(\mathrm{g}(z))\,. \qquad \text{(B.5)}$$

Let's multiply both sides by $\exp\left(\int \mathrm{f}(z)\,\mathrm{d}z\right)$:

$$\left[\mathrm{f}(z)\exp\left(\int \mathrm{f}(z)\,\mathrm{d}z\right)\right]A_{\mathrm{r}}(z) + \exp\left(\int \mathrm{f}(z)\,\mathrm{d}z\right)\frac{\partial A_{\mathrm{r}}(z)}{\partial z}$$
$$= c\exp\left(\mathrm{g}(z) + \int \mathrm{f}(z)\,\mathrm{d}z\right). \quad \text{(B.6)}$$

Making a substitution:

$$\mathrm{f}(z)\exp\left(\int \mathrm{f}(z)\,\mathrm{d}z\right) = \frac{\mathrm{d}}{\mathrm{d}z}\left[\exp\left(\int \mathrm{f}(z)\,\mathrm{d}z\right)\right], \tag{B.7}$$

equation (B.6) will become:

$$\frac{\mathrm{d}}{\mathrm{d}z}\left[\exp\left(\int \mathrm{f}(z)\,\mathrm{d}z\right)\right]A_\mathrm{r}(z) + \exp\left(\int \mathrm{f}(z)\,\mathrm{d}z\right)\frac{\partial A_\mathrm{r}(z)}{\partial z}$$
$$= c\exp\left(\mathrm{g}(z) + \int \mathrm{f}(z)\,\mathrm{d}z\right). \tag{B.8}$$

Applying the reverse product rule $\alpha\frac{\mathrm{d}\beta}{\mathrm{d}z} + \beta\frac{\mathrm{d}\alpha}{\mathrm{d}z} = \frac{\mathrm{d}}{\mathrm{d}z}(\alpha\beta)$:

$$\frac{\mathrm{d}}{\mathrm{d}z}\left[\exp\left(\int \mathrm{f}(z)\,\mathrm{d}z\right)A_\mathrm{r}(z)\right] = c\exp\left(\mathrm{g}(z) + \int \mathrm{f}(z)\,\mathrm{d}z\right). \tag{B.9}$$

Let's introduce the integral of $\mathrm{f}(z)$:

$$\int \mathrm{f}(z)\,\mathrm{d}z = \mathrm{F}(z) + k_1, \tag{B.10}$$

and integrate equation (B.9) from z_0 to $z_0 + L$, where L is the length of the grating:

$$\int_{z_0}^{z_0+L} \frac{\mathrm{d}}{\mathrm{d}z}\left[e^{\mathrm{F}(z)+k_1}A_\mathrm{r}(z)\right]\mathrm{d}z = \int_{z_0}^{z_0+L} c e^{\mathrm{g}(z)+\mathrm{F}(z)+k_1}\,\mathrm{d}z, \tag{B.11}$$

$$e^{\mathrm{F}(z_0+L)+k_1}A_\mathrm{r}(z_0 + L) - e^{\mathrm{F}(z_0)+k_1}A_\mathrm{r}(z_0) = \int_{z_0}^{z_0+L} c e^{\mathrm{g}(z)+\mathrm{F}(z)+k_1}\,\mathrm{d}z. \tag{B.12}$$

Considering that reflected signal is nonexistent at the end of the grating $A_\mathrm{r}(z_0 + L) = 0$:

$$e^{\mathrm{F}(z_0)+k_1}A_\mathrm{r}(z_0) = -\int_{z_0}^{z_0+L} c e^{\mathrm{g}(z)+\mathrm{F}(\xi)+k_1}\,\mathrm{d}z. \tag{B.13}$$

We can rewrite equation (B.10) for F in form of a definite integral:

$$\mathrm{F}(z) - \mathrm{F}(z_0) = \int_{z_0}^{z} j\Delta k(z)\,\mathrm{d}z. \tag{B.14}$$

Function $F(z)$ represents the phase shift accumulated while propagating along the grating. Since at the beginning of the grating phase shift $F(z_0)$ is equal to zero:

$$F(z) = \int_{z_0}^{z} j\Delta k(\xi)\,\mathrm{d}\xi\,, \tag{B.15}$$

exactly the same as equation (B.3) for g. This allows for rewriting equation (B.13):

$$A_\mathrm{r}(z_0) = -\int_{z_0}^{z_0+L} c e^{2\,\mathrm{g}(z)}\,\mathrm{d}z\,. \tag{B.16}$$

Reverting back to original variables given by equations (B.2)–(B.4) the final solution is obtained:

$$A_\mathrm{r}(z_0) = jg_2 Q^* A_\mathrm{pr} \int_{z_0}^{z_0+L} \exp\left(j \int_{z_0}^{z} 2\Delta k(\xi)\,\mathrm{d}\xi \right) \mathrm{d}z\,. \tag{B.17}$$

Bibliography

[1]   Y. Song, S. Havstad, D. Starodubov, Y. Xie, A. Willner, and J. Feinberg, "40-nm-wide tunable fiber ring laser with single-mode operation using a highly stretchable FBG", *IEEE Photon. Technol. Lett.*, vol. 13, no. 11, pp. 1167–1169, 2001.

[2]   C. Goh, M. Mokhtar, S. Butler, S. Set, K. Kikuchi, and M. Ibsen, "Wavelength tuning of fiber Bragg gratings over 90 nm using a simple tuning package", *IEEE Photon. Technol. Lett.*, vol. 15, no. 4, pp. 557–559, 2003.

[3]   R. Kashyap, *Fiber Bragg Gratings*. Academic Press, 1999, 480 pp.

[4]   A. Zadok, Y. Antman, N. Primerov, A. Denisov, J. Sancho, and L. Thevenaz, "Random-access distributed fiber sensing", *Laser & Photon. Rev.*, vol. 6, no. 5, pp. L1–L5, 2012.

[5]   K. Y. Song, S. Chin, N. Primerov, and L. Thévenaz, "Time-domain distributed fiber sensor with 1 cm spatial resolution based on Brillouin dynamic grating", *J. Lightwave Technol.*, vol. 28, no. 14, pp. 2062–2067, 2010.

[6]   J. Sancho, N. Primerov, S. Chin, Y. Antman, A. Zadok, S. Sales, and L. Thévenaz, "Tunable and reconfigurable multi-tap microwave photonic filter based on dynamic Brillouin gratings in fibers", *Opt. Express*, vol. 20, no. 6, p. 6157, 2012.

[7]   N. Primerov, S. Chin, L. Thévenaz, L. Ursini, and M. Santagiustina, "All-optical calculus based on dynamic Brillouin grating reflectors in optical fibers", in *Slow and Fast Light*, OSA, 2011, SLMA3.

[8]   S. Chin, N. Primerov, K. Y. Song, L. Thevenaz, M. Santagiustina, and L. Ursini, "True time reversal via dynamic Brillouin gratings in polarization maintaining fibers", in *Nonlinear Photonics 2010*, OSA, 2010, NThA6.

[9]   S. Chin, N. Primerov, S. Sales, and L. Thévenaz, "Tunable multiplication of the repetition rate of an optical pulse train using dynamic Brillouin gratings in optical fibers", in *CLEO/Europe and EQEC 2011 Conference Digest*, OSA, 2011, CD_P8.

[10]   T. Horiguchi and M. Tateda, "BOTDA-nondestructive measurement of single-mode optical fiber attenuation characteristics using Brillouin interaction: Theory", *J. Lightwave Technol.*, vol. 7, no. 8, pp. 1170–1176, 1989.

[11]   F. Rodriguez-Barrios, S. Martin-Lopez, A. Carrasco-Sanz, P. Corredera, J. Ania-Castanon, L. Thevenaz, and M. Gonzalez-Herraez, "Distributed Brillouin fiber sensor assisted by first-order Raman amplification", *J. Lightwave Technol.*, vol. 28, no. 15, pp. 2162–2172, 2010.

[12]   S. Martin-Lopez, M. Alcon-Camas, F. Rodriguez, P. Corredera, J. D. Ania-Castañon, L. Thévenaz, and M. Gonzalez-Herraez, "Brillouin optical time-domain analysis assisted by second-order Raman amplification", *Opt. Express*, vol. 18, no. 18, p. 18 769, 2010.

[13]   M. A. Soto, G. Bolognini, and F. Di Pasquale, "Optimization of long-range BOTDA sensors with high resolution using first-order bi-directional Raman amplification", *Opt. Express*, vol. 19, no. 5, p. 4444, 2011.

[14]   X. Angulo-Vinuesa, S. Martin-Lopez, P. Corredera, and M. Gonzalez-Herraez, "Raman-assisted Brillouin optical time-domain analysis with sub-meter resolution over 100 km", *Opt. Express*, vol. 20, no. 11, pp. 12 147–12 154, 2012.

[15]   M. A. Soto, M. Taki, G. Bolognini, and F. Di Pasquale, "Simplex-coded BOTDA sensor over 120-km SMF with 1-m spatial resolution assisted by optimized bidirectional Raman amplification", *IEEE Photon. Technol. Lett.*, vol. 24, no. 20, pp. 1823–1826, 2012.

[16]   M. A. Soto, G. Bolognini, F. Di Pasquale, and L. Thévenaz, "Simplex-coded BOTDA fiber sensor with 1 m spatial resolution over a 50 km range", *Opt. Lett.*, vol. 35, no. 2, p. 259, 2010.

[17]   M. A. Soto, G. Bolognini, and F. Di Pasquale, "Analysis of optical pulse coding in spontaneous Brillouin-based distributed temperature sensors", *Opt. Express*, vol. 16, no. 23, p. 19 097, 2008.

[18]   M. A. Soto, G. Bolognini, and F. Di Pasquale, "Analysis of pulse modulation format in coded BOTDA sensors", *Opt. Express*, vol. 18, no. 14, p. 14 878, 2010.

[19]   H. Liang, W. Li, N. Linze, L. Chen, and X. Bao, "High-resolution DPP-BOTDA over 50 km LEAF using return-to-zero coded pulses", *Opt. Lett.*, vol. 35, no. 10, p. 1503, 2010.

[20]   M. A. Soto, G. Bolognini, and F. D. Pasquale, "Long-range simplex-coded BOTDA sensor over 120 km distance employing optical preamplification", *Opt. Lett.*, vol. 36, no. 2, p. 232, 2011.

[21] X.-H. Jia, Y.-J. Rao, Z.-N. Wang, W.-L. Zhang, C.-X. Yuan, X.-D. Yan, J. Li, H. Wu, Y.-Y. Zhu, and F. Peng, "Distributed Raman amplification using ultra-long fiber laser with a ring cavity: characteristics and sensing application", *Opt. Express*, vol. 21, no. 18, p. 21 208, 2013.

[22] M. Soto, X. Angulo-Vinuesa, S. Martin-Lopez, S.-H. Chin, J. Ania-Castanon, P. Corredera, E. Rochat, M. Gonzalez-Herraez, and L. Thevenaz, "Extending the real remoteness of long-range Brillouin optical time-domain fiber analyzers", *J. Lightwave Technol.*, vol. 32, no. 1, pp. 152–162, 2014.

[23] A. Fellay, L. Thévenaz, M. Facchini, M. Niklès, and P. Robert, "Distributed sensing using stimulated Brillouin scattering: towards ultimate resolution.", in *Proceedings of the 12th International Conference on Optical Fiber Sensors*, OSA, 1997, OWD3.

[24] K. Hotate and T. Hasegawa, "Measurement of Brillouin gain spectrum distribution along an optical fiber using a correlation-based technique – proposal, experiment and simulation", *IEICE Trans. Electron.*, vol. E83-C, no. 3, pp. 405–412, 2000.

[25] Y. Mizuno, W. Zou, Z. He, and K. Hotate, "Proposal of Brillouin optical correlation-domain reflectometry (BOCDR)", *Opt. Express*, vol. 16, no. 16, p. 12 148, 2008.

[26] M. A. Soto, S. Chin, and L. Thévenaz, "Double-pulse Brillouin distributed optical fiber sensors: analytical model and experimental validation", in *Proceedings of the 22nd International Conference on Optical Fiber Sensors*, vol. 8421, SPIE, 2012, p. 842 124.

[27] A. Brown, B. Colpitts, and K. Brown, "Distributed sensor based on dark-pulse Brillouin scattering", *IEEE Photon. Technol. Lett.*, vol. 17, no. 7, pp. 1501–1503, 2005.

[28] W. Li, X. Bao, Y. Li, and L. Chen, "Differential pulse-width pair BOTDA for high spatial resolution sensing", *Opt. Express*, vol. 16, no. 26, p. 21 616, 2008.

[29] S. Foaleng, M. Tur, J.-C. Beugnot, and L. Thevenaz, "High spatial and spectral resolution long-range sensing using Brillouin echoes", *J. Lightwave Technol.*, vol. 28, no. 20, pp. 2993–3003, 2010.

[30] K.-Y. Song, Z. He, and K. Hotate, "Distributed strain measurement with millimeter-order spatial resolution based on Brillouin optical correlation domain analysis and beat lock-in detection scheme", in *Proceedings of the 18th International Conference on Optical Fiber Sensors*, OSA, 2006, ThC2.

[31] O. Matsuoka, M. Kishi, and K. Hotate, "Brillouin optical correlation domain reflectometry with double frequency modulation and phase modulation", in *Proceedings of the 23rd International Conference on Optical Fiber Sensors*, vol. 9157, SPIE, 2014, 91576G.

[32]   M. A. Soto and L. Thévenaz, "Towards 1'000'000 resolved points in a distributed optical fibre sensor", in *Proceedings of the 23rd International Conference on Optical Fiber Sensors*, vol. 9157, SPIE, 2014, p. 9157C3.

[33]   A. Denisov, M. A. Soto, and L. Thévenaz, "Time gated phase-correlation distributed Brillouin fibre sensor", in *Proceedings of the 5th European Workshop on Optical Fibre Sensors*, vol. 8794, SPIE, 2013, p. 87943I.

[34]   D. Elooz, Y. Antman, N. Levanon, and A. Zadok, "High-resolution long-reach distributed Brillouin sensing based on combined time-domain and correlation-domain analysis", *Opt. Express*, vol. 22, no. 6, p. 6453, 2014.

[35]   M. Santagiustina, S. Chin, N. Primerov, L. Ursini, and L. Thévenaz, "All-optical signal processing using dynamic Brillouin gratings", *Sci. Rep.*, vol. 3, 2013.

[36]   S. Chin, N. Primerov, and L. Thevenaz, "Photonic delay line for broadband optical signals, based on dynamic grating reflectors in fibers", in *Proceedings of the 36th European Conference and Exhibition on Optical Communication (ECOC)*, IEEE, 2010, pp. 1–3.

[37]   Y. Antman, N. Primerov, J. Sancho, L. Thevenaz, and A. Zadok, "Localized and stationary dynamic gratings via stimulated Brillouin scattering with phase modulated pumps", *Opt. Express*, vol. 20, no. 7, p. 7807, 2012.

[38]   L. Liu, R. Kumar, K. Huybrechts, T. Spuesens, G. Roelkens, E.-J. Geluk, T. de Vries, P. Regreny, D. Van Thourhout, R. Baets, and G. Morthier, "An ultra-small, low-power, all-optical flip-flop memory on a silicon chip", *Nature Photon.*, vol. 4, no. 3, pp. 182–187, 2010.

[39]   M. T. Hill, H. J. S. Dorren, T. de Vries, X. J. M. Leijtens, J. H. den Besten, B. Smalbrugge, Y.-S. Oei, H. Binsma, G.-D. Khoe, and M. K. Smit, "A fast low-power optical memory based on coupled micro-ring lasers", *Nature*, vol. 432, no. 7014, pp. 206–209, 2004.

[40]   L. Brillouin, "Diffusion de la lumière et des rayons X par un corps transparent homogène. Influence de l'agitation thermique", *Ann. Phys.(Paris)*, vol. 17, no. 21, pp. 88–122, 1922.

[41]   L. Mandelstam, "Light scattering by inhomogeneous media («К вопросу о рассеянии света неоднородной средой»)", *Zh. Russ. Fiz-Khim*, vol. 58, p. 381, 1926.

[42]   R. Y. Chiao, C. H. Townes, and B. P. Stoicheff, "Stimulated Brillouin scattering and coherent generation of intense hypersonic waves", *Phys. Rev. Lett.*, vol. 12, no. 21, pp. 592–595, 1964.

[43]   R. W. Boyd, *Nonlinear Optics*. Academic Press, 2003, 597 pp.

[44]   G. P. Agrawal, *Nonlinear Fiber Optics*. Academic Press, 2007, 560 pp.

[45] R. W. Boyd, K. Rzaewski, and P. Narum, "Noise initiation of stimulated Brillouin scattering", *Phys. Rev. A*, vol. 42, no. 9, pp. 5514–5521, 1990.

[46] S. Foaleng Mafang, "Brillouin echoes for advanced distributed sensing in optical fibres", PhD thesis, EPFL, Lausanne, Switzerland, 2011.

[47] M. Nikles, L. Thevenaz, and P. Robert, "Brillouin gain spectrum characterization in single-mode optical fibers", *J. Lightwave Technol.*, vol. 15, no. 10, pp. 1842–1851, 1997.

[48] T. Horiguchi, T. Kurashima, and M. Tateda, "Tensile strain dependence of Brillouin frequency shift in silica optical fibers", *IEEE Photon. Technol. Lett.*, vol. 1, no. 5, pp. 107–108, 1989.

[49] K. Shimizu, T. Kurashima, T. Horiguchi, and Y. Koyamada, "New technique to shift lightwave frequency for distributed fiber optic sensing", in *Distributed and Multiplexed Fiber Optic Sensors II*, vol. 1797, SPIE, 1993, pp. 18–30.

[50] Y. Mizuno, Z. He, and K. Hotate, "Measurement range enlargement in Brillouin optical correlation-domain reflectometry based on double-modulation scheme", *Opt. Express*, vol. 18, no. 6, p. 5926, 2010.

[51] K. Hotate, K. Abe, and K. Y. Song, "Suppression of signal fluctuation in Brillouin optical correlation domain analysis system using polarization diversity scheme", *IEEE Photon. Technol. Lett.*, vol. 18, no. 24, pp. 2653–2655, 2006.

[52] Y. Antman, N. Levanon, and A. Zadok, "Low-noise delays from dynamic Brillouin gratings based on perfect Golomb coding of pump waves", *Opt. Lett.*, vol. 37, no. 24, p. 5259, 2012.

[53] Y. Antman, L. Yaron, T. Langer, M. Tur, N. Levanon, and A. Zadok, "Experimental demonstration of localized Brillouin gratings with low off-peak reflectivity established by perfect Golomb codes", *Opt. Lett.*, vol. 38, no. 22, p. 4701, 2013.

[54] J. Zhou, J. Chen, Y. Jaouen, L. Yi, H. Petit, and P. Gallion, "A new frequency model for pump-to-signal RIN transfer in Brillouin fiber amplifiers", *IEEE Photon. Technol. Lett.*, vol. 19, no. 13, pp. 978–980, 2007.

[55] A. David and M. Horowitz, "Low-frequency transmitted intensity noise induced by stimulated Brillouin scattering in optical fibers", *Opt. Express*, vol. 19, no. 12, p. 11 792, 2011.

[56] M. A. Soto and L. Thévenaz, "Modeling and evaluating the performance of Brillouin distributed optical fiber sensors", *Opt. Express*, vol. 21, no. 25, p. 31 347, 2013.

[57] G. Brambilla, "Optical fibre nanowires and microwires: a review", *J. Opt.*, vol. 12, no. 4, p. 043 001, 2010.

[58] C. Baker and M. Rochette, "High nonlinearity and single-mode transmission in tapered multimode-PMMA fibers", *IEEE Photon. J.*, vol. 4, no. 3, pp. 960–969, 2012.

[59] J.-C. Beugnot, S. Lebrun, G. Pauliat, H. Maillotte, V. Laude, and T. Sylvestre, "Brillouin light scattering from surface acoustic waves in a subwavelength-diameter optical fibre", *Nat. Commun.*, vol. 5, 2014.

[60] Y. London, Y. Antman, R. Cohen, N. Kimelfeld, N. Levanon, and A. Zadok, "High-resolution long-range distributed Brillouin analysis using dual-layer phase and amplitude coding", *Opt. Express*, vol. 22, no. 22, pp. 27 144–27 158, 2014.

[61] R. Cohen, Y. London, Y. Antman, and A. Zadok, "Brillouin optical correlation domain analysis with 4 millimeter resolution based on amplified spontaneous emission", *Opt. Express*, vol. 22, no. 10, pp. 12 070–12 078, 2014.

[62] L. G. Cohen and J. W. Fleming, "Effect of temperature on transmission in light-guides", *Bell Syst. Tech. J.*, vol. 58, no. 4, pp. 945–951, 1979.

[63] K. Y. Song, "Operation of brillouin dynamic grating in single-mode optical fibers", *Opt. Lett.*, vol. 36, no. 23, p. 4686, 2011.

[64] P. T. Rakich, C. Reinke, R. Camacho, P. Davids, and Z. Wang, "Giant enhancement of stimulated Brillouin scattering in the subwavelength limit", *Phys. Rev. X*, vol. 2, no. 1, p. 011 008, 2012.

[65] H. Shin, W. Qiu, R. Jarecki, J. A. Cox, R. H. O. Iii, A. Starbuck, Z. Wang, and P. T. Rakich, "Tailorable stimulated Brillouin scattering in nanoscale silicon waveguides", *Nat. Commun.*, vol. 4, 2013.

[66] R. Van Laer, B. Kuyken, D. Van Thourhout, and R. Baets, "Interaction between light and highly confined hypersound in a silicon photonic nanowire", *Nature Photon.*, vol. 9, no. 3, pp. 199–203, 2015.

[67] M. Merklein, I. V. Kabakova, T. F. S. Büttner, D.-Y. Choi, B. Luther-Davies, S. J. Madden, and B. J. Eggleton, "Enhancing and inhibiting stimulated Brillouin scattering in photonic integrated circuits", *Nat. Commun.*, vol. 6, 2015.

[68] B. J. Eggleton, C. G. Poulton, and R. Pant, "Inducing and harnessing stimulated Brillouin scattering in photonic integrated circuits", *Adv. Opt. Photonics*, vol. 5, no. 4, p. 536, 2013.

[69] L. Thévenaz, "Silicon nanophotonics: good vibrations for light", *Nature Photon.*, vol. advance online publication, 2015.

[70] R. Pant, E. Li, C. G. Poulton, D.-Y. Choi, S. Madden, B. Luther-Davies, and B. J. Eggleton, "Observation of Brillouin dynamic grating in a photonic chip", *Opt. Lett.*, vol. 38, no. 3, p. 305, 2013.

Publications

Journal papers

1. A. Denisov, M. A. Soto and L. Thévenaz, "Going beyond 1 000 000 resolved points in a Brillouin distributed fibre sensor: theoretical analysis and experimental demonstration", *submitted to Light: Science & Applications*, 2015.,

2. F. Alishahi, A. Vedadi, T. M. P. Hoang, M. A. Soto and A. Denisov et al., "Power evolution along phase-sensitive parametric amplifiers: an experimental survey", *Optics Letters*, vol. 39, num. 21, p. 6114, 2014.

3. A. Zadok, Y. Antman, N. Primerov, A. Denisov and J. Sancho et al., "Random-access distributed fiber sensing", *Laser & Photonics Reviews*, vol. 6, num. 5, pp. L1–L5, 2012.

Conference proceedings

1. L. Thévenaz, A. Denisov and M. A. Soto, "Brillouin Distributed Fiber Sensing at Ultra-High Spatial Resolution" (in press). *2015 IEEE Photonics Conference (IPC)*, Reston, USA. 4–8 October 2015.

2. F. Alishahi, A. Vedadi, M. A. Shoaie, M. A. Soto and A. Denisov et al., "Effect of Dispersion Fluctuations on Longitudinal Gain Evolution in Phase-Sensitive Parametric Amplifiers", in *Proceedings of CLEO: Science and Innovations*, OSA, 2014, STu3N-4.

3. A. Denisov, M. A. Soto and L. Thévenaz, "1'000'000 resolved points along a Brillouin distributed fibre sensor", in *Proceedings of the 23rd International Conference on Optical Fiber Sensors*, SPIE, 2014, 9157D2.

4. F. Alishahi, A. Vedadi, M. A. Soto, A. Denisov and K. Mehrany et al., "Distributed Measurement of Signal Power Evolution in a Phase Sensitive Parametric Amplifier", in *Proceedings of Optical Fiber Communication Conference*, OSA, 2014, Th1H-4.

5. F. Alishahi, A. Vedadi, A. Denisov, M. A. Soto and K. Mehrany et al., "Highly Sensitive Dispersion Map Extraction from Highly Nonlinear Fibers Using BOTDA Probing of Parametric Amplification", in *Proceedings of European Conference on Lasers and Electro-Optics (CLEO-Europe)*, IEEE, 2013, p. 1.

6. A. Denisov, M. A. Soto and L. Thévenaz, "Time gated phase-correlation distributed Brillouin fibre sensor", in *Proceedings of the 5th European Workshop on Optical Fibre Sensors*, SPIE, 2013, pp. 87943I–87943I.

7. F. Alishahi, A. Vedadi, A. Denisov, M. A. Soto and K. Mehrany et al., "Mapping Dispersion Fluctuations along Optical Fibers Using Brillouin Probing and a Fast Analytic Calculation", in: *Proceedings of CLEO Conference*, San Jose, USA, 2013.

8. L. Thévenaz, N. Primerov, S. Chin, Y. Antman and A. Denisov et al., "All-optical storage and processing in optical fibers", in: *Proceedings 3rd International Conference on Photonics (ICP 2012)*, IEEE, 2012.

9. A. Denisov and L. Thévenaz. "Frequency-Agile Brillouin Optical Time-Domain Analysis Fibre Sensor", in: *Proceedings of IONS-11*, OSA, 2012.

10. X. Angulo-Vinuesa, S. Martin-Lopez, C. Caucheteur, D. Kinet and M. Wuilpart et al., "Kerr effect in structured superluminal media", in: *Proceedings of Photonics West - Advances in Slow and Fast Light V*, SPIE, 2012, pp. 827310–827310.

Andrey Denisov

andrey.denisov.nsu@gmail.com **linkedin.com/in/andreydenisov**

EDUCATION

2011 – 2015	**PhD in Photonics**, *École Polytechnique Fédérale de Lausanne, Switzerland*
2008 – 2010	**Master of Physics**, *Novosibirsk State University, Russia*
2004 – 2008	**Bachelor of Physics**, *Novosibirsk State University, Russia*
2013 – present	**Continuing education,** online courses on statistics, machine learning, data science, and other subjects.

EXPERIENCE

2011.06 – 2015.09 **Doctoral researcher**, *École Polytechnique Fédérale de Lausanne, Switzerland*
- Successfully completed four research projects in Brillouin fibre sensing: two long (1+ years) and two short (3 months).
- Over the course of 2 years improved the performance of a new sensing technique by 100 times, setting an absolute record in the field.
- Developed software for equipment control and data analysis in LabView and Matlab, to be used by myself and my colleagues.
- Created and experimentally verified two major mathematical models.
- Organised a test of an optoelectronic prototype for the manufacturer. The test report was used to create the next generation of the device.
- Authored and coauthored 12 publications for high-impact journals and conferences. Presented results at the biggest conference in the field.

2006.09 – 2011.04 **Junior researcher (20%–100%)**
Institute of Automation and Electrometry, Novosibirsk, Russia
- Part of the team of three in two scientific projects on fibre laser, with central role in modelling of physical processes.
- Tested and assembled the optical part of a pulsed UV laser prototype providing feedback for the CAD designer and the collaborator working on the fibre part.
- For 3 years worked in the organising committee of a student conference.

2009.09 – 2011.05 **Founder, coordinator, lecturer**, *Science for Kids, Novosibirsk, Russia*
- One of the volunteer project founders; wrote the budget section for a grant proposal; worked in a team of 5 to start the project and attract new members.
- Gave 15 presentations on physics and optics – lectures and demonstrations, adapting for the audience: school students 9 to16 years old.

2009.02 – 2009.10 **English-Russian translator (remote work)**, *RuFilms, Moscow, Russia*
- Translated subtitles and scripts for 20 movies and documentaries

IT SKILLS

Data analysis	• Matlab; basic knowledge of R and SQL
Programming	• Python, C++, LabView
Text and graphics	• Word and LaTeX for structured, well-designed documents
	• Adobe Illustrator for professional looking figures

LANGUAGES

English	Full working proficiency (C2)	Russian	Mother tongue
French	Intermediate (B1), in progress	German	Basic